NTNU
Norwegian University of
Science and Technology

Structure of Clean and Oxidized PdCu (100) Surfaces at the Atomic Scale

John Fjermestad Aase

Master of Science in Physics and Mathematics
Submission date: February 2012
Supervisor: Anne Borg, IFY

Norwegian University of Science and Technology
Department of Physics

Structure of Clean and Oxidized PdCu(100) Surfaces at the Atomic Scale

Master thesis, NTNU.

John Fjermestad Aase

20.02.2012

The work was carried out under supervision by professor Anne Borg.

Abstract

In this thesis, clean and oxidized $Pd_{57}Cu_{43}(100)$ single crystal surfaces were studied by LEED, STM and XPS in UHV conditions. The clean sample annealed to 300^oC has been found to either consist of ordered domains of Pd or Cu atoms forming a $c(2 \times 2)$ structure, or by a more disordered alloy $c(2 \times 2)$ structure of p4g symmetry. Small areas of (1×1) structure as well as screw dislocations and island- like formations are present on this surface. Annealing the clean sample to 600^oC causes Cu segregation to the surface as well as a shift towards higher binding energy of Pd $3d_{\frac{5}{2}}$ core levels, and an almost defect- free surface with $p(2 \times 2)$ structure is seen. Oxidation at 300^oC of the surface annealed to 300^oC shows that a $c(2 \times 2)$ covers the whole surface for all oxygen dosages at 68L or above, and XPS spectra do not vary with oxygen dosage, hence the $c(2 \times 2)$ is inert in this case. For dosages of 1350L or above, oxide islands and a large number of defects could appear, depending on the preparation history of the sample. Oxidation at 300^oC and 600^oC of the Cu rich surface annealed to 600^oC reveals up to seven structures, which are $p(2 \times 2)$, $c(2 \times 2)$, (4×4)-like, hexagonal, maze- like, $(2\sqrt{2} \times \sqrt{2})R45^o$ missing row type and one more structure that could not be characterized. There is evidence that copper oxide phases are formed for the Cu rich surfaces annealed to 600^oC, but no bulk oxide was formed in any experiments. A detailed understanding of clean and oxidized $Pd_{57}Cu_{43}(100)$ has been obtained at the atomic scale.

Samandrag

I denne masteroppgåva har reine og oksiderte overflater av ein $Pd_{57}Cu_{43}(100)$ einkrystall vorte studert ved hjelp av LEED, STM og XPS i ultrahøgvakuum. Den reine overflata oppvarma til 300^oC består anten av ordna domener av Pd- eller Cu- atom som dannar ein $c(2 \times 2)$- struktur, eller av ein meir uordna $c(2 \times 2)$- legeringsstruktur med p4g- symmetri. Små område med (1×1)- struktur i tillegg til skrudislokasjonar og øyliknande formar kan sjåast på denne overflata. Oppvarming av rein overflate til 600^oC fører til at Cu segregerer til overflata i tillegg til at Pd $3d_{\frac{5}{2}}$ kjernenivåa flyttar seg mot høgare bindingsenergi, og overflata er nesten defektfri med $p(2 \times 2)$- struktur. Oksidering ved 300^oC av overflata som er oppvarma til 300^oC syner at ein $c(2 \times 2)$- struktur dekkjer overflata for alle oksygendosar på 68L eller meir, og XPS- spekter varierer ikkje med oksygendose, noko som tyder at $c(2 \times 2)$- strukturen er ureaktiv i dette tilfellet. For dosar over 1350L eller meir ser ein av og til øyar og mange defektar, avhengig av prepareringshistorikken til prøva. Oksidering ved 300^oC og 600^oC av den koparrike overflata varma til 600^oC fører til opptil sju ulike strukturar. Desse er $p(2 \times 2)$, $c(2 \times 2)$, (4×4)- liknande, heksagonal, labyrint- liknande, $(2\sqrt{2} \times \sqrt{2})R45^o$ manglande rad- type og ein til som ikkje vart stadfesta. Det vart funne prov på at koparoksid vert danna på den koparrike overflata varma til 600^oC, men bulkoksid vart ikkej sett i nokre av eksperimenta. Ei detaljert forståing av rein og oksidert $Pd_{57}Cu_{43}(100)$ er oppnådd på atomært nivå.

Preface

This thesis concludes my Masters degree in applied physics. During my time as a student of physics and mathematics with specialization in applied phyisics, I have taken courses in almost all major fields of physics, as well as many other courses. I have learned a lot, not only about physics, but also about myself. The Masters programme has been very challenging, but also fun and interesting. At this point, though, I am glad it is finally over.

I would like to thank my supervisor, Professor Anne Borg, for letting me write my project and Masters thesis about surfaces of materials while performing experimental work. When I started my project work, I was pretty low on motivation and just wanted to finish my masters degree as soon as possible, but I soon realized that studying materials with STM is both interesting and fun. I am therefore very glad I was given the opportunity to do so. A great thanks also to Dr. Lars Erik Walle for helping me in the lab and with the XPS data, and not least for fixing the STM that time I broke it! Also thanks to PhD student Mari Helene Farstad for fitting the XPS spectra for me, and to PhD student Vasco Fernandes for his help in the lab and with Gwyddion.

I would also like to thank all my friends and relatives who have encouraged me to finish my degree. Last, but not least, a great thanks to Anna who has been there for me all the time. Without her my life as a student would have been intolerable, and I would probably never have gone to Singapore for a whole year as an exchange student unless she joined me.

Contents

1. Introduction

1.1 Model catalysts

Catalysts are often used in industry and everyday life to control various chemical reactions. They have the ability to enhance reactions by participating in them without being consumed, and offer huge advantages in controlling both reaction speed and reaction products. In heterogeneous catalysis, the catalyst and reactants are in different physical states, e.g. with catalyst in solid state and reactants in gas phase. Several metals are known to hold catalytic properties, but since most metals are oxidized in ambient conditions, the effect of oxidation on their catalytic behaviour is important to understand [1]. During the past decade, several studies of oxidation of late transition metals such as Ag, Pd, Rh and Pt have revealed the formation of well- ordered surface oxides [2]. Applying powerful experimental techniques as well as theoretical modeling, one has found that surface oxides represent oxide layers in a phase that is in between chemisorbed atomic oxygen and bulk oxide, displaying complex structures and properties different from those of the bulk oxide [2, 3].

Although catalysts are fabricated as macroscopic modules, catalysis itself is a microscopic phenomenon. The observed macroscopic properties can thus be explained at the atomic scale. In real world applications, catalysts usually operate under high temperatures and pressures, and the catalytically active surface is continually changing due to adsorption, reaction, desorption, segregation and diffusion mechanisms. Hence it is very difficult to understand what is going on at the atomic scale. For this reason, simplified model systems involving single crystals of catalytic materials are often studied under ultra high vacuum conditions. Despite the simpleness of model systems, they have resulted in a much better understanding of the basic processes in catalysis. This is perhaps best illustrated by the Nobel prize in chemistry in 2007 being awarded to Gerhard Ertl for his studies of chemical processes on solid surfaces [4]. At present, there are suggestions that it may not be the metals themselves that are the catalytically active phase in oxidation reactions, but rather their oxidized forms [2, 3, 5, 6].

1.2 Membranes for H_2 production

The demand for clean energy has increased heavily during the last couple of decades due to the environmental issues related to burning of fossil fuels. However, fossil fuels will remain an important source to energy in the foreseeable future. It is therefore of high interest to use fossil fuels as energy sources without having to worry about pollution and environmental effects. This is possible if fuels are gasified instead of burned [7, 8]. By only partial oxidation of energy sources such as coal, oil, natural gas and biomass, they can be processed to produce synthetic gas (syngas), consisting mainly of carbon monoxide (CO) and molecular hydrogen (H_2) as well as other products like H_2S, CO_2

and Cl compounds, depending on the source of syngas. Hydrogen can then be separated from the syngas by catalytic selective membranes. A simple illustration of gasification is given in Figure (1.1). H_2 is adsorbed on the catalytically active membrane surface where H atoms are formed, which can diffuse through the membrane and desorb as H_2 on the other side [9, 10]. Depleted syngas can be further processed by the water- gas shift reaction, in which steam reacts with CO in the presence of a catalyst to form CO_2 and more H_2 that can be separated.

Gasification has the huge advantage that one of its products is high- purity H_2 gas that can be stored and burnt elsewhere. It also offers the possibility of processing or capturing CO_2 and other by-products instead of letting them into the atmosphere, although such processing costs energy. Hence fossil fuels, which are potential environmental hazards, can be used to produce clean fuel, while the fossil fuels and their by- products can be processed away from populated areas. Hydrogen finds potential future applications in electricity production as well as fuels for fuel cells in industries, airplanes, automobiles, homes and several other parts of everyday life [11]. When hydrogen is burned, the only reaction product is water vapour, i.e. no pollution is emitted. It is expected that hydrogen will gradually gain interest as the world runs out of traditional fuels and oil becomes more expensive [11]. An important role in production of hydrogen is obviously played by the catalysts that enhance the chemical reactions and the selective membranes. Gaining more knowledge about their materials and how they behave in the mentioned processes would allow us to further optimize hydrogen production and promote the use of clean energy.

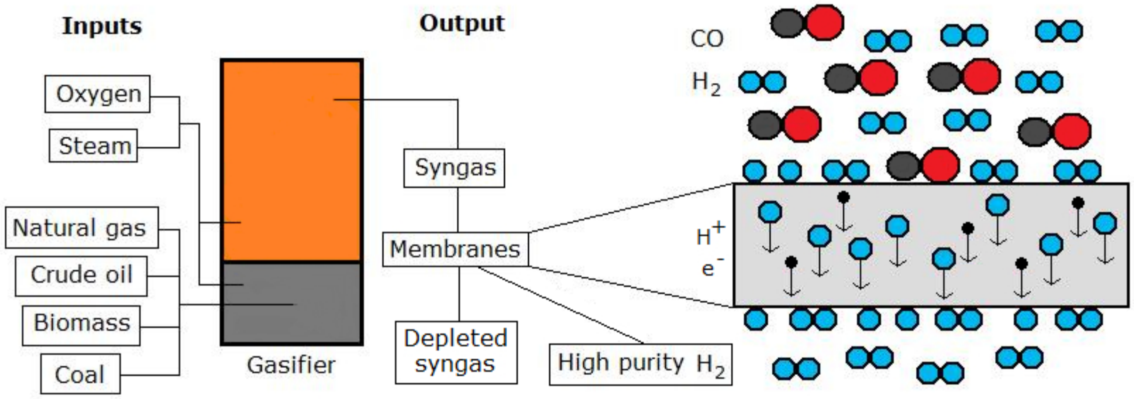

Figure 1.1: A gasifier and a membrane

1.3 Palladium and palladium alloys

Palladium may be used as a catalyst for combustion of methane [12] and oxidation of hydrocarbons in automotive exhausts [13], and is also the most promising material for hydrogen permeable membranes because of its catalytic surface, high hydrogen permeability, infinite hydrogen selectivity, temperature stability and corrosion resistance [14]. Unfortunately, pure palladium suffers from several disadvantages. Upon hydrogen separation, hydride phase transitions can occur which cause irreversible embrittlement of palladium membranes, thus giving them poor mechanical strength [15].

Hydrogen permeation can be severely reduced when a membrane is contaminated by oxide, sulfur and other syngas compounds [9, 10]. Especially problematic is H_2S, which could lead to the formation of bulk Pd_4S [16] with a hydrogen permeability 20 times less than that of pure Pd [17]. Palladium is also a material of high cost [10].

These problems can be avoided while maintaining the good properties of Pd by alloying it with other materials such as Au, Ag, Cu and Ru, forming either binary [18] or ternary alloys [19]. PdAu alloys have shown some resistance to H_2S, no structural damage due to embrittlement and high performance especially at high temperatures [16, 20] with a maximum hydrogen permeability at roughly 12% Au [21]. PdAg alloys show similar properties to those of PdAu, with a maximum hydrogen permeability at roughly 20% Ag [21]. PdRu has very good mechanical strength even at high temperatures, and high hydrogen permeability at <10% Ru [22]. Most interesting is probably PdCu alloys, which have shown great resistance towards H_2S poisoning, and hydrogen permeabilities comparable to that of pure Pd even up to as much as 50% Cu, with maxiumum permeability at 40% Cu [9, 23, 24]. It has been found that a pure Pd membrane could be covered by a sulfuric overlayer several μm thick, whereas a layer of only a few nm is formed on a $Pd_{47}Cu_{53}$ membrane after exposure to 1000ppm H_2S [9]. This, and the fact that Cu is a more low-cost material than Au, Ag and Ru, is the reason why PdCu alloys seem the most promising materials for membranes.

1.4 Purpose of this thesis

The purpose of this thesis is to gain a better understanding of the physical phenomena that occur on the catalytically active surfaces of PdCu membranes. Plenty of experiments are found in the literature in which such membranes were studied at large scale, but none have been reported which describe membrane properties at the atomic scale. Particularly, one is interested in the interaction of oxygen with PdCu surfaces at varying temperatures and pressures. It has been reported that thermal treatment in air has improved hydrogen permeability of Pd and PdCu [25] as well as PdAg membranes [26, 27, 28, 29, 30], most likely due to surface roughening and oxidation of contaminants. However, one still does not fully understand the true nature of clean PdCu and its oxidation mechanisms.

In this thesis, a $Pd_{57}Cu_{43}(100)$ single crystal has been studied in UHV as a model system of a PdCu membrane. The clean surface has been studied after annealing to different temperatures, and the oxidized surface has been studied after different annealings and oxidations at different temperatures and O_2 pressures. Results from Low Energy Electron Diffraction (LEED), synchrotron- based X- ray Photoelectron Spectroscopy (XPS) and Scanning Tunneling Microscopy (STM) have been combined in order to gain a much better understanding of this surface. Important features such as surface structures, defects, growth mechanisms, segregation and chemical composition are presented and discussed in detail. Atomic resolution with STM has been achieved for all sample preparations.

2. Theory

This chapter explains the basic theory behind the physical phenomena observed in the work with this thesis. The surface region of a solid sample studied in a UHV system is an interface between the solid bulk on one side and vacuum or gas on the other side. A surface therefore interacts in several ways with the substrate and any gas particles present in the vacuum chamber. In the first section, basic surface features such as structures and defects are described along with kinetic processes of adsorbates. Then principles behind film growth and overlayer atomic structures are given, before a short explanation is given of atomic structure and segregation in bimetallic alloys. Finally, a mechanism of oxidation of metal surfaces is presented.

2.1 Surfaces

Surfaces of solids appear flat and smooth on a macroscopic scale, but at the atomic level, they appear as complex and anisotropic landscapes that deviate heavily from the ideal defect- free surface [31, 32]. Figure (2.1) shows what a typical surface might look like. Always present are step edges one or more atomic layers in height of different shapes and directions, which separate flat terraces. Step edges are considered defects, as they cause otherwise perfectly flat surfaces such as e.g. the (100) plane of an fcc crystal to deviate from the ideal case. Point defects can be present both in terraces and on step edges. Most common are vacancies, which are lattice points with missing atoms. Defects in the atomic structure of the surface can also be present, such as screw and edge dislocations. An edge dislocation occurs if e.g. n rows of atoms merge to form $n-1$ rows. Where a screw dislocation is present, a step edge originates on a terrace in such a way that it is possible to draw an imaginary line from one step height to another without crossing a step edge. Impurities will always be a part of any sample, and could be present on the surface.

In surface science, one often wants to deposit or adsorb a material onto a sample. Atoms or molecules can be adsorbed physically (physisorption) or chemically (chemisorption) on a surface. Physisorbed atoms are bound to the surface atoms by the van der Waals interaction, which is a process that does not require an activation energy, whereas chemisorbed atoms form covalent, ionic or strong polar bonds to surface atoms. Adsorbed atoms are called adatoms, and they are randomly distributed on a sample surface upon exposure. Figure (2.2) shows common kinetic processes that adatoms can undergo once adsorbed on a surface. It is found that the molecular or atomic impingement rate I (molecules per cm^2 per second) onto a surface is [32]:

$$I = \frac{p}{\sqrt{2\pi mkT}} \tag{2.1}$$

where p is the pressure, m the mass of impinging particles, k the Boltzmann constant and T the temperature. The opposite of adsorption is desorption, in which an adatom is re-evaporated from

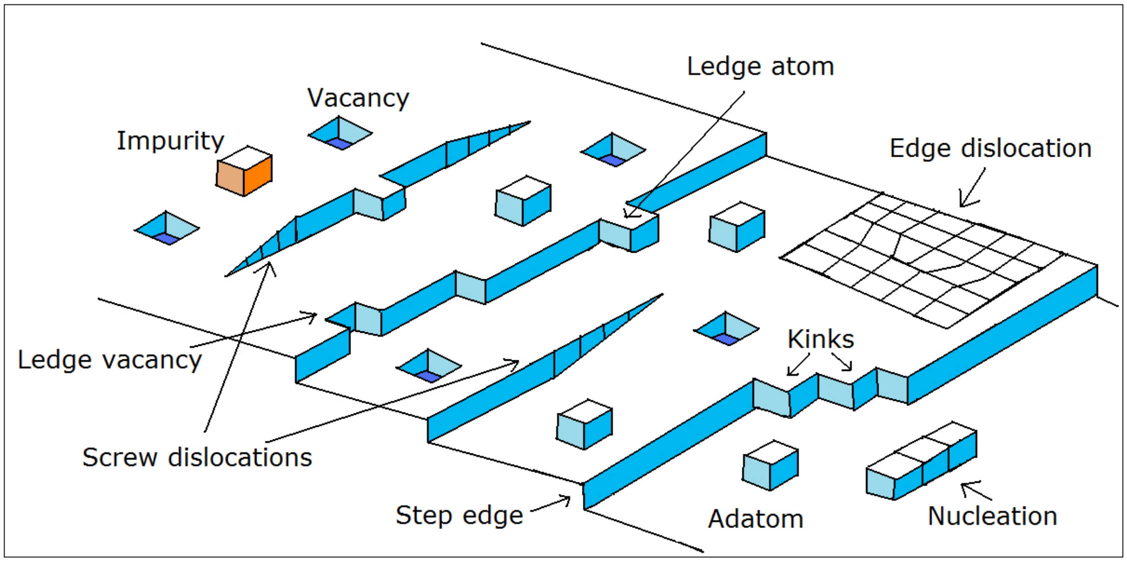

Figure 2.1: An illustration of defects that can be present on a surface. Based on figure from [33].

the surface. This requires an activation energy per adatom, and the desorption frequency ν_{des} is given by [32]:

$$\nu_{des} = \nu_0 \exp\left[\frac{-\Delta G_{des}}{kT}\right] \tag{2.2}$$

where ΔG_{des} is the activation free energy of desorption and ν_0 is an attempt frequency on the order of the atomic vibrational frequency of the surface atoms, usually $\propto 10^{13}$ s^{-1}. The mean lifetime of an adatom on the surface, τ_a is then [32]:

$$\tau_a = \frac{1}{\nu_{des}} \tag{2.3}$$

By defining n_a as the number of adatoms per cm^2, the desorption rate $E = \frac{n_a}{\tau_a}$ [32]. In equilibrium, E is equal to I, which gives the following value of n_a [32]:

$$n_a = \frac{\nu_0 p}{\sqrt{2\pi mkT}} \exp\left[\frac{-\Delta G_{des}}{kT}\right] \tag{2.4}$$

Hence the amount of adsorbed atoms or molecules depends on their mass and their interaction with the sample surface as well as on the pressure and temperature at which adsorption occurs. Note that the value of ΔG_{des} could change as the surface is covered by an increasing amount of adatoms, since adatoms may interact differently with other adatoms than with the substrate. If an adatom does not desorb, it may diffuse across the surface and eventually form chemical bonds to surface atoms by nucleation. The diffusivity is a measure of the mobility of adsorbed species, which determines whether or not they are mobile enough to diffuse to any preferred nucleation sites such as vacancies, clusters, islands or defects. Adatoms move on terraces by a random walk process, with mean distances $\overline{R}$ given by [32]:

$$\overline{R^2} = 2D_a t \tag{2.5}$$

where t is the time it takes to travel a distance $\overline{R}$. The intrinsic diffusion coefficient of an adatom, D_a, is given by [32]:

$$D_a = \frac{l^2}{4\tau} \tag{2.6}$$

where l is the adatom jump distance on the order of the surface lattice parameter and τ is the mean time between jumps. Diffusion occurs if an adatom overcomes the diffusion activation barrier, ΔE_d. If the barrier is large compared to kT, the diffusion coefficient is [32]:

$$D_a = \frac{l^2 \nu_x}{2} \exp\left[\frac{-\Delta E_d}{kt}\right] \tag{2.7}$$

whereas it is proportional to $\sqrt{T}$ if the barrier is small compared to kT, in which case adatoms move freely as a 2D gas on the surface. An expression can be found for the overall surface diffusivity [33]:

$$D = D_0 \exp\left[\frac{-\Delta E_d}{kT}\right] \tag{2.8}$$

where D_0 is the maximum diffusion coefficient at $T = \infty$. These equations show that adatoms are more mobile at higher temperatures. Higher mobility means that they have increased probability of nucleating at preferred sites. One consequence of this is that in the case of island growth, the amount of clusters or islands will decrease with higher temperature because there is an increasing probability that adatoms attach to already existing islands than form new islands [34]. If the mobility is very high, adatoms may nucleate at step edges so that step edges grow at the expense of islands because adatoms diffuse to step edges instead of nucleate islands on terraces.

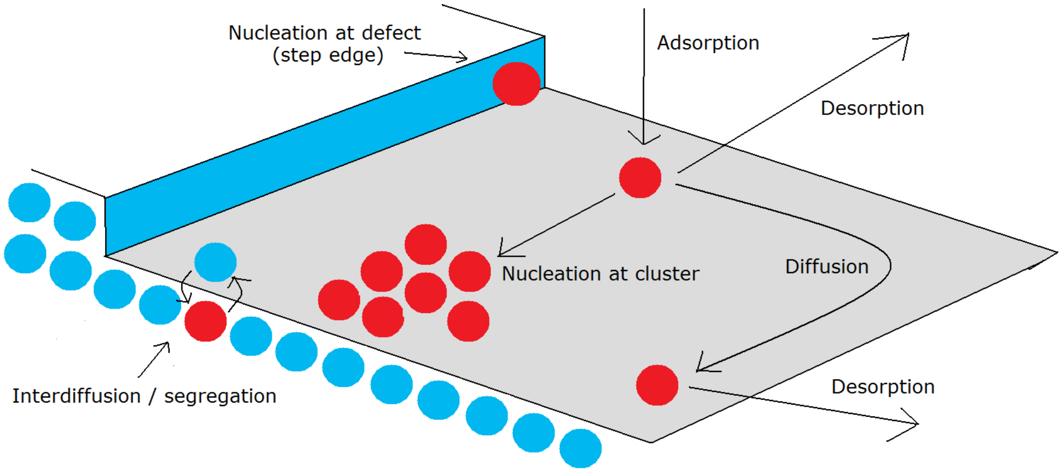

Figure 2.2: Kinetic processes on surfaces. Based on figure from [35].

2.2 Thin film growth modes

Growth of thin films with the same crystal structure and orientation as the substrate is called epitaxy, which means growth of a crystal on another crystal [36]. If the deposited material is the same as the substrate material, the process is referred to as homogeneous epitaxy. Heterogeneous epitaxy means growth of a material on another material. The deposited material does however not necessarily grow into the same structure as the substrate, in which case the growth would be non-epitaxial. Thin film growth is usually divided into three categories [37]:

- Frank- van der Merwe (FM): Layer-by-layer growth
- Volmer- Weber (VW): Island growth
- Stranski- Krastanov (SK): Layer plus island growth

These are illustrated in Figure (2.3). In FM growth the next layer will only start growing once the previous layer is completed. VW growth results in three- dimensional islands, and the surface is not completely covered by the deposited material unless the coverage is high enough for islands to coalesce. SK growth starts out in a layer-by-layer mode, but switches to island growth after one or more layers are completed. To explain this, one needs to consider the thermodynamics and surface free energies, γ between the different interfaces present during growth. It is then practical to introduce variables for the surface free energy of each interface. These are surface free energy for the substrate-vacuum interface (γ_S), the film-vacuum interface (γ_F) and the substrate-film interface (γ_{SF}). If deposition is performed in vacuum, growth modes depend on $\Delta\gamma$, which is [37]:

$$\Delta\gamma = \gamma_F + \gamma_{SF} - \gamma_S + CkTln\left(\frac{p'}{p}\right) \tag{2.9}$$

where C is a material- dependent constant, p' the equilibrium vapour pressure of the depositing material and p is the pressure of the gas phase. When $\Delta\gamma<0$, the interaction between film and substrate atoms is greater than the interaction between film atoms. Layer $(n+1)$ will then start growing once layer n is finished, and a Frank- van der Merwe growth is observed. If $\Delta\gamma>0$, the interaction between film atoms is greater than that between substrate and film. Film atoms then prefer to bond with other film atoms rather than with substrate atoms, and diffusion will cause islands to form as in Volmer- Weber growth. In Stranski- Krastanov growth the sign of $\Delta\gamma$ changes at a certain point. The reason for this is that there is a difference in lattice parameters of the growing film and the substrate so that an elastic deformation energy is established. Transition from layer to island growth occurs when the film becomes thick enough to sufficiently isolate the film surface from the deformation forces present at the the substrate-film interface [35]. In summary, it is clear that growth mode depends on adsorbate-adsorbate and adsorbate-substrate interactions, lattice matching, strain, pressure and temperature [37].

2.3 Reconstruction and relaxation

Atoms at the surface of a solid have neighbouring atoms only on side, meaning that the periodical structure of the bulk is abruptly terminated. This affects surface atoms in the topmost layers because dangling bonds and local density of states is assosiated with a certain surface free energy [31]. Due to the tendency of the surface to minimize its excess surface energy, strain effects arise which can trigger relaxation or reconstruction. Relaxation is when atoms of the topmost layers are displaced in the direction orthogonal to the surface. Since electron density is reduced for surface

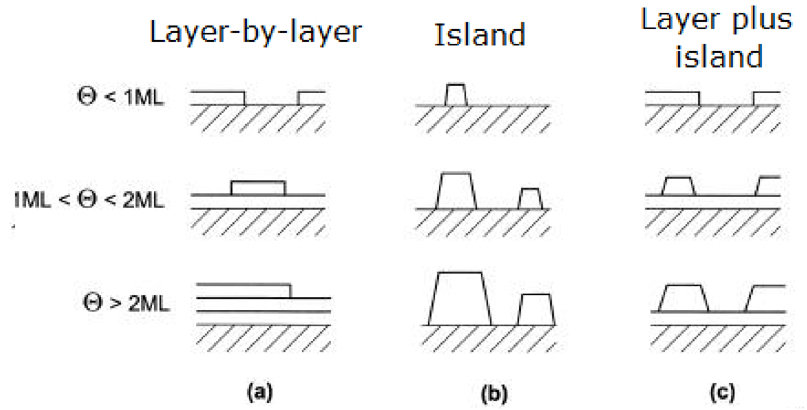

Figure 2.3: The three thin film growth modes for different monolayer coverages (Θ) [36].

atoms because of a lower coordination number and missing neighbours, an inwards displacement of such atoms is often favoured, as that increases the local density of states. In some materials such as transition metals (e.g. Pd), atoms may also relax outwards, depending on the relative strengths of the outward pressure of delocalized sp- electrons and the inward pressure of localized d electrons [38]. Surfaces of most materials undergo relaxation, but many also experience lateral displacements which could change the atomic structure in a process called reconstruction. Figure (2.4) illustrates the two processes.

Surface stress can arise from thermodynamic and electric properties in the surface region. A relation between stress and surface energy can be found via the contribution of the surface to an infinetesimal change in the Helmholtz free energy F_s [31]:

$$dF_s = \gamma dA + Ad\gamma \tag{2.10}$$

where γ is the surface free energy and A is the surface area. The first term represents a change in surface area, e.g. by a change in density of atoms, whereas the second term represents a change in interatomic distances at a fixed number of atoms. Obviously, both of these terms can be nonzero during relaxation or reconstruction in a solid surface. Using equation 2.10 it is possible to derive the Shuttleworth equation [31]:

$$\sigma_{ij} = \gamma\delta_{ij} + \frac{\partial\gamma}{\partial\epsilon_{ij}} \tag{2.11}$$

where σ_{ij} is the surface stress tensor, δ_{ij} is the Kronecker delta function and ϵ_{ij} is the strain tensor. The second term is crucial to reconstructions, as it describes how the surface free energy varies with the strain. Needs et al. have used this to develope a model describing the stability of a simple cubic (100) system towards 1- dimensional reconstruction [39]. The parameter P, given by [39]:

$$P = \frac{\pi a^2(g-\gamma)}{2\sqrt{2\mu a^2 W}} \tag{2.12}$$

where a is the lattice parameter, g the total surface stress, μ the interatomic force constant between surface atoms and W the strength of the surface-substrate interaction. If P>1 the surface reconstructs by adding atoms to the top layer, if P<-1 it reconstructs by removing atoms, and if $|P| < 1$

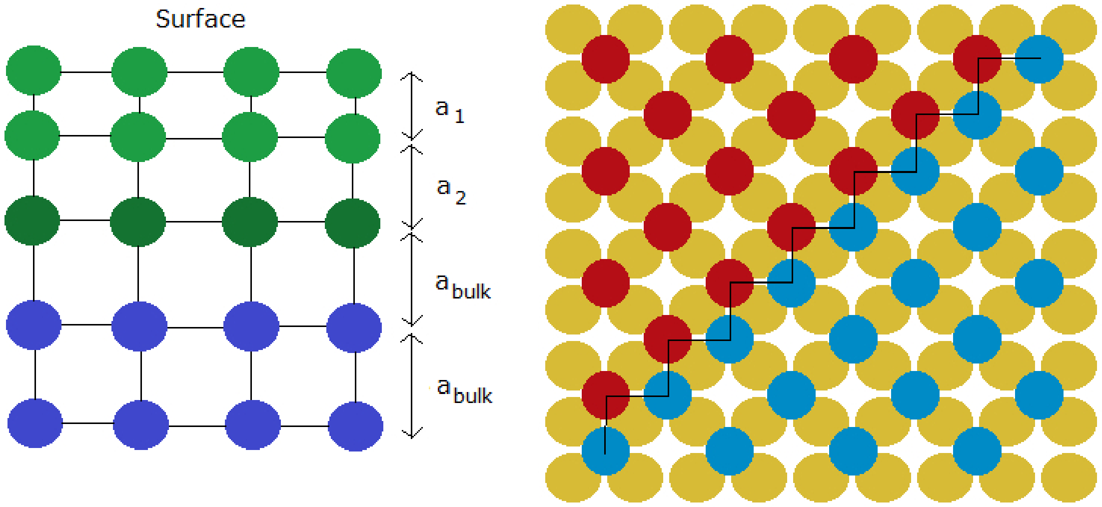

Figure 2.4: Left: A surface in which the first two atomic layers are relaxed inwards. Based on figure from [35]. Right: A reconstructed surface with atoms in 4- fold hollow sites forming a $(\sqrt{2} \times \sqrt{2})$ R45^o structure on top of a cubic (1×1) crystal. Atoms of red and blue colour are out of phase with respect to eachother, thus resulting in a domain boundary line.

the surface is stable and there will be no reconstruction. Another, more simple model was developed by Cammarata, in which strain energy is compared to energy of formation of a dislocation [40, 41]. The surface reconstructs if [40, 41]:

$$0.1 < \frac{g - \gamma}{Gb} \tag{2.13}$$

where G is the shear modulus and b is the magnitude of the Burger vector of the dislocation. Reconstructions are usually written in the Wood notation [31]:

$$S(hkl)\kappa \left(\frac{|\vec{b_1}|}{|\vec{a_1}|} \times \frac{|\vec{b_2}|}{|\vec{a_2}|} \right) R\phi^o \tag{2.14}$$

κ can be p (primitive) or c (centered), vectors $\vec{b_1}$ and $\vec{b_2}$ are the primitive lattice vectors of the reconstructed layer, $\vec{b_1}$ and $\vec{b_1}$ those of the bulk, and $R\phi^o$ means rotation of the overlayer by ϕ degrees with respect to the bulk. κ and $R\phi^o$ can sometimes be omitted from the notation. $S(hkl)$ means the substrate material S of crystallographic orientation (hkl).

When a reconstructed overlayer is formed, the atomic structure may be rotated by different angles relative to the substrate, depending on its rotational symmetry. The superlattice of the overlayer may grow at each of those angles in different parts of the surface, thus forming domains. Each domain will then be separated by a dislocation where the structure is out of phase. In some cases, domains may form even if the superlattice possesses the same rotational symmetry as the substrate, such as e.g. a $(\sqrt{2} \times \sqrt{2})$ R45^o (often written c(2×2)) structure on a cubic (1×1). Depending on the exact lattice points at which the superlattice starts to form, dislocations may form where domains are out of phase, as shown in Figure (2.4).

2.4 Segregation and surface composition in bimetallic alloys

Alloy compositions may be different in surfaces than in the corresponding bulk, depending on several factors [37]. A metal can have low solubility in other metals, which highly affects the arrangement of atoms of the different metals. Intermetallic compounds may form in some alloys if the solubility is high so that atoms of the two metals are arranged periodically. In other alloys, the two metals could be arranged more randomly. Furthermore, the solubility can be different in the surface than in the bulk. Different metals have different surface energies. If one of the alloy components has a significantly lower surface energy than the other, there will be preferential segregation of that component to the surface. Segregation is dependent on whether alloy formation is exothermic or endothermic, which depends on the relative interactions A-A, B-B and A-B and the relative sizes of the two alloy compounds A and B. If A-A and B-B interactions are stronger than A-B, then alloy formation will be endothermic, and segregation can occur. Segregation also depends on strain and temperature. McLean derived the following formula for surface segregation in bimetallic alloys called the Langmuir-McLean formula [42]:

$$\frac{X_A^{surf}}{X_B^{surf}} = \frac{X_A^{bulk}}{X_B^{bulk}} \exp\left[\frac{\sigma_B - \sigma_A}{RT}\right] \tag{2.15}$$

where X_A^{surf}, X_A^{bulk}, X_B^{surf} and X_B^{bulk} are molar fractions in surface and bulk of alloy components A and B, and σ_B and σ_A are surface energies of components B and A, respectively. Several mathematical models have been developed in an attempt to fully describe segregation phenomena, but they are far too complex to be included here. See e.g. [43] and references therein.

2.5 Oxidation

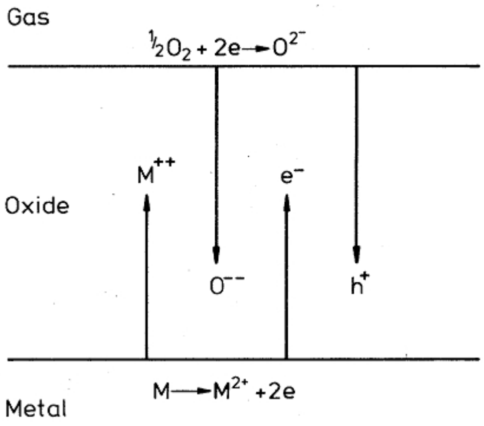

Figure 2.5: Diffusion processes for metal and oxygen ions as well as for electrons and holes during oxidation of a metal surface [44].

Metal surfaces can be oxidized in UHV by exposing them to low O_2 pressures and/or heating. Oxygen will then be adsorbed on the surface, and can eventually form a layer of metal oxide. A theory of oxidation of metals was established by Cabrera and Mott, which is a diffusion- limited theory [45]. It relies on transportation of electrons and electron holes through the growing oxide film. Upon completion of one layer, further growth of metal oxide can only occur if oxygen and metal ions are able to diffuse through the already exisisting metal oxide overlayer. Electrons can move through the metal substrate and ionize oxygen adatoms by the following reaction [44]:

$$\frac{1}{2}O_2(g) + 2e^-(metal) \rightarrow O^{2-}(adatom) \tag{2.16}$$

Metal ions can also be oinized accordingly [44]:

$$M \rightarrow M^{2+} + 2e^- \tag{2.17}$$

The Fermi levels of the metal and adsorbed oxide layer then align, and a uniform electric field is established in the oxide film due to the negatively charged oxygen atoms and the positively charged metal-oxide interface. Because no net electric current can pass through the film, electrons and positively charged electron holes will move in opposite directions through the film. These diffusion processes are illustrated in Figure (2.5). For oxidation to continue, both metal and oxygen ions must be able to overcome the diffusion activation energy barrier and diffuse through the film. The electric field lowers the diffusion barrier, but as the film grows the diffusion barrier increases to a certain point when no further oxidation is possible [36].

Oxidation of single crystal fcc (100) transition metal surfaces in UHV have shown that only a single layer is formed at typical temperatures and O_2 pressures which result in oxygen coverages of less than 0.5ML [46]. An oxidation model in which oxygen atoms are assumed to only occupy 4-fold hollow sites of the substrate has been developed, which describes results obtained from experiments [46]. Experiments in which binary alloys of metals have been oxidized have shown preferential oxidation of one of the alloy components [36].

3. Materials

When studying a material it is always a good idea to search for interesting results of other researchers. In this chapter, the most relevant experimental and theoretical results found in the literature are presented. No papers on PdCu(100) have been found, but some of its basic properties are presented in the first section along with relevant results from work with other PdCu surfaces. The other sections include relevant properties of Pd(100), Cu(100) and PdCu surface alloys, as these systems are expected to have properties comparable to those of PdCu(100).

3.1 PdCu(100) and other PdCu surfaces

Pd and Cu are both known to form face- centered cubic (fcc) crystals [47]. The same is also the case for PdCu single crystals [48]. Lattice parameters of Pd and Cu are 3,88Å and 3,62Å respectively [47]. The lattice parameter of a PdCu alloy is therefore expected to have a similar value. Figure (3.1) shows the fcc structure and the structure of the (100) surface. Note that the interatomic distance of the cubic structure of the (100) plane is the lattice parameter a divided by $\sqrt{2}$, thus it is expected to be somewhere between 2,6Å and 2,7Å for PdCu(100). PdCu alloys can form Cu_3Pd or PdCu single crystals [49]. However, it is not obvious whether or not a $Pd_{57}Cu_{43}$ alloy will form such compounds. That also means it is not easy to know the chemical composition of the surface. Segregation processes can further complicate the surface composition, as copper is known to segregate to the surface of PdCu alloys [50].

Loboda-Cackovic and co-workers have studied PdCu(110), and found that the surface initially is Pd- rich, with Cu segregation to the surface at temperatures above 550K, and that higher temperatures increases the top layer Cu content [48, 51, 52]. They also found that thermal treatment induces surface roughening and partial disordering [53, 54]. Their results are compatible with those of Miller et al., who studied a polycrystalline $Pd_{70}Cu_{30}$ membrane [10]. They found that the top layer was Cu- enriched upon annealing due to segregaion from the bulk, whereas the near- surface region was Pd- rich relative to the bulk for all annealing temperatures above 400K. The $Pd_{70}Cu_{30}$ membrane reached a maximum Cu content of more than 60% in the top layer at an annealing temperature of roughly 700K.

An important question is what type of oxide is formed when PdCu(100) is oxidized. One can get an idea of what might happen by comparing the heat of formation of different oxides. These are shown in Table (3.1), and indicate that formation of copper oxide is energetically favoured, with Cu_2O slightly more favoured than CuO. Oxidation could therefore cause further segregation of Cu to the top layer. Hammoudeh et al. reported that a PdCu(110) surface seemed saturated by atomic oxygen already after an exposure of roughly 7L [55].

Table 3.1: Heat of formation for relevant oxide compounds [47]

Compound	Heat of formation
PdO	-85,4 kJ/mol
CuO	-157,3 kJ/mol
Cu_2O	-168,6 kJ/mol

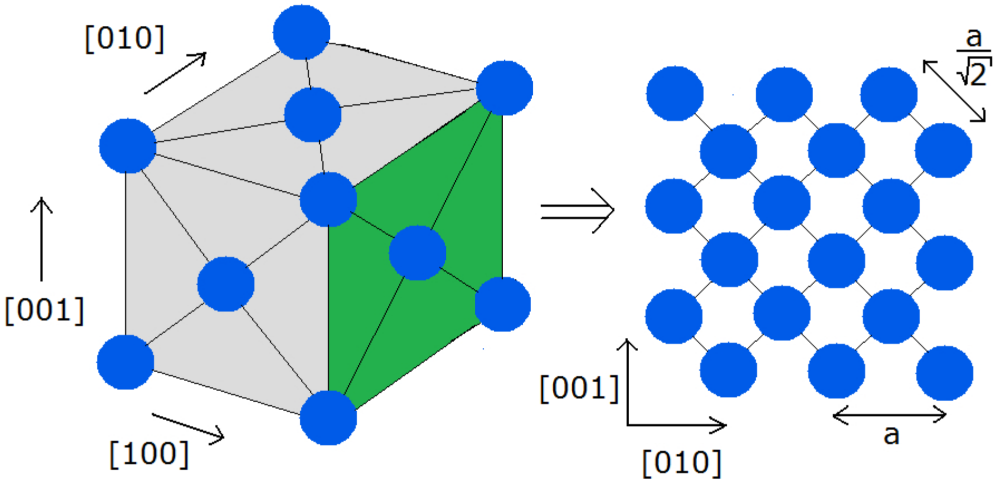

Figure 3.1: Left: The fcc crystal structure with the (100) plane indicated. Right: An illustration of the cubic structure of the (100) plane.

3.2 Pd(100)

Pd(100) surfaces have been heavily studied during the past decade in order to accurately describe its oxidation properties. Zheng and Altman found that oxidation of Pd(100) proceeds in four different stages with up to five different surface phases [56, 57]. In the first stage, a p(2×2) structure is formed, which is stable up to a coverage of 0.25ML. Above 0.25ML, it co-exists with a c(2×2) structure up to 0.5ML. Second stage involves oxygen filling subsurface sites, which causes Pd atoms to be ejected to the surface. This is caused by the fact that the areal density of Pd atoms in PdO is lower than in pure Pd. The excess Pd atoms are then able to diffuse across the surface and nucleate oxide islands. Oxide islands are found to be of the same height as step edges on the clean Pd(100) surface. Island growth stops when all subsurface sites are filled. In stage three, the surface reconstructs, forming a (5×5) structure below 400K and a ($\sqrt{5} \times \sqrt{5}$)R27^o structure above 400K (see Figure(3.2)). At that stage, the Pd-O bond strength is somewhere between that of chemisorbed oxygen and bulk PdO. Finally in the fourth stage, three- dimensional bulk- like PdO clusters are formed.

The ($\sqrt{5} \times \sqrt{5}$)R27^o was first thought to be of a structure similar to PdO(001), but further studies led Todorova et al. to suggest it is actually a strained layer of PdO(101) [58]. This was later confirmed although slightly modified by Kostelník et al., who found that the PdO(101) is shifted horizontally with respect to the Pd(100) plane [6]. Seriani et al. later confirmed by computational methods that the (101) orientation of PdO is the most stable on Pd(100), and also constructed a model that explains the Stranski- Krastanov growth mode [59]. The $(\sqrt{5} \times \sqrt{5})R27^o$ surface oxide can be stable at a wide variety of temperatures and pressures. Lundgren et al. identified a strong kinetic hindrance to formation of bulk PdO, even at ambient pressures [60]. Nevertheless, large agglomerates and bulk PdO has been observed for pressures above 1mbar [61].

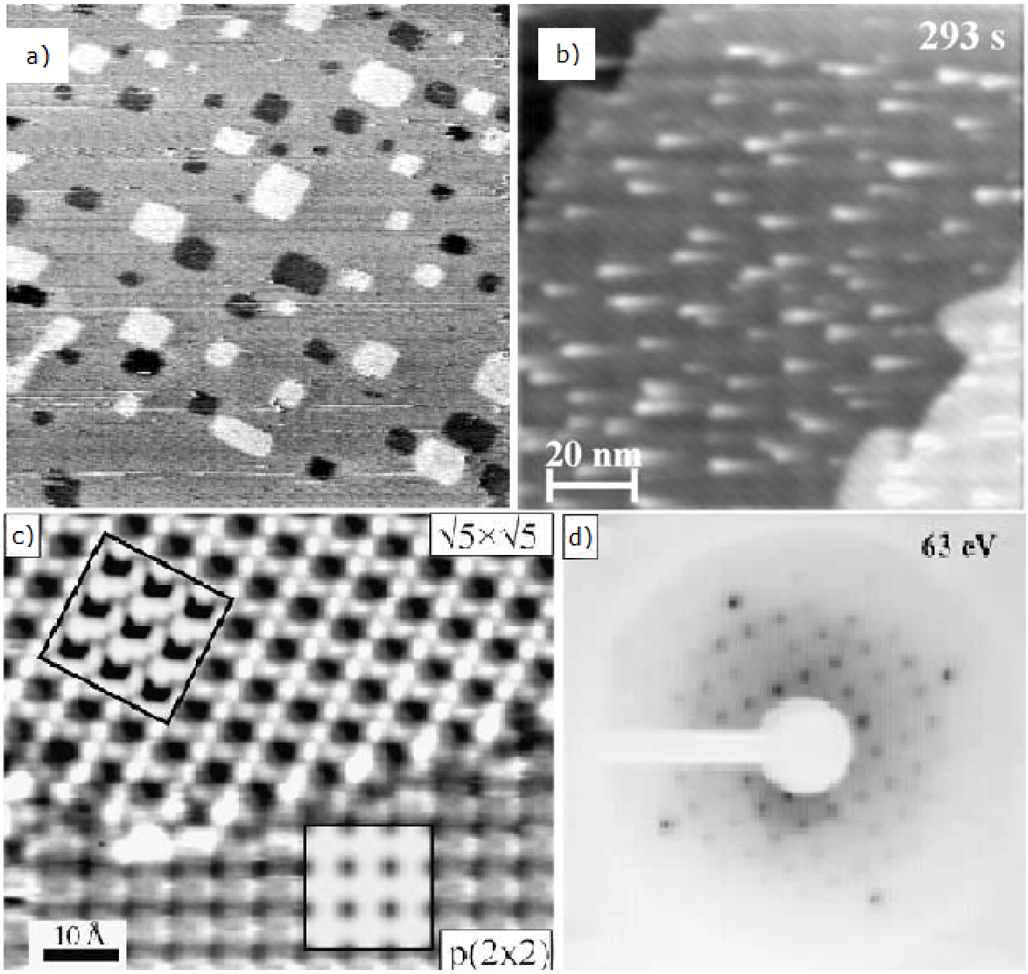

Figure 3.2: (a) STM image of metallic Pd(100) surface after reduction of oxide with CO. Adatom and vacancy islands are clearly oriented in the [010] and [001] directions [62]. (b) In- situ STM image of oxide clusters formed by oxidizing Pd(100) with NO_2 at 550K and $2 \cdot 10^{-8}$ Torr [57]. (c) STM image showing both the $(\sqrt{5} \times \sqrt{5})R27^o$ and $p(2 \times 2)$ structures [58]. (d) LEED pattern of the (5×5) structure at 63eV [57].

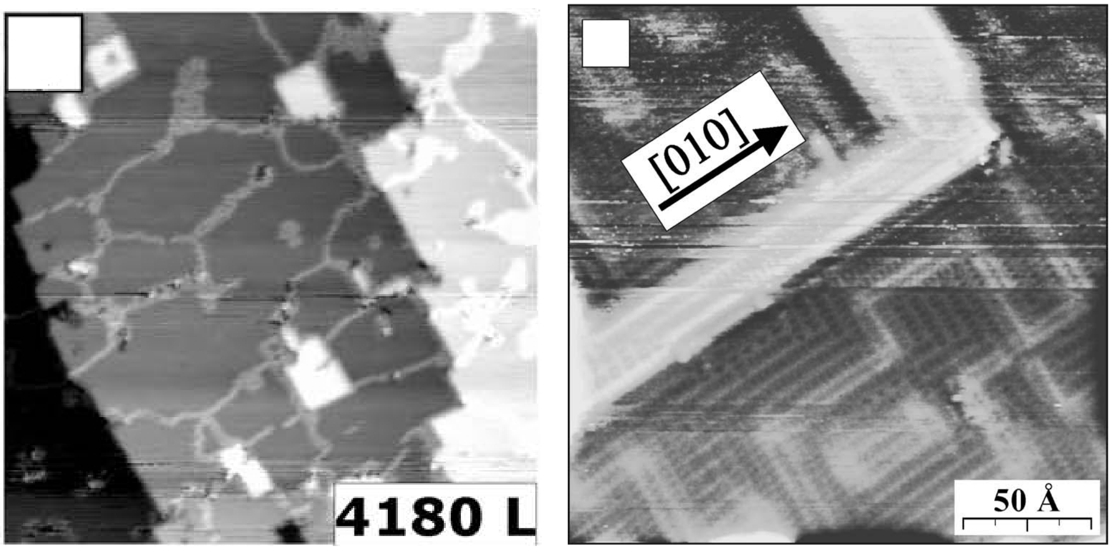

Figure 3.3: Left: In- situ STM image of Cu(100) oxidized at $8 \cdot 10^{-7}$mbar at 373K. Step edges and islands follow the [010] and [001] directions. Right: STM image of the $(2\sqrt{2} \times \sqrt{2})$R45^o structure on Cu(100) oxidized with $6 \cdot 10^5$L at $3.7{\cdot}10^{-2}$mbar O_2 at 373K. The image clearly shows that the structure grows in two domains. The bright area is an island of the same structure. Both figures are taken from [63].

3.3 Cu(100)

Copper is used in everything from water pipes and building construction to elecronics [64], and its oxidized form has found applications in catalysis [65], solar cells [66] and gas sensors [67]. Due to its many applications, both clean copper and its oxidation has been studied by several research groups. Oxidation of Cu(100) is a process quite similar to oxidation of Pd(100), as it goes through 3 phases of different structures [63, 68]. First, a c(2×2) is formed with oxygen atoms in four- fold hollow sites, which is stable up to a coverage of 0.3ML. Then the surface reconstructs into a $(2\sqrt{2}\times\sqrt{2})$R45^o missing- row structure that saturates at 0.5ML (see Figures (3.3) & (3.4). STM has revealed that this structure has two domains separated by boundary lines, and that 2D islands are formed by Cu atoms that are ejected to the surface, where they diffuse and nucleate islands or attach to pre-existing step edges [63]. Steps, islands and boundary lines all run in the <001>directions, as shown in Figure (3.3). Calculations support the experimental observations that oxide formed in stage two is highly stable, and that there is a strong hindrance towards further oxidation [69]. Similar to the $(\sqrt{5} \times \sqrt{5})$R27^o reconstruction on Pd(100), the $(2\sqrt{2} \times \sqrt{2})$R45^o reconstruction on Cu(100) also requires oxygen atoms to enter subsurface sites [69]. The third stage involves growth of 3D Cu_2O islands at high pressures [63]. Such 3D islands form several different shapes depending of temperature at pressures larger than 10^{-4} [70], and can later be reduced by annealing at high T, leaving nanoindentations on the surface [71]. It has been reported that 3D Cu_2O islands nucleate epitaxially at a pressure of $\propto 5$ $\cdot 10^{-5}$mbar, but they are randomly oriented at 150mbar [72]. Calculations on surface and subsurface oxygen [73, 74, 75] and kinetics of reconstruction and adsorption [64, 76, 77, 78] are also available in the literature, but they are too detailed to be presented here.

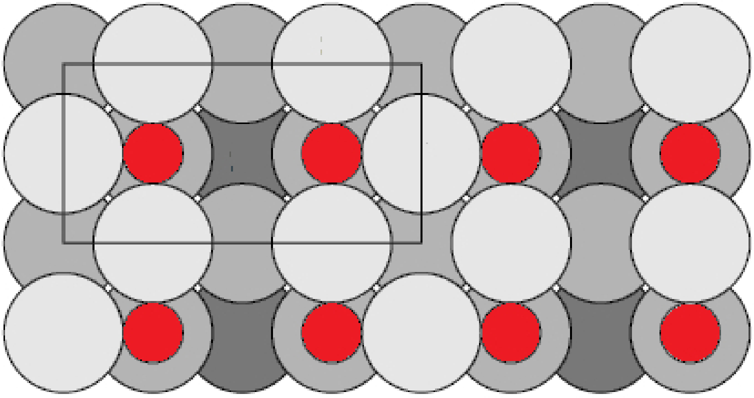

Figure 3.4: The $(2\sqrt{2} \times \sqrt{2})R45^o$ reconstruction. Cu atoms from the first, second and third layer are illustrated with different brightnesses. Red oxygen atoms occupy hollow sites. Notice that a row of Cu atoms is missing where the third layer Cu atoms are visible. The figure is taken from [73].

3.4 Pd on Cu(100)

Pope et al. found that deposition of 0.5ML Pd onto Cu(100) gives an incomplete surface alloy layer of c(2 × 2) LEED pattern, in which some Pd atoms are covered by overlayer islands [79, 82]. At 1ML, however, it was not a normal c(2 × 2) structure that was seen, but rather one with a p4g symmetry. Domains of normal c(2 × 2) and Cu- rich structures were also present on the surface. XPS revealed that positive core level binding energy shifts were observed for Pd, whereas they were negative for Cu, which is consistent with charge transfer from Pd to Cu [79].

This system has also been studied by STM by Murray et al. [80]. Figure (3.5) shows two of their STM images after deposition of 0.2ML Pd onto Cu(100). Protrusions are seen in the Cu(100) (1 × 1) structure, which they attributed to Pd atoms having replaced Cu atoms. These protrusions were imaged differently depending on imaging conditions. The ejected Cu atoms diffused across the surface and formed Cu islands on top of the alloy layer. At 0.35ML Pd (Figure (3.6)), Pd atoms formed rows in the [010] and [001] directions, and where such rows met, a c(2 × 2) structure was seen. At 1.10ML they saw a checkerboard c(2 × 2) alloy structure on terraces. When the coverage was 1.30ML, areas of p(2 × 2) started to form, but no p4g symmetry was visible with STM.

Several models were proposed in order to explain the p4g symmetry [80, 79, 81, 82, 83], but it was not until density functional calculations were performed that the structure seen after depositing 1ML Pd on Cu(100) was understood [84]. The structure consists of a clock- reconstructed p(2 × 2)-p4g alloy layer on top of an ordered c(2 × 2) alloy subsurface layer in registry with the Cu(100) substrate (see Figure (3.6)). The driving force for this reconstruction is minimization of energy by forming a structure that is in between a square (100) and a triangular (111) layer [84].

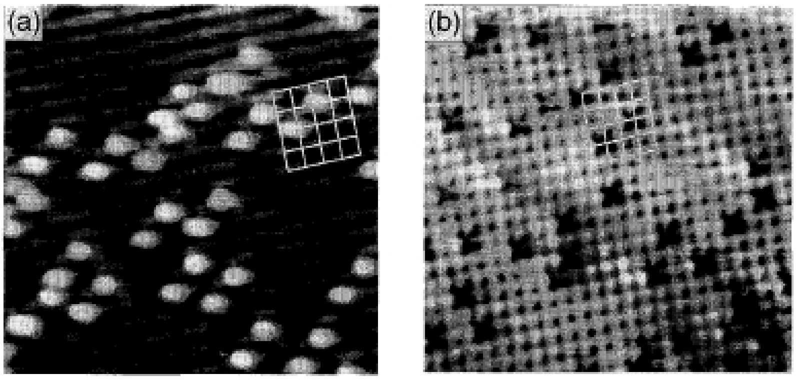

Figure 3.5: Left: STM image of protrusions in the Cu(100) after deposition of 0.2ML Pd. Right: A similar area after a tip change. The figure is taken from [80].

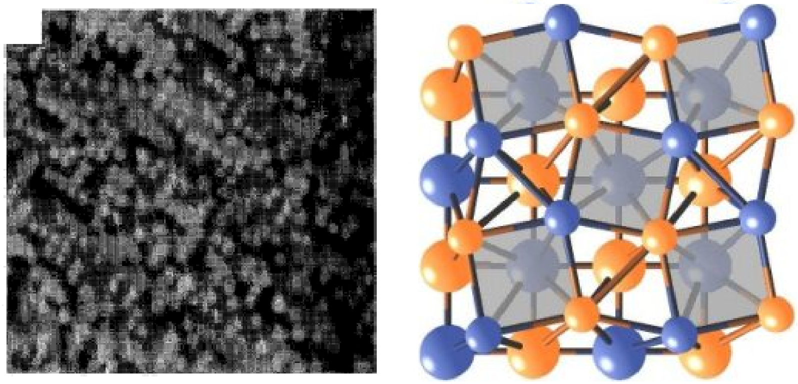

Figure 3.6: Left: STM image of 0.35ML Pd on Cu(100). Pd atoms form rows, and where rows meet, a c(2 × 2) structure is seen [80]. Right: A model of the c(2 × 2)-p4g structure present at 1ML Pd on Cu(100). Blue and yellow atoms denote Pd and Cu atoms, respectively. The figure is taken from [84].

4. Experimental techniques

This chapter describes the experimental techniques used in this thesis. The three techniques that have been used are Low Energy Electron Diffraction (LEED), Scanning Tunneling Microscopy (STM) and X- ray Photoelectron Spectroscopy (XPS). Their physical principles as well as fundamental instrumentation and theory will be explained in the following sections.

4.1 LEED

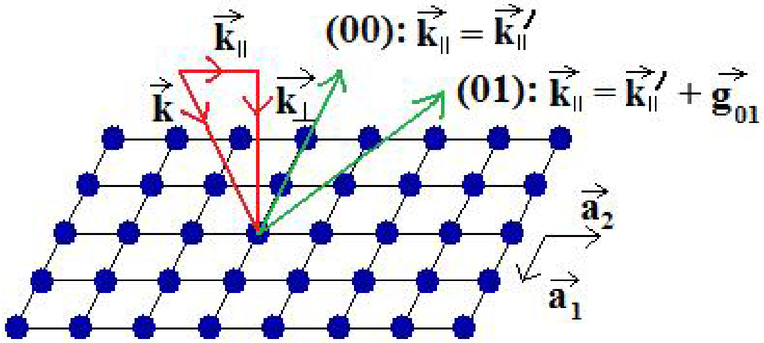

Figure 4.1: Illustration of diffraction from a surface in real space. The incoming waves with wavevectors $\vec{k} = \vec{k_{\parallel}} + \vec{k_{\perp}}$ are scattered into waves with wavevectors $\vec{k'} = \vec{k'_{\parallel}} + \vec{k'_{\perp}}$ [31].

Low Energy Electron Diffraction (LEED) is a technique commonly used to study surface crystallography [85]. Its name comes from the fact that electrons of energies typically below 200eV undergo diffraction as they are scattered by the atoms in the lattice of the sample surface. For comparison, electron energies of up to 1MeV are used in Transmission Electron Microscopy (TEM) [86]. These low energies is the reason why LEED is a very surface sensitive technique, as the electrons only penetrate their way into the first few atomic layers of the sample. It should be noted that LEED only works for well- ordered surfaces in which atoms form a lattice. If LEED is used on disordered surfaces nothing of interest will be seen since there is no periodic lattice that can cause construcive interference. In the case of a surface with repeating step edges, e.g. a cubic (510), the step edges can give rise to additional spots because there would be a repeating feature at every 5th atom along one direction in addition to the repeating lattice along the direction orthogonal to it, thus creating a (5x1) LEED pattern [85]. However, step edges or domain boundaries are normally not seen becuase they do not occur periodically and because they often occur with greater spacing than can be detected by LEED.

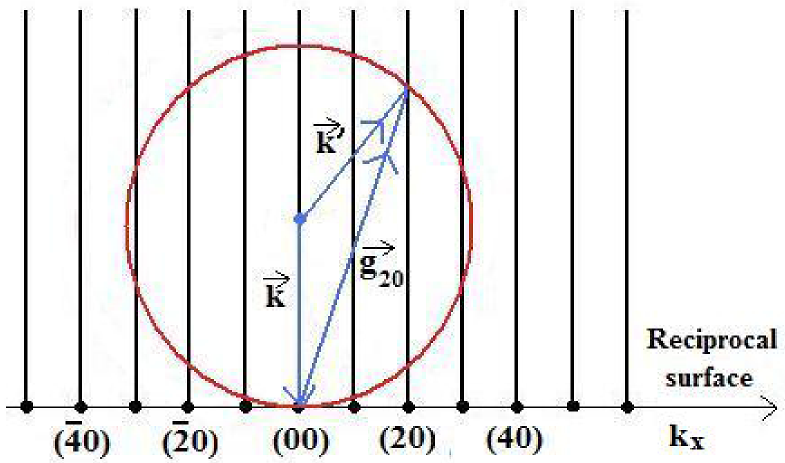

Figure 4.2: The Ewald sphere construction, which for this $\vec{k}$ gives diffraction spots from the $(\bar{3}0)$, $(\bar{2}0)$, $(\bar{1}0)$, (00), (10), (20) and (30) reciprocal vectors as well as several spots that are not seen in this figure, e.g. $(\bar{1}2)$ and $(2\bar{1})$ [31].

The diffraction phenomenon is explained by the Ewald sphere construction [35, 31, 85]. According to quantum mechanics, particles like electrons also display a wave nature because of their wave- particle dualism. Electrons therefore have a characteristic de Broglie wavelength λ and a corresponding wave vector:

$$\vec{k} = \frac{2\pi}{\lambda}\hat{\mathbf{k}} \tag{4.1}$$

where $\hat{\mathbf{k}}$ is a unit vector parallel to the direction of propagation. The radius of the Ewald sphere of the wave is given by $|\vec{k}|$, which according to quantum mechanics is related to the energy E in the following way [85]:

$$E = \frac{\hbar^2 k^2}{2m} \tag{4.2}$$

where m is the electron mass. The basis for the Ewald sphere construction is that electrons contributing to the diffraction pattern are elastically scattered. Since energy is conserved in elastic scattering, the following relation holds:

$$|\vec{k}| = |\vec{k'}| \tag{4.3}$$

Figure (4.1) shows how an electron wave with wavevector $\vec{k} = \vec{k'_{\parallel}} + \vec{k'_{\perp}}$ is scattered by a 2D Bravais lattice. Consider an incoming wave with wavevector $\vec{k}$ that undergoes scattering. The scattered wave is denoted $\vec{k'}$. It then follows from conservation of momentum that [31]:

$$\vec{k'_{\parallel}} = \vec{k_{\parallel}} + \vec{g_{hk}} \tag{4.4}$$

where $\vec{g_{hk}}$ is a surface reciprocal lattice vector. Figure (4.2) illustrates this for the case of $\vec{g_{hk}} = \vec{g_{20}}$. This explains why in Figure (4.2) both the incoming and scattered wave vectors are equal to the radius of the Ewald sphere. The rods displayed in Figure (4.2) indicate which of the reciprocal

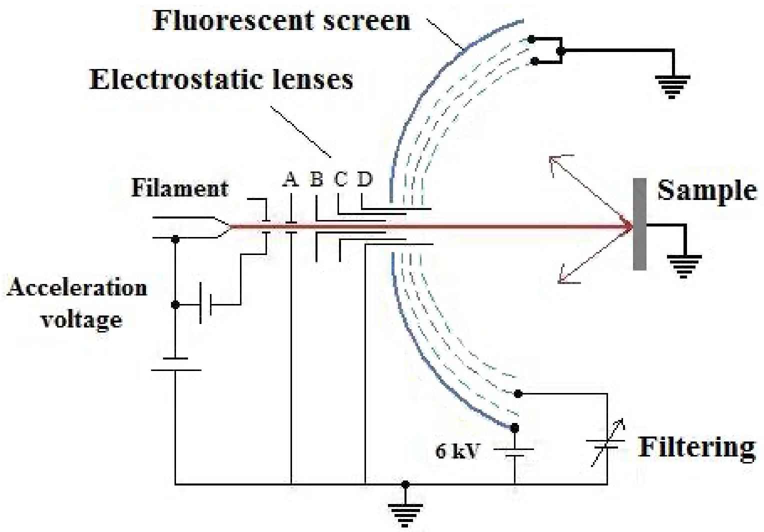

Figure 4.3: A typical LEED setup [35].

lattice vectors $\vec{g_{hk}}$ can contribute with a diffraction maximum. Every rod that intersects the Ewald sphere contributes with a single spot to the diffraction pattern, which is observed on a fluorescent screen. In the figure, only one surface dimension (x) is shown, hence the Ewald sphere is illustrated as a circle, but obviously the same phenomena occur in the other surface dimension (y) for different values of the k index of $\vec{g_{0k}}$. In this way, a 2D LEED pattern is formed. The number of LEED spots clearly depends on the radius of the Ewald sphere, which according to equation 4.2 is proportional to the square of the energy. Higher energy therefore gives more diffraction spots. From equations 4.2 and 4.1 it can easily be seen that typical LEED wavelengths are on the order of 1Å, which is similar to typical interatomic distances of crystalline solids.

Figure (4.3) shows a typical LEED setup. Electrons are emitted from a filament and accelerated by an electrostatic field in an electron gun. Their energy can be adjusted to the desired value by varying the acceleration field. On their way towards the sample, the electron beam is focused and adjusted by electrostatic lenses for optimal diffraction patterns. Normally the beam is pointed orthogonally towards the sample, meaning that the electron gun is at the center of the fluorescent screen. This makes the observed diffraction pattern as symmetric as possible, which makes interpretation easier. For this reason, the (00) diffraction spot is not seen unless the sample is rotated. Both inelastic as well as elastic scattering processes occur, and even though only elastically scattered electrons provide any information, as much as 99% of electrons could be scattered inelastically [85]. Inelastically scattered electrons appear on the screen only as a homogeneous background, hence it is desirable to prevent them from reaching the screen. This is achieved by an electrostatic grid indicated as filtering in Figure (4.3), carrying a negative voltage that is overcome by elastically scattered electrons, but not by inelastically scattered electrons which have lower energies. LEED requires vacuum conditions to avoid electrons from being inelastically scattered by gas particles between the sample and the detecting screen, because such electrons would only contribute to the background. The screen carries a positive voltage of about 6kV so that electrons are accelerated towards it.

In addition to information about the atomic structures in the sample, the brightness and clearness of LEED spots can in some cases give an estimate of the degree of order in the surface, because well-ordered surfaces result in a clearer LEED pattern than surfaces of less order. When an adsorbate is formed on top of another material by e.g. oxidation or deposition, superlattices may be formed as explained in chapter (2.1). Each individual superstructure will then form its own LEED pattern, and by comparing the brightness of spots corresponding to different structures, one could get an idea of which structure is expected to dominate the surface. After a sample has been cleaned by sputtering and annealing, one can check the crystallography with LEED. If a diffraction pattern is seen which corresponds to the bulk structure or reconstructed clean surface, one can assume that any overlayers have been sputtered away. LEED is also often routinely used to check the chrystallography before STM experiments are started.

4.2 STM

Scanning Tunneling Microscopy (STM) is an important technique in surface science that was invented by Gerd Binnig and Heinrich Rohrer in 1981. Their work earned them the Nobel prize in physics in 1986 together with Ernst Ruska [87]. The reason why STM is such a powerful technique is its ability to study surfaces at the atomic scale, providing information not only about large- scale features such as surface structure, but also individual atoms of the surface. This is done by using piezoelectric crystals to move a metal tip in two or three dimensions across a sample surface. A bias voltage is applied between the sample and tip, which sets up a tunneling current that can be used to create images of the surface of a conducting material. The sign of the bias voltage determines whether occupied or unoccupied surface states are measured.

Classically, electrons are not able to pass between two electrodes separated only by vacuum or air, because their energy is not sufficient to overcome the barrier. The left part of Figure (4.4) shows what the potential barrier and electron wave function look like when there is no bias voltage. The wave function then quickly decreases to very small values, hence the probability of finding the electron in the center of the barrier is close to zero. This is explained by solving the Schrödinger equation for an electron inside and outside of the barrier:

$$\hat{H}\psi = \left(-\frac{\hbar^2}{2m}\frac{d^2}{dx^2} + V\right)\psi = E\psi \tag{4.5}$$

The solutions are [85]:

$$\psi = \begin{cases} Ae^{ikx} + Be^{-ikx}, & \text{Outside barrier} \\ Ce^{ik'x} + De^{-ik'x}, & \text{Inside barrier} \end{cases} \tag{4.6}$$

where A, B, C and D are constants and x is the position. The wavenumbers k and k' are [85]:

$$k = \frac{2mE}{\hbar^2} \tag{4.7}$$

$$k' = \sqrt{\frac{2m(E-V)}{\hbar^2}} \tag{4.8}$$

where E is the electron energy and V is the barrier potential. It is evident from these equations that the wave function decays exponentially inside the barrier, as shown in Figure (4.4). When a bias voltage is applied, the wavefunction decreases more slowly inside the whole barrier, as in the right part of Figure (4.4), so that the probability of tunneling is increased. Tunneling probability can also be increased by making the barrier thinner. Since tunneling can occur both ways through the barrier, a net tunneling current is only obtained when a voltage is applied.

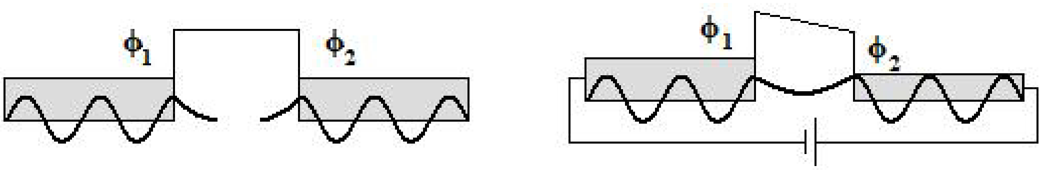

Figure 4.4: The wavefunction of an electron inside and outside a potential barrier. Left: Due to the exponential decay of the wavefunction inside the barrier, it may not cross the barrier if it is too thick. Right: A thinner barrier and an applied voltage enables electrons to tunnel through the barrier, and a current is set up [85].

It has been found that the tunneling current across a one- dimensional vacuum barrier is approximately [88]:

$$I \propto \frac{V}{d}\ exp(-Kd\sqrt{\overline{\phi}}) \tag{4.9}$$

where d is the barrier width, $\overline{\phi}$ the average work function and K a constant of approximately 1,025Å^{-1}eV$^{-1/2}$. Notice the strong dependence on the distance between tip and sample. The dependence on the work function also tells us that tunneling properties vary amongst different materials. This one- dimensional model is sufficient to describe how tunneling works and how it can be achieved, but a much more complex model is required to understand the exact nature of the phenomena that occur during STM imaging. A three- dimensional model has been worked out by Tersoff and Hamann, in which 1st order perturbation theory has been used to express the tunneling current as [89]:

$$I = \frac{2\pi e}{\hbar}\sum_{\mu,\nu} f(E_\mu)[1 - f(E_\nu + eV_{bias})]|M_{\mu\nu}|^2\delta(E_\mu - E_\nu) \tag{4.10}$$

where $f(E)$ is the Fermi function and $M_{\mu\nu}$ the matrix element for tunneling between eigenstates ψ_{mu} in the tip and ψ_{nu} in the sample with corresponding eigenenergies E_μ and E_ν. The expression for the tunneling matrix elements is [89]:

$$M_{\mu\nu} = \frac{\hbar^2}{2m}\int(\psi_\mu^*\vec{\nabla}\psi_\nu - \psi_\nu\vec{\nabla}\psi_\mu^*)\,\mathrm{d}\vec{S} \tag{4.11}$$

where the integration is done over any surface lying entirely within the barrier region. In their model, Tersoff and Hamann assumed a spherical tip similar to the one in Figure (4.5). The following expression was chosen for ψ_ν [89]:

$$\psi_\nu = \frac{1}{\sqrt{\Omega_s}}\sum_G a_G\ \exp[z\ \sqrt{\kappa^2 + |\vec{\kappa_G}|}]\ \exp[i\,\vec{\kappa_G}\cdot\vec{x}] \tag{4.12}$$

where Ω_s is the sample volume, a_G are of order unity, $\kappa = \hbar^{-1}(2m\phi)^{1/2}$, z is the z coordinate and $\vec{\kappa_G} = \vec{k_\parallel} + \vec{G}$ where $\vec{k_\parallel}$ is the surface Bloch wave vector of the state and $\vec{G}$ is a surface reciprocal lattice vector. For ψ_μ they chose [89]:

$$\psi_\mu = \frac{1}{\sqrt{\Omega_t}}c_t\,\kappa R e^{\kappa R}(\kappa|\vec{r} - \vec{r_0}|)^{-1}e^{-\kappa|\vec{r}-\vec{r_0}|} \tag{4.13}$$

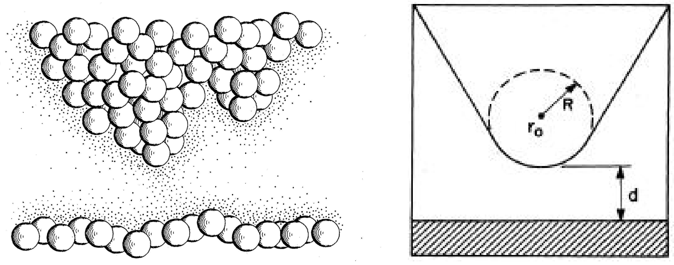

Figure 4.5: Left: Example of what a real tip may look like. Tunneling from both subtips is possible, but the current will be largest for the one closest to the sample [90]. Right: The spherical tip used in the model of Tersoff and Hamann [89].

where Ω_s is the probe volume, R is the tip radius, $\vec{r}$ is the tip radial vector and $\vec{r_0}$ is defined as the tip center of curvature. From these wave functions they could calculate $M_{\mu\nu}$ and arrive at the following expression for the tunneling current [89]:

$$I = 32\pi^3\hbar^{-1}e^2V\phi^2D_t(E_F)R^2\kappa^{-4}e^{2\kappa R}\sum_{\nu}|\psi_{nu}(\vec{r_0})|^2\delta(E_\nu - E_F) \tag{4.14}$$

where D_t is the density of states per unit volume of the tip. The sum expression in equation (4.14) is the local density of states of the sample, evaluated at $\vec{r_0}$ [91]. Comparing this to equation 4.11 for the one- dimensional case, the two expressions reveal an equal dependence on V and similarly strong dependence on the work function. However, the important feature of equation (4.14) is its incorporation of tip geometry, which plays a key role in STM experiments.

In their model, Tersoff and Hamann assumed a spherical tip of a certain radius. This is close to the ideal tip, which has only one atom at the very end. However, in real life the tip may possess a completely different geometry of complex character. Figure (4.5) gives an example of what a tip could look like during imgaging. If one has a multiple tip, tunneling is possible between every single subtip, meaning that every surface feature appears more than once on the image, possibly with different intensities. It is also possible to have a somewhat blunt tip in which several atoms are equally close to the sample surface. There is then a possibility that certain surface formations are smaller than the area of the tip, causing the tip itself to be imaged instead of the sample. Despite all the challenges STM can offer, it is perfectly possible to obtain a tip of reasonable quality. Tips are usually made out of W or a Pt/Ir alloy. The most common fabrication methods are electrochemical etching or simply cutting a metal wire at an angle. While scanning, the tip geometry can change if it picks up an atom from the surface or if atoms loosen from it. STM requires samples that are prepared in such a way as to make them as flat as possible, which usually includes series of sputtering and annealing.

Figure (4.6) shows the principle of operation of a tunneling microscope. Piezoelectric materials have the ability to stretch or compress when an external voltage is applied to them, or vice versa. Fortunately for us, voltage is something we can control very precisely, which means we can also precisely control the stretching and compression of piezoelectric materials. The tip can therefore be controlled so accurately that, in principle, a lateral resolution of less than 10^{-11}m and a vertical resolution of about 10^{-12}m can be achieved [85]. There are two ways of operating the microscope. One can scan

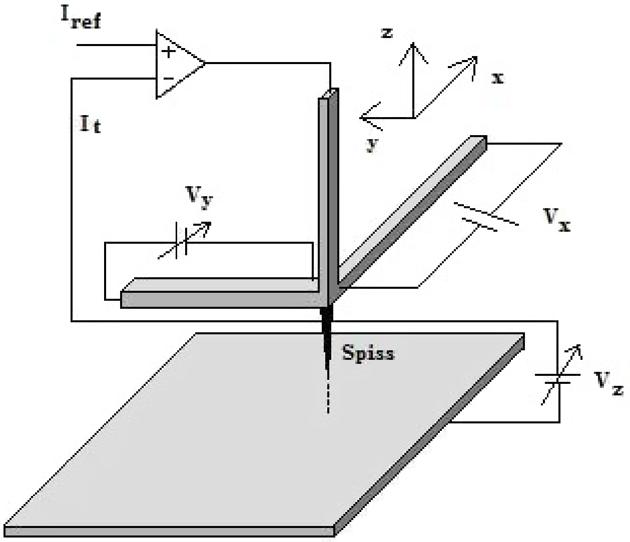

Figure 4.6: The principle behind STM. Voltages V_x and V_y are applied to the piezos in order to move the tip across the surface, whereas V_z moves the tip orthogonally to the surface when scanning in constant current mode [33].

the tip at constant z value and measure a changing tunneling current due to changing separation. Alternatively one can use a feedback loop to make the tip adjust the separation to the contours and electronic density of states of the surface in such a way that the tunneling current is constant, thus measuring a changing z value. See Figure (4.7) for an illustration of the two modes. STM can be performed both in vacuum and ambient conditions, but experiments are however often performed in vacuum. Surface studies of clean metals requires UHV since they would otherwise become oxidized very quickly, i.e. the few Å [85] of space between the tip and sample is usually vacuum.

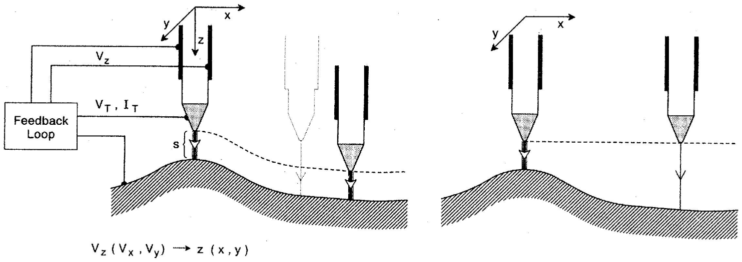

Figure 4.7: Left: Constant tunneling current and a feedback loop allows the tip to follow the contours of the surface. Right: Scanning at constant z and varying tunneling current [90].

4.3 XPS

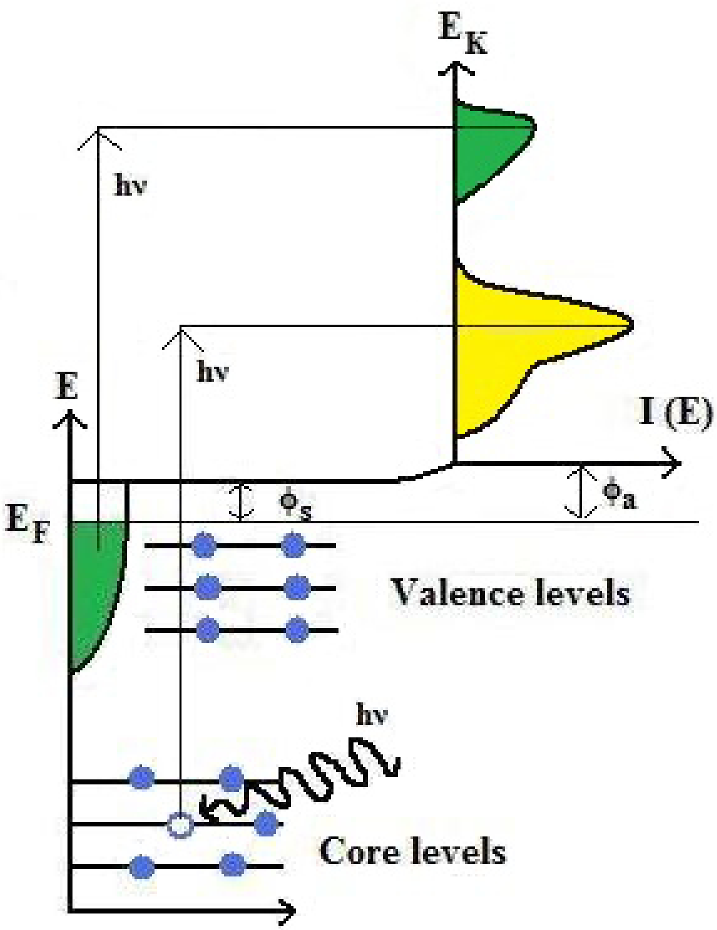

Figure 4.8: Illustration of how photoelectrons from core levels and the valence band of a solid are converted into an $I(E_B)$ spectrum in the analyzer. The figure is adapted from [92] and [93].

X- ray Photoelectron Spectroscopy (XPS) is a very useful technique in surface science, as it provides both qualitative and quantitative information. It is based on the photoelectric effect, which enables an incoming photon to eject an electron from its atom e.g. in the surface of a solid. Such ejected electrons are called photoelectrons. The photoelectric process will only occur if the energy of the incoming photon is higher than the electron binding energy, i.e. the so- called Einstein equation must be satisfied [85]:

$$E_B = h\nu - E_K \tag{4.15}$$

where E_B is the electron binding energy, ν es the frequency of the photon and E_K is the kinetic energy of the ejected electron. If $h\nu > E_B$, the emitted electron will carry a kinetic energy equal to $h\nu - E_B$, which can be measured by a photoelectron analyzer. When photoemission from a solid sample is considered, a photoelectron also needs to overcome the work function, ϕ_S, to be able to escape from the sample. The Einstein equation then becomes [85]

$$E_B = h\nu - E_K - \phi_S \tag{4.16}$$

On its way to the analyzer, the electron is accelerated or decelerated by the work function difference $\phi_S - \phi_A$, where ϕ_A is the work function of the analyzer, which in general is not equal to ϕ_S [86]. By calibrating the analyzer , the correct value for E_B can be found. Figure (4.8) illustrates the theory of how the photoelectric effect can provide binding energy spectra. The resulting spectra are plots of intensity versus binding energy. Binding energy reveals information about chemistry and surface composition, whereas intensity provides quantitative information. Although X- rays penetrate deep into the sample and may give rise to photoelectrons in the bulk, only photoelectrons from the topmost surface region can escape into the vacuum and be detected. XPS is thus a very surface sensitive technique. The electron mean free path varies amongst different materials, and also depends on the kinetic energy of the electron, as shown in Figure (4.9). Hence surface sensitivity is optimized at a certain photon energy, corresponding to the minimum photoelectron mean free path.

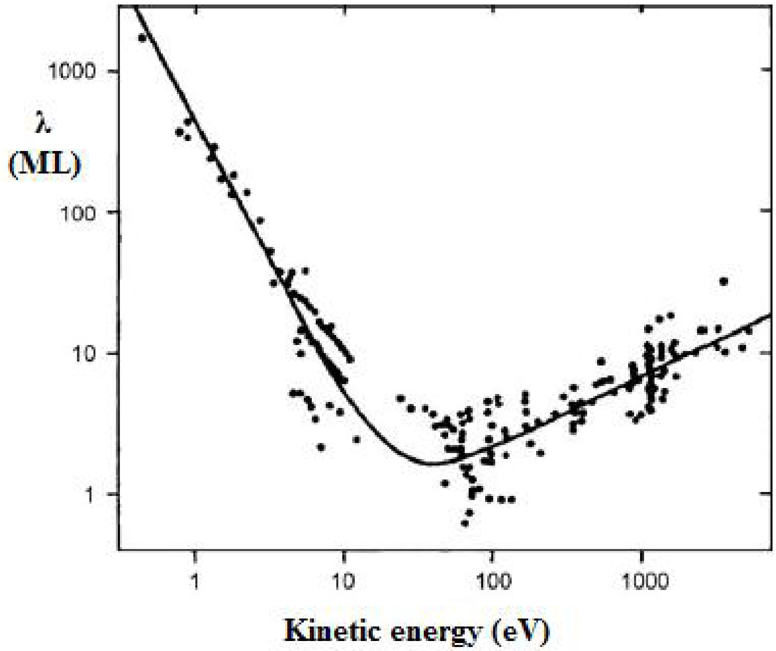

Figure 4.9: Mean free path of electrons in monolayers as a function of kinetic energy [94]. Each point in the graph represents an electron state of a certain material.

There are basically two common ways of generating X- rays for XPS experiments. The simplest way is to use an x- ray source and analyzer that can be connected to a normal UHV chamber in the same way as LEED and STM instruments. An X- ray anode is then used to accelerate electrons onto a target material, which emits fluorescence X- rays with a fixed energy [85]. The other way of generating X- rays for XPS is to use a beam of electrons at relativistic speed in a synchrotron

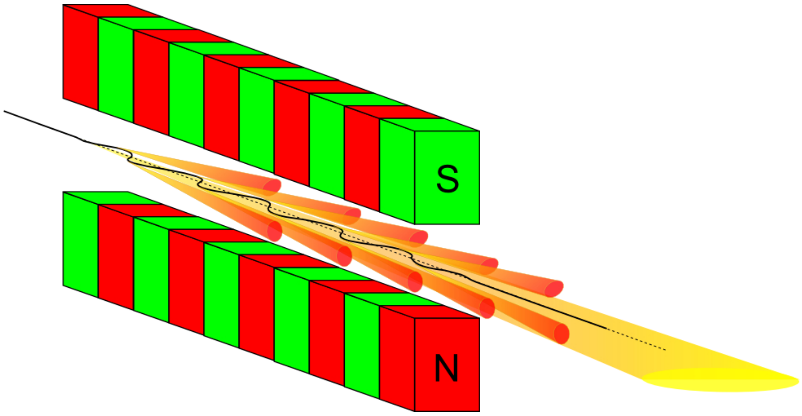

Figure 4.10: Illustration of how X- rays are produced by an undulator [95]

facility. A synchrotron is a large ring through which an electron beam is directed by several magnets. Connected to the ring are several beam lines with stations where one can perform experiments. Undulators are often used in synchrotrons to produce X- rays [96, 97]. They consist of several magnets of alternating polarity (Figure 4.10), and cause electrons to be accelerated and thus emit radiation. The energy of the emitted photons can be controlled by adjusting the distance between the two rows of magnets in the undulator. Whereas the anode is only capable of producing X- rays with one energy, the undulator can produce X- rays of any energy. Surface sensitivity is therefore much greater for synchrotron- based X- rays, since it allows use of the optimal photon energy.

An X- ray analyzer is shown in Figure (4.11). Photoelectrons are focused and decelerated or accelerated so that only those of energy higher than a fixed pass energy reach the hemispherical analyzer, in which an electrostatic field causes electrons of high energy to be less curved than those of low energy, so that they hit the detector at different points. The detector can then count how many electrons hit each single detection point, and a spectrum is obtained.

Theoretically, photoelectrons originating from core levels of atoms carry information about their binding energies, which have certain discrete values for each core level electron state. However, photoemission peaks in XPS spectra do not appear as having a single value, but rather as continuous curves with a certain peak width. After a core electron has been ejected, the resulting core hole has a certain lifetime before the atom relaxes and the core hole is filled by an electron from a higher state. The peak broadening due to core hole lifetimes can be found using Heisenberg's uncertainty principle [85]:

$$\Gamma = \frac{h}{\tau} \tag{4.17}$$

where Γ is the peak with in eV and τ is the core hole lifetime. Instruments also contribute to peak broadening because they have finite energy resolution. Lifetime broadening gives a Lorentzian line shape while instrumental effects give a Gaussian line shape. Metals have an assymetric contribution to line shapes on the high E_B side originating from photoelectrons losing a portion of their energy to excite valence electrons into the conduction band. Always present in the spectra is also the background, which comes from photoelectrons that have undergone inelastic scattering on their way to the analyzer. By combining these contributions, one can fit the photoemission spectra [85].

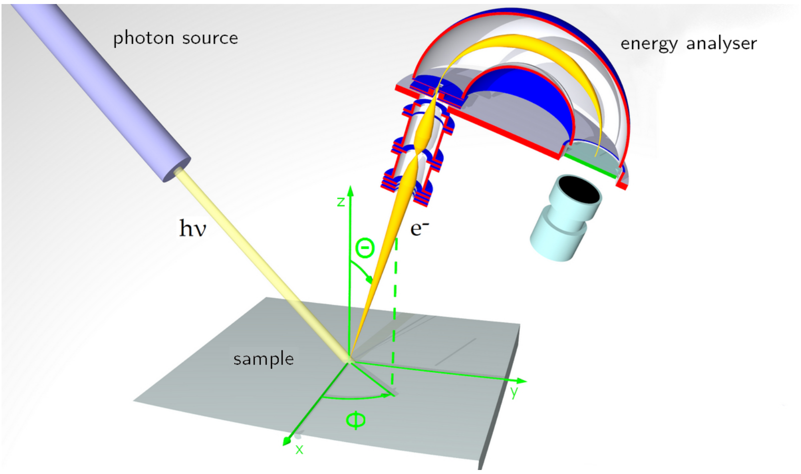

Figure 4.11: A typical XPS analyzer [98].

Overlapping of different peaks is not the only issue when analyzing XPS spectra. Some peaks could arise from physical phenomena that one is not particularly interested in. Multiplet splitting occurs when the valence band of the system has unpaired electrons [86]. After ejection of a core electron, another unpaired electron becomes present in the atom, which may have spin up or down. Depending on the spin of these unpaired electrons, there may or may not be exchange interactions between them, and this causes the peak to be split into two or more peaks. The Pd 3d level is an example of this, as it in the final state is in a configuration with an unpaired spin s and angular momentum $l = 2$. There is then a coupling effect between the two, which results in permitted values of the resultant angular momentum $J = 2 \pm \frac{1}{2}$ [86]. This explains why the Pd 3d is split into Pd $3d_{5/2}$ and Pd $3d_{3/2}$.

Even though core level electrons do not participate in chemical bonding, their binding energies are affected by their chemical environment, which is highly complex. Both neighbouring atoms and valence as well as other core level electrons can induce so- called core level shifts, which shift the binding energy towards higher or lower values [85]. Additional peaks will therefore appear for atoms that are chemically bonded to e.g. an adsorbate, and if there are several types of possible adsorption sites, each of those sites will contribute with its own peak. One way of explaining chemical shifts is to use the charge potential model [85]:

$$E_B = E_B^o + Cq_i + \sum_{j \neq i} \frac{q_j}{r_{ij}} \tag{4.18}$$

where E_B^o is a reference energy, C a constant, q_i the charge on atom i and q_j the charge on atom j at distance r_{ij}. Atoms located in the surface are only bound to other atoms on one side. This causes a binding energy shift for core electrons called the Surface Core Level Shift (SCLS), which produces a surface component in addition to the normal bulk component [85]. Other peak- generating mechanisms worth mentioning are shake-up and shake-off satellites, Auger emission and surface plasmon losees [86]. By comparing intensities of peaks for different sample preparations, one can gain a lot of knowledge about its surface. This is done using available software with fitting algorithms which fit each curve by convergence from initial values.

5. Instruments

5.1 The vacuum chamber

All experiments involving STM were performed in ultra high vacuum conditions inside the stainless steel vacuum chamber (Omicron) shown in Figure (5.1) Instruments are connected to the chamber using flanges which are sealed by copper gaskets to prevent leakage. A full list of instruments connected to the chamber is given in Table (5.1). Proper UHV can only be obtained after the chamber has been subject to bake- out, during which it is kept at an elevated temperature for more than 20 hours while pumping. Temperatures higher than the boiling point of water are maintained by heating filaments located inside the solid frame on which the chamber is resting. Insulating walls are placed around it, forming a furnace, so one does not have to heat up the whole lab. The purpose of performing a bake- out is to evaporate as much gas from the inside of the chamber walls as possible. Ideally one would like to have a perfect vacuum with zero pressure, but that is impossible to achieve because particles continually desorb from the chamber walls. After bake- out and sufficient pumping, an equilibrium is established. The pressure then stays constant because the amount of particles pumped out equals the amount of particles that desorb. This equilibrium is called the base pressure, and is roughly $8{\cdot}10^{-10}$mbar for this chamber.

5.2 Pumps

Several different pumps are used to obtain UHV, each with their own specific advantages and ways of pumping. In this UHV system there is one turbomolecular pump (turbo pump), one ion pump and one Titanium Sublimation Pump (TSP). The turbo pump is purely mechanical, and consists of blades rotating at 1000Hz that force the particles out of the chamber. To prevent it from being damaged by large differential pressures, and to support it in reaching very low pressures, another mechanical pump is used as a backing pump so that the turbo pump is not exposed to ambient pressures. The pump is automatically ventilated by nitrogen gas flowing through it to prevent oil from reaching the inside of the chamber. A valve can isolate the chamber from the turbo pump, and after the turbo pump has been switched on it takes roughly two hours before one can be certain the pressure in the pump is low enough to allow the valve to be opened again. The turbo pump is used whenever one is not performing STM, as well as for pumping the load lock and argon gas, as illustrated in Figure (5.2). Due to vibrations caused by the turbo pump and its backing pump, both of them should be switched off while doing STM, as imaging otherwise will be disturbed by noise. In addition to the main turbo pump there is also another turbo pump which is used when changing oxygen gas.

The ion pump ionizes gas atoms by electron bombardment, after which the ions are accelerated

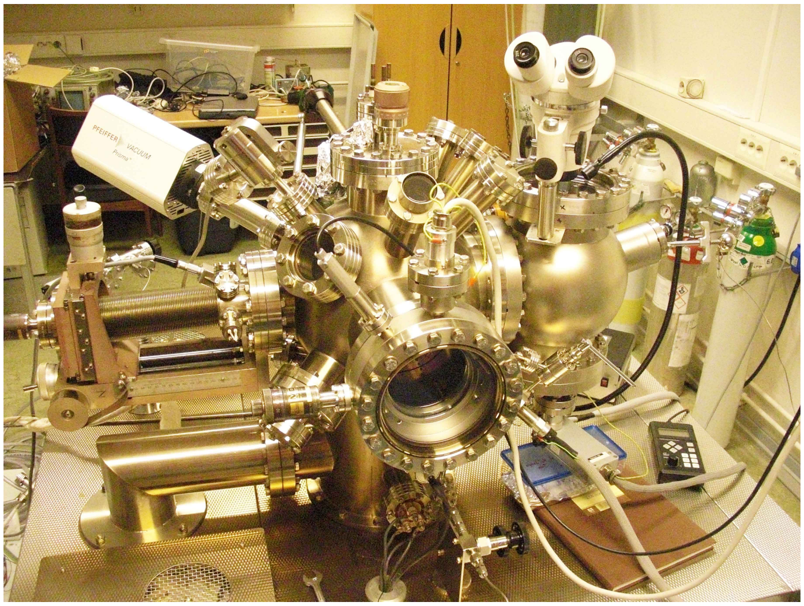

Figure 5.1: The vacuum chamber

onto an electrode by an electric potential of 7kV. They are essentially sputtered onto the electrode where they are trapped by physisorption or chemisorption. In this way atoms and molecules are removed from the UHV by a process that does not involve any moving parts. This makes the ion pump ideal for STM systems, as it does not produce any vibrations or other noise that can interfere with the STM imaging. While doing STM, the ion pump is the only instrument that maintains the low pressure. However, its principle of operation allows it to only run in very low pressures. If pressure becomes too high, the amount of particles captured could rise to a level at which the pump is damaged and becomes disfunctional. For this reason the ion pump is only run when pressure does not exceed $2{\cdot}10^{-8}$mbar.

The last pump is the TSP, which simply consists of three titanium filaments. By passing an electric current of about 50A through one of the filaments, the sublimation temperature is reached, and titanium is evaporated. A thin film of titanium is then formed on the chamber walls and any other surface which is directly facing the TSP. Pure titanium is highly reactive towards several types of gas atoms and molecules expected to be present in the background pressure. When these particles are adsorbed on the Ti film they react with it, forming e.g. TiO_2, and are thus pumped. This process continues until the Ti film is covered by particles, at which point a new film of Ti needs to be deposited. For this reason the TSP is set to run automatically for one minute every eight hours. Since one wants to avoid getting titanium on samples and electrical components, the TSP is safely located behind a screen at the bottom of the chamber. Only one Ti filament is used at a time, but for practical reasons there are two additional filaments for backup. Then one does not have to ventilate the chamber to change to a new filament unless all three need to be replaced. The TSP is only switched on between each lab session.

Table 5.1: Instruments connected to the vacuum chamber.

Instrument	Purpose
Ion pump	Pumping
Turbo pump	Pumping
Titanium sublimation pump	Pumping
Mechanical pump	Prepumping for turbo pump
Another turbo pump connected to oxygen circuit	Changing oxygen gas
Valves between turbo pump and argon circuit	Changing argon gas
Ion gauge	Pressure monitoring
Sputter gun	Sputtering
Leak valves	Introduction of Ar and O_2 gas
LEED apparatus	LEED
STM apparatus	STM imaging
Manipulator	Move and rotate samples
Manipulator filament and high voltage source	Thermal treatment of the sample
Wobblestick	Moving samples bewteen instruments
Sample carousel	Storage of samples and tips
Loadlock	Insertion of new tips or samples
Titanium evaporator	Evaporation of titanium
Mass spectrometer	Leak testing

5.3 Pressure monitoring and leak testing

5.3.1 Ion gauge

The pressure is continually monitored by an ion gauge. Its principle of operation is very similar to that of the ion pump. Electrons are emitted thermally from a filament at a certain current. Gas particles are ionized by electron bombardment and accelerated towards a grid by an electrical potential. The electrical current constituted by the ions hitting the grid can be measured, and reveals the pressure if the instrument is correctly calibrated.

5.3.2 Mass spectrometer

If one suspects leakage somewhere in the chamber, a mass spectrometer is used for leak testing. The mass spectrometer ionizes gas particles by electron bombardment, before they are accelerated by an electromagnetic field towards an analyzer. Atoms with different masses are sorted and counted by the analyzer so one can what type of atoms are present in the chamber. Small amounts of helium can then be sprayed onto different parts of the chamber, and the mass spectrometer will reveal if helium reaches the inside of the chamber. Hence one determines whether or not there is a leakage and also its location. Helium is chosen because it is a noble gas which diffuses easily, does not react with anything and because it is not already present in the chamber.

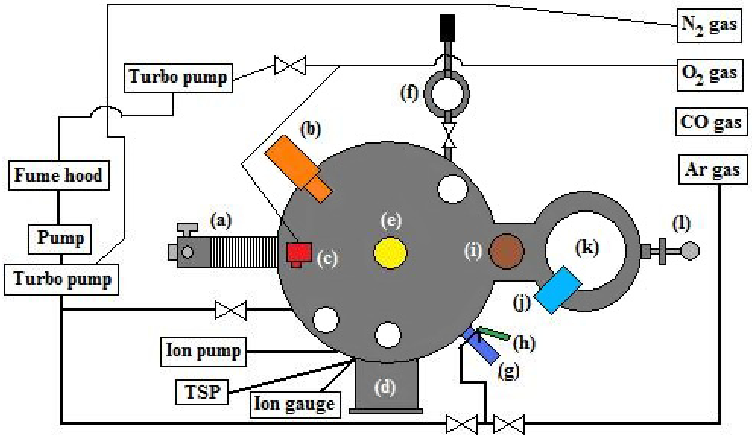

Figure 5.2: An illustration of the whole vacuum system. (a) Manipulator; (b) Mass spectrometer; (c) Valve for O_2 gas; (d) LEED; (e) Ti evaporator (not used); (f) Load lock for insertion of new tips or samples; (g) Sputtering gun; (h) Valve for Ar gas; (i) Sample carousel; (j) STM binoculars; (k) STM; (l) Wobble stick.

5.4 Sample preparation

5.4.1 Sputtering gun

The sample was cleaned by cycles of sputtering and annealing. Sputtering is essentially to bombard the sample with charged particles of sufficient energy to knock atoms from the sample into the vacuum. By this technique the topmost atomic layers are removed, exposing the the clean bulk of the sample. Sputtering is usually done with Ar since it is a noble gas and one therefore avoids contamination of the sample as Ar does not react chemically with it. The sputtering gun ionizes the argon atoms by bombarding them with electrons. Electrostatic lenses are then used to accelerate the Ar^+ ions towards the sample with an adjustable energy given by the voltage.

5.4.2 Thermal treatment

On the manipulator, right behind the sample holder, there is a filament through which currents up to 2A may pass. The filament is then heated by the electrical resistance and starts to glow. Before experiments started, it was found that a filament current of 1,6A and a voltage of 5,6V gave a stable sample temperature of 300^{o}C. In order to heat the sample to higher temperatures, one needs to bombard it with electrons by setting up an emission current of a few mA between sample and filament. This is done by applying a voltage of 1000V on the sample and pass a current through the filament. There is no instrument on the manipulator that can measure the temperature, so this has to be done from outside of the chamber using a pyrometer. A pyrometer can measure the thermal radiation j emitted by the sample, and the temperature is then found using:

$$j = \epsilon \sigma T^4 \tag{5.1}$$

where σ is the Stefan-Boltzmann constant and ϵ is the emissivity of the sample material, which is entered in the pyrometer. The pyrometer used in all experiments can only determine temperatures of 600^oC or above. Another pyrometer was therefore used to obtain the correct values for obtaining a temperature of 300^oC.

5.5 LEED and STM

5.5.1 LEED

The LEED apparatus consists of an electron gun that accelerates electrons orthogonally towards the sample, where they are scattered. A diffraction pattern is then visible on a fluorescent screen, as explained in chapter (4.1). Four electrostatic lenses and a Wehnelt electrode can be adjusted to optimize the intensity and sharpness of the spots. Whenever the electron energy is changed, the lenses need to be readjusted. All LEED images in these experiments were taken with a screen voltage of 6kV. The screen itself is manually moved close to the sample. Although light is switched off in the lab to make spots as clear as possible, some spots only appear clearly on images. A standard digital camera (Casio EX-S10) placed on a stand was used to record all LEED images. For optimal image quality the camera was set to 10 megapixels, slow shutter speed and high light sensitivity.

5.5.2 STM

The STM consists of two main parts, a scanner and a coarse movement unit, that rest on a suspended platform as illustrated in Figure (5.3). The scanner, consisting of three piezoelectric crystals, is used to move the tip in three dimensions across the surface during scanning. An area of roughly 500x500 nm^2 can be reached by the scanner without using the coarse movement unit. The coarse movement unit is used to move the sample to and from the tip, and also sideways so that different areas can be scanned. A remote control is used to control the coarse movement unit, whereas the scanner is controlled by a computer. When approaching the tip, an external microscope is used while moving the sample quite close. Automatic stepwise approach is then used until a tunneling current is measured by the STM. Both tip and sample are resting on sample holders which can be grabbed by the manipulator and lifted out of the STM. This is only done when the tip and sample are far apart.

Figure (5.3) shows that the STM is located on a platform. Unlocking this platform by pulling down a lock mechanism beneath the STM allows it to hang from four springs which then are its only supports, thus damping vibrations. Several magnets are placed circularly around the STM. When the STM vibrates, these magnets induce an Eddy current in copper plates attached to the STM, which generates an opposing force to the vibrations, thus dampening them.

Scanning is controlled using the STM software. Parameters that can be adjusted are bias voltage, tunneling current, loop gain, scan speed and area. Each image can be saved manually, or the software can save all images automatically. Data is saved as text files, which enables use of several different programs designed for editing and analyzing STM images.

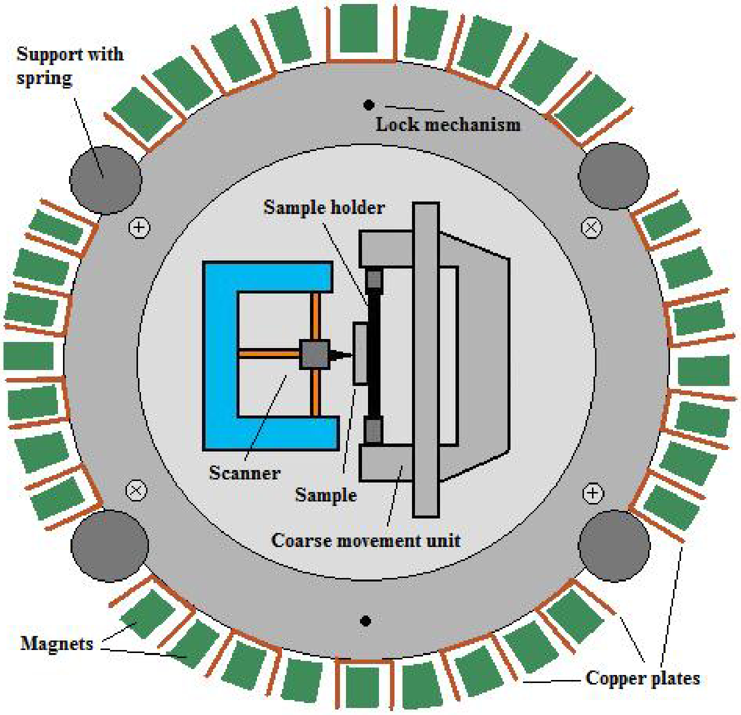

Figure 5.3: The STM viewed from above. Four springs allow the STM to hang freely while oscillations are dampened by the springs and by several magnets that induce a dampening Eddy current in copper plates attached to the STM. The three piezocrystals as well as the course movement unit can move the tip and sample in three dimensions [99].

5.6 MAX-lab

XPS experiments were performed at beamline I311 of the MAX II storage ring at MAX-lab in Lund, Sweden. The MAX II ring has a circumference of 90m, and consists of 10 straight sections separated by bending magnets [100]. It operates at an energy of 1.5GeV, and is thus characterized as a 3rd generation storage ring. The I311 beamline is undulator based, and can provide X- rays with energies between 43-1500eV which are sent through a monochromator. The experimental station consists of separate analyzer and preparation UHV chambers. Usual sample preparation instruments such as a sputtering gun and LEED optics are available in the preparation chamber, and a hemispherical electron energy analyzer is used in the analysis chamber.

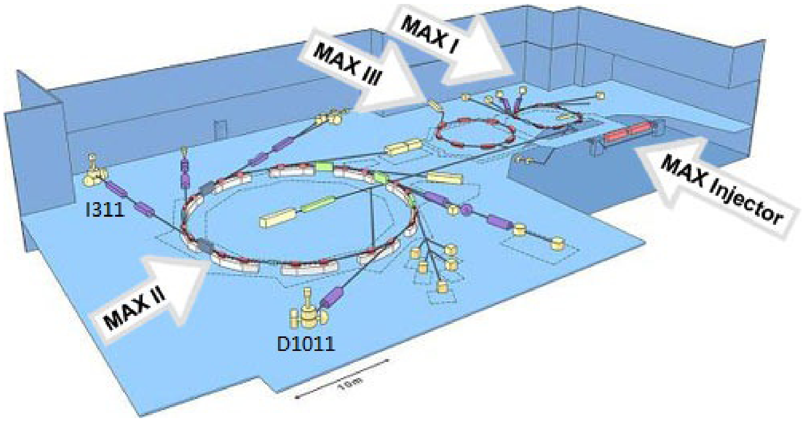

Figure 5.4: An illustration of MAX-lab [100]

6. Experimental procedure

This chapter gives an explanation of the experimental procedures applied in the work with this thesis. First, a simple description is given of which steps have been applied in a typical lab session. Then procedures for sample preparation and characterization are explained in more detail before a short description of data analysis and software is given. The last section describes the principle behind the tip manufacturing process. Note that procedures for XPS measurements are not presented, as the author did not take part in those experiments.

6.1 A typical lab session

Figure (6.1) shows the overall procedure applied in this work. Each lab session lasted most of the day, starting by cleaning the sample by cycles of sputtering and annealing. LEED was then used to determine whether the structure of the clean PdCu(100) was seen, and thus whether or not further sputtering was necessary. The clean surface could then be characterized by STM, or oxidized. LEED was again used after oxidation both for characterization and for checking that the surface had actually been oxidized. Before STM was performed, the turbo pump had to be switched off, and since it requires at least two hours to reach sufficiently low pressure again , no more sample preparation was performed during the rest of the lab session once STM imaging had started. One attempt was made to oxidize the clean surface while performing STM (in- situ STM). The Ar and O_2 gas was changed every Monday to make sure only clean gas was used in the experiments.

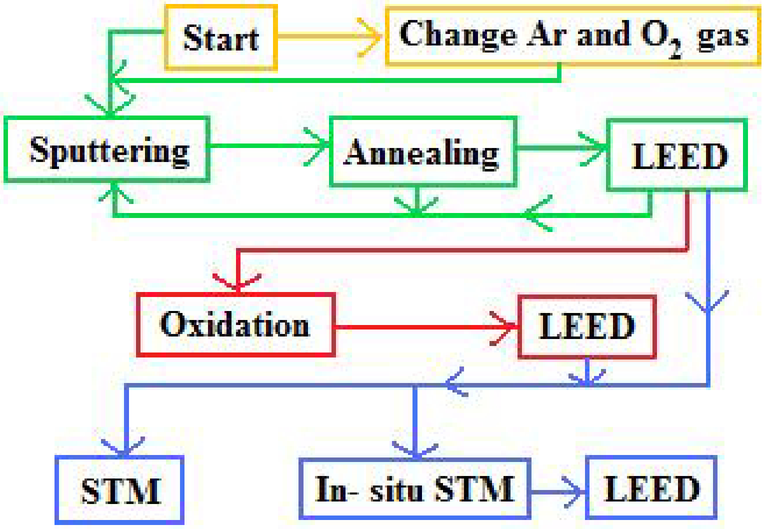

Figure 6.1: Flow diagram of the experimental procedure. Green boxes represent sample cleaning for obtaining a clean PdCu(100) surface, red represent oxidation and blue represent characterization.

6.2 Sample cleaning

The sample was always cleaned by cycles of sputtering and annealing. The number of sputterings varied from time to time, depending on the preparation history of the sample. After the chamber had been baked, around ten cycles were performed. At least two cycles were performed after oxidation. If the sample had not been oxidized in the preceding lab session, only one or two sputterings were usually performed. Argon was used for sputtering in all experiments. Table (6.1) summarizes the parameters used in all sputterings. Annealing was performed after every sputtering, and the sample was also heated during oxidation. Two temperatures were used: 300^{o}C and 600^{o}C. In the STM and LEED experiments, annealing time was always 10 minutes unless otherwise stated. XPS experiments were performed with varying annealing time at temperatures between 327^{o}C and 627^{o}C. Since the emissivity of the $Pd_{57}Cu_{43}$ alloy was not known, an emissivity of 0,14 was chosen in the pyrometer because it is intermediate between the emissivities of Pd and Cu individually.

Table 6.1: Parameters used for sputtering

Variable	Value
Time	30 minutes
Ion energy	1keV
Ar pressure in chamber	Between 2,0 $\cdot 10^{-5}$ and 4,0 $\cdot 10^{-5}$ mbar
Temperature	Room temperature

6.3 Oxidation

Oxidation was performed by heating the sample to 300^{o}C or 600^{o}C and letting oxygen gas flow into the chamber to obtain a constant oxygen pressure of up to $5{\cdot}10^{-5}$mbar. As a measure of oxygen exposure, the dose is given in Langmuirs (L). A dosage of 1L corresponds to exposing the surface to $1{,}33{\cdot}10^{-6}$mbar for one second. When in- situ STM was performed during oxidation, the ion pump was the only pump maintaining low pressure. Oxygen pressure was therefore never higher than $1{\cdot}10^{-8}$mbar in the in- situ experiment.

6.4 LEED

LEED was always used to check that the expected crystallographic structure was present in the surface after cleaning or oxidation. Images of the diffraction pattern were made every time, and for comparable and reproducible results, the same electron energy was used every time if possible. To look carefully for very weak diffraction spots, the electron energy was varied, usually towards lower energy, which results in fewer spots. After energy had been changed, the lenses were adjusted so the spots became as sharp and bright as possible. Whenever weak spots appeared, a new image was made. In this way, diffraction spots were detected which were otherwise invisible at the energies usually used after both sputtering and oxidation.

6.5 STM

The turbo pump was always off while performing STM to avoid vibrations. After annealing or oxidation, one always waited at least one hour to allow the sample to cool down and the chamber pressure to decrease. Oxidation had a very negative influence on the pressure, as it could take days for the pressure to return to its normal value if a high oxygen dosage had been used. Therefore pressure was usually around $2{\cdot}10^{-9}$mbar - $5{\cdot}10^{-9}$mbar while performing STM after oxidation. When the clean surface was studied, pressure was usually below $1{\cdot}10^{-9}$mbar. Only one wolfram tip was used in all STM experiments. All images were made with a resolution of 512x512 pixels in constant current mode. Both backward and forward scanning directions were recorded. Scan speed was usually four times the size of the image, i.e. an image of 100x100nm^2 was scanned at a speed of around 400nm/s.

Based on experience with this STM system, a strategy was worked out for how to achieve good resolution. First of all, imaging was heavily disturbed by noise until around 17:00, meaning there was no point in performing STM earlier than that. The first thing to look for when scanning was flat areas of around 200x200nm^2. Occasionally one could then run into something that would appear as very wide and high formations on the surface. It was then important to change area frequently until the whole area appeared flat, so that step edges, holes and islands were visible. If this proved impossible due to noise or large formations, the sample was retracted from the tip, and moved a fair distance sideways using the coarse movement unit, before re- approaching. That sometimes helped after one or more attempts, but if imaging was still bad, the sample was retracted and lifted out and back into the STM in an attempt to reposition the sample in a more stable position. These steps were repeated until flat areas could be located and imaged with good stability. It actually worked almost every time.

Once flat areas could be imaged, features such as islands, step edges, line defects and holes appeared very clearly. It would then be an appropriate time to try to go down to atomic scale. Pushing for atomic resolution is always tricky, and requires patience. One would typically start at 30x30nm^2. Noise depended strongly on loop gain, and could be reduced by setting loop gain to 2-3%. Low voltage (±0,1-0,3V) and high tunneling current (more than 2nA) proved to both reduce noise and improve resolution when scanning small areas, both on the clean as well as the oxidized surface. Scan area was then changed regularly, while small adjustments were made to voltage, tunneling current and loop gain until atomic resolution was obtained. On a very few occasions, none of these steps were useful. Attempts were then made to induce changes to the tip by setting voltage (up to 10V), tunneling current (up to 10nA) and scan speed (up to 10x scan area) to high values for a few minutes, hoping it would change into something better.

6.6 STM image analysis

Although the imaging software for the STM could also be used to analyze and edit the images, a free program called Gwyddion was used in this work, as it provides the user with more analyzing tools. Gwyddion is a program that is able to analyze images obtained by all scanning probe microscopy techniques [101]. In this work, it has been used to create images by importing raw data files, edit the images and obtain quantitative information from the data.

Images have been edited by applying four different functions in Gwyddion: level data by mean plane subtraction, correct lines by matching height median, correct horizontal lines and stretch color range to part of data. The first simply computes a plane from all image points and subtracts it from the data. The line correction functions match individual horizontal lines and points, and thus correct lines and scars appearing in the image that originate from the imaging instead of the sample surface. At last, the colour range can be edited in order to highlight certain features such as atoms, islands, defect lines etc. These functions make images clearer and smoother, and although they modify some of the data points, no important information is lost. Both interpretation and data processing of images is therefore easier after editing with these functions.

Line profiles have been used to extract quantitative data from STM images. A line profile shows the height distribution as a function of distance along a given line in the surface plane. Interatomic distances can be found by creating a line profile along a given row of several atoms. The atoms will then appear as maxima, and by placing cursors at the first and last atom in the profile, Gwyddion calculates the distance between those atoms. By division of the number of atoms in the profile, the interatomic distance is determined. The angle of the line profile relative to the horizontal axis in the STM image is also given, so that the directions of atomic structures can be compared amongst different images. Line profiles can also be used to fit step edges, holes and islands (see Figure (6.2). Gwyddion uses such fits to calculate their widths and heights.

6.7 XPS spectrum analysis

XPS spectra were plotted in a program called Igor [102], which can be used for processing of several kinds of data. The XPS spectra were loaded as text files and displayed graphically as intensity vs. binding energy curves. For most spectra, an additional measurement of the Fermi edge was also performed with the same photon energy as the measurement of the core levels. Since the Fermi edge always reveals at which binding energy the intensity goes to zero, this can be used to calibrate each spectrum so that all peaks are at their correct binding energies. The binding energy coordinate of

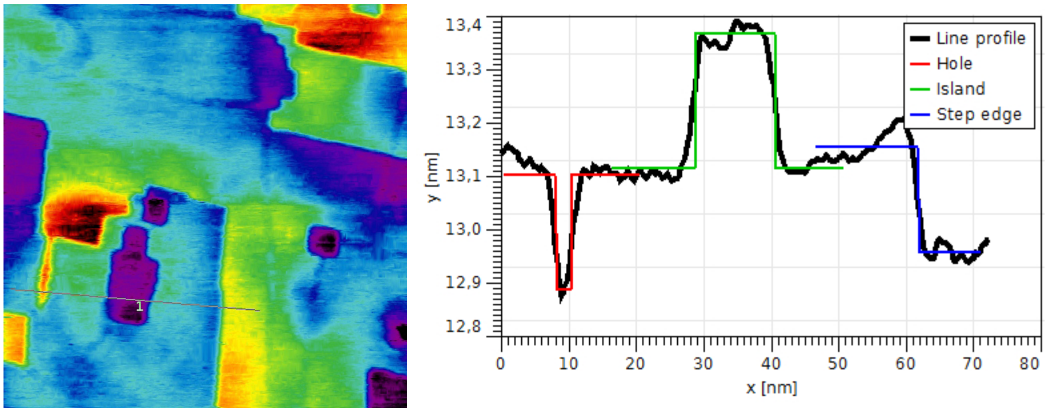

Figure 6.2: Left: An STM image with a line profile running over a hole, an island and a step edge. Right: The line profile with fits. Gwyddion uses fits to calculate widths and heights.

the Fermi edge was found by fitting a curve of the form:

$$f(x) = \frac{h}{1 + \exp(\frac{-(x-b)}{c})} + d \tag{6.1}$$

where b, c, d and h are constants that were given initial values. A curve fitting algorithm then found the value of b which was the binding energy of the Fermi edge. Figure (6.3) shows a typical Fermi edge that has been fitted. Once b was found, the corresponding core level spectrum could be shifted by b along the binding energy axis. Calibration was performed for all Pd3d and O1s spectra, but not for Cu2p spectra due to the difficulty of fitting the Fermi edge at the photon energies used for Cu2p spectra.

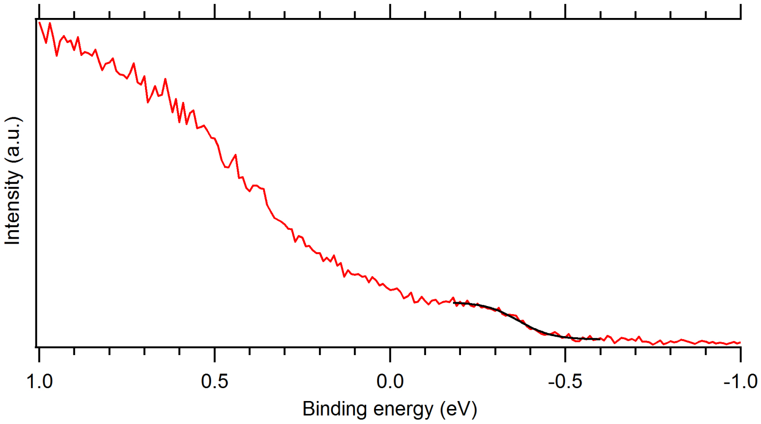

Figure 6.3: A Fermi edge with fit.

Once XPS spectra were calibrated, they could be compared by adding them to the same coordinate system and normalize them at low binding energy. Normalization in this case means to assign the spectrum a value of one at a single point, thus subtracting background to make it easier to compare the spectra. Since Cu2p spectra could not be calibrated, they were simply shifted in such a way that the peak appeared at the same binding energy for each spectrum. Their binding energies are therefore not correct, but it is still possible to compare their shapes and intensities.

Peaks were fitted in a program called FitXPS [103]. This program uses the line shape found by Doniach and Šunjić [104]:

$$I_\alpha(E) = I_0 \frac{\Gamma(1-\alpha)\gamma}{[(E-E_0)^2+\gamma^2]^{(1-\alpha)/2}} \cos\left[\frac{\pi\alpha}{2} + (1-\alpha)\tan^{-1}\left(\frac{E-E_0}{\gamma}\right)\right] \tag{6.2}$$

where I_0 is the intensity at E_0, Γ is the gamma function, α the asymmetry parameter and 2γ is the Lorentzian full width at half maximum. FitXPS computes a convolution between this line shape and a Gaussian line shape to obtain:

$$I(E) = \int_{-\infty}^{\infty} I_\alpha(E') I_G(E-E')\,\mathrm{d}E' \tag{6.3}$$

This way, each peak can be fitted to obtain peak position, area, maximum, asymmetry, width and other parameters useful for extracting information from XPS spectra. A fitted XPS spectrum is shown in Figure (6.4).

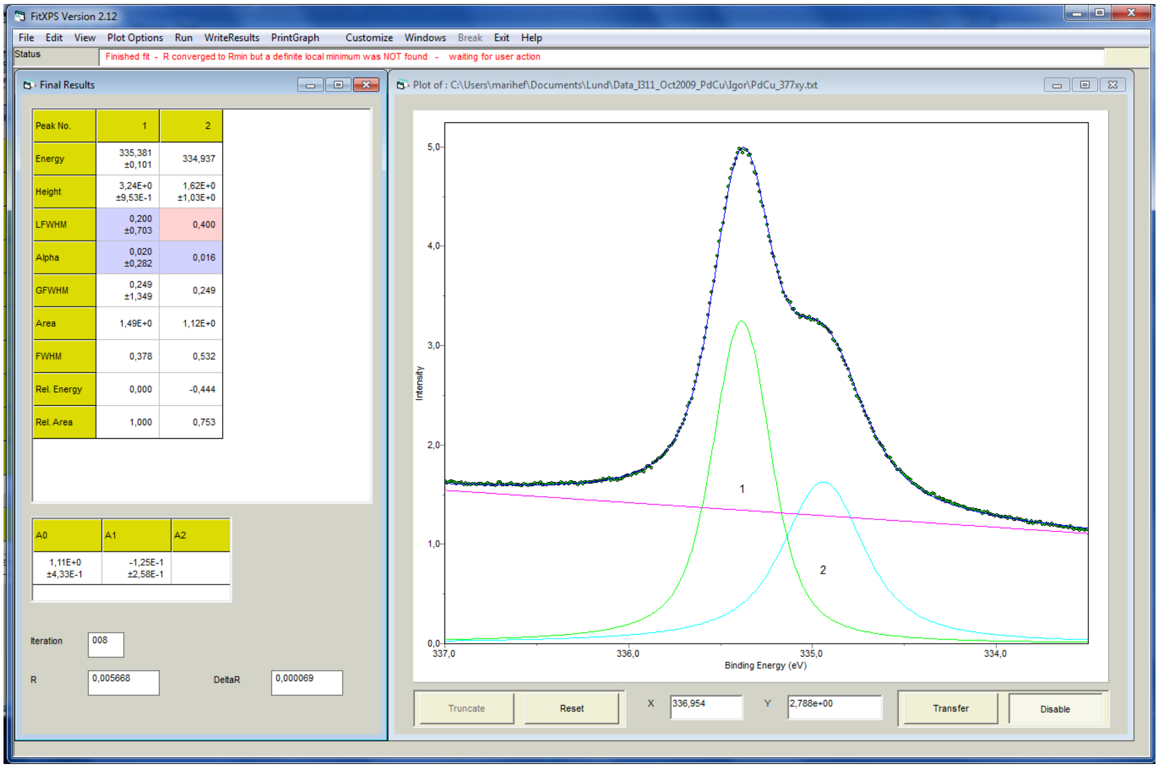

Status: Finished fit - R converged to Rmin but a definite local minimum was NOT found - waiting for user action

Peak No.	1	2
Energy	335,381 ±0,101	334,937
Height	3,24E+0 ±9,53E-1	1,62E+0 ±1,03E+0
LFWHM	0,200 ±0,703	0,400
Alpha	0,020 ±0,282	0,016
GFWHM	0,249 ±1,349	0,249
Area	1,49E+0	1,12E+0
FWHM	0,378	0,532
Rel. Energy	0,000	-0,444
Rel. Area	1,000	0,753

A0	A1	A2
1,11E+0 ±4,33E-1	-1,25E-1 ±2,58E-1	

Iteration: 008

R: 0,005668

DeltaR: 0,000069

X: 336,954

Y: 2,788e+00

Figure 6.4: Screen image of the FitXPS program showing a fitted spectrum and the different quantities it calculates.

6.8 Tip etching

The single wolfram tip used in this work was made by electrochemical etching. A wolfram wire was dipped into an etching solution, and a voltage was applied between the wire and solution so that a current would pass. The current was controlled by a program which shut it off as soon as the current dropped significantly, at which point a sharp tip was formed. The tip was then dipped into three separate glasses of distilled water to get rid of any remains of the etching solution. By looking at the tip through a microscope, one could determine whether or not it was good enough to be put into the vacuum chamber. To avoid too much oxidation of the tip, it was put into the load lock of the vacuum chamber as quickly as possible.

7. Results and discussion

All experimental results are presented and discussed in this chapter. The first section deals with the clean surface and the second section with oxidized surfaces. The following notation is used throughout this chapter: Oxygen dosage [L] O_2 @ Oxidation temperature / PdCu(100)_Annealing temperature for the clean sample. E.g. 3400L O_2 @ 600^{o}C / PdCu(100)_[600^{o}C] means that the oxygen dosage is 3400L, temperature during oxidation is 600^{o}C, and the clean surface was annealed to 600^{o}C prior to oxidation. Unless otherwise stated, annealing time is 5 minutes in XPS experiments and 10 minutes in LEED and STM experiments.

7.1 Clean surface

7.1.1 XPS spectra

XPS spectra were recorded for the clean surface after cycles of sputtering and annealing. Figure (7.1) shows fitted Pd3d$_{\frac{5}{2}}$ spectra after annealing to temperatures between 600K and 900K for 5 minutes. Each spectrum consist of two components. The component with lowest binding energy is clearly much smaller for 450eV photon energy than for 390eV, which is evidence for that component arising from Pd atoms in the surface since 390eV is a more surface sensitive photon energy than 450eV for the Pd 3d$_{\frac{5}{2}}$ core level. The two components are therefore one bulk and one surface contribution to these spectra. There is no doubt that the surface component decreases with increasing annealing temperature, and it is very small compared to the bulk component after annealing to 900K. This is due to segregation of copper to the surface, and indicates that the surface becomes more Cu rich the higher the annealing temperature, in agreement with previous results from studies of PdCu alloys [10, 48, 50, 51, 52]. In Figure (7.2) the ratio of the area under surface (A_{surf}) and bulk (A_{bulk}) components are plotted for each temperature and photon energy. At 600K and 390eV photon energy, the two components differ only by a factor of ~ 0.82, whereas at 900K, the surface component differs by ~ 0.26 from the bulk. This large difference may not be caused entirely by segregation of Cu from bulk to the topmost atomic layer. Miller et al. observed that the near- surface region of a $Pd_{70}Cu_{30}$ alloy became more Pd rich relative to bulk upon annealing to similar temperatures as in this thesis [10]. Such a phenomenon could also occur for this system, as it would be consistent with the data. A_{surf}/A_{bulk} appears to depend linearly on annealing temperature within these measurements. As expected, the ratio is smaller when a photon energy of 450eV is used due to the lower surface sensitivity. Note that the measurement point at 742K in Figure (7.2) is not consistent with the others, and is therefore probably an experimental error.

One can also see in Figure (7.1) that the whole spectra are shifted towards higher binding energy for higher annealing temperatures. Binding energies for bulk components are plotted against temperature in Figure (7.2). A binding energy shift of ~ 0.22eV is observed between 600K and 900K. It is

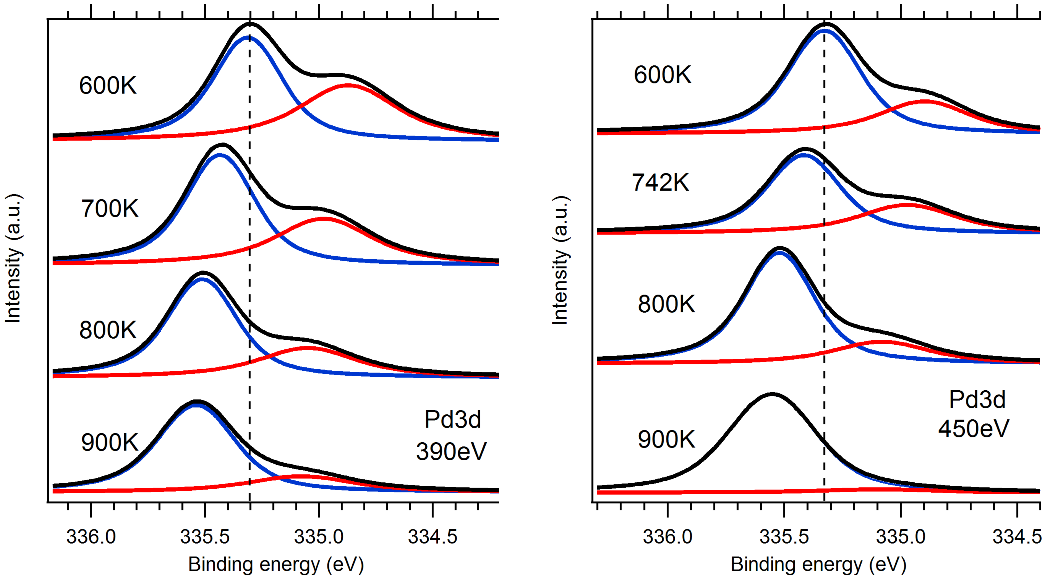

Figure 7.1: Fitted XPS spectra for the Pd 3d$_{\frac{5}{2}}$ core levels at 390eV and 450eV for different annealing temperatures. Spectra are shown in black, bulk components are blue and surface components are red. The dashed lines indicate the binding energy of the bulk component at 600K, and serve as guidelines.

not straightforward to explain the origin of this shift. Since Cu is known to segregate to the surface upon annealing, possibly leaving the near- surface region Pd rich, the alloy composition in the XPS accessible region obviously changes with temperature. Depending on the nature of Pd-Pd, Cu-Cu and Pd-Cu interactions, there may then be differences in strain, bonding or electrical propterties which could cause a core level shift. Order- disorder transitions at elevated temperatures of $\sim$ 700K have been observed for $Pd_{50}Cu_{50}(110)$ [51, 53] and also been suggested for polycrystalline $Pd_{70}Cu_{30}$ [10]. It was believed that although the surface composition did not change upon such transitions, the local atom arrangement was changed as small ordered areas rich in Pd or Cu were replaced by a random distribution of the two alloy components. Segregation of Cu to the initially Pd rich $Pd_{57}Cu_{43}(100)$ surface is compatible with such a transition given that the segregated Cu atoms are distributed randomly. This may explain the shift observed for both surface and bulk components in Figure (7.1).

Experiments have shown that Pd $3d_{\frac{3}{2}}$ spectra are shifted towards higher binding energy for higher Pd coverage when Pd is deposited onto Cu(100) [79], which is consistent with the results presented here with Pd $3d_{\frac{5}{2}}$ being shifted towards higher binding energy for more Cu rich surfaces. The shift is most likely due to the effects of segregation and distribution of alloy components on local strain, bonding and charge transfer. XPS spectra for Pd(100) show that the bulk component is located at 334.95eV (Figure (A.1)). Thus the core level shift (CLS) of Pd $3d_{\frac{5}{2}}$ is $\sim$ 0.37 for $Pd_{57}Cu_{43}(100)$ at 600K and $\sim$ 0.58 at 900K. These values are only slighly larger than the $\sim$ 0.3eV found experimentally by Mårtensson et al. [106] and theoretically by Olovsson et al. [105], with the difference probably being caused by different sample preparations. The surface core level shift (SCLS), which is the binding energy difference between surface and bulk components, is $\sim$ 0.450eV for the $Pd_{57}Cu_{43}$ system, which is very similar to the SCLS of 0.460eV for Pd(100).

Annealing time has a similar effect on CLS and surface to bulk ratio as annealing temperature. Longer annealing time causes a larger CLS as well as more Cu segregation at 600K, as shown in Figure (7.3). There are larger differences between 5 and 10 minutes annealing than between 10 and 15 minutes, which indicates that the mechanisms behind Cu segregation and Pd $3d_{\frac{5}{2}}$ binding energy shift approach an equilibrium with time. These results agree with those of Miller et al. for polycrystalline $Pd_{70}Cu_{30}$ [10]. They found that an equilibrium was reached after 30 minutes, and that only small changes were detectable in the 10-30 minute interval. The same tendency is present in Figure (7.2), where dependence of CLS and A_{surf}/A_{bulk} on annealing time are remarkably similar. Comparing these results to the temperature dependence in Figure (7.2), it seems that CLS dependence on both annealing time and temperature is logarithmic, whereas the A_{surf}/A_{bulk} ratio depends linearly on T and inversely exponential on t. These results mean that the choice of 10 minutues as standard annealing time for this material is valid, although longer annealing time could be chosen in order to guarantee that equilibrium is reached.

Spectra were also recorded for Cu 2p, but these were not calibrated, as explained in chapter 6, and therefore also not fitted. The spectra in Figure (A.2) are normalized at low binding energy and shifted along the binding energy axis to make comparison easier. Higher annealing temperature clearly results in a higher intensity for these spectra, as expected because of Cu segregation. After 15 minutes annealing the spectrum is broader than it is after annealing for 5 minutes, and the area under the 15 min. spectrum appears larger. This could suggest more Cu in the XPS accessible region and a more complex chemical environment for Cu atoms, but such conclusions cannot be safely made from this spectrum since detailed investigations have not been performed. Core level shifts for these Cu spectra are also not covered here since they are not calibrated.

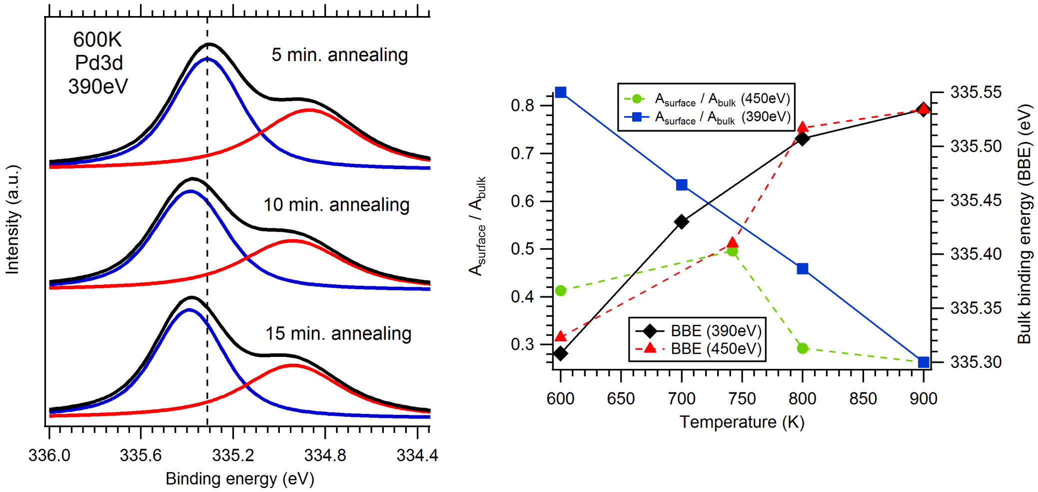

Figure 7.2: Left: Pd 3d$_{\frac{5}{2}}$ XPS spectra for the clean surface annealed to 600K with different annealing times. The dashed line indicates the binding energy of the bulk component at 600K, and serves as a guideline. Right: Plot of the ratio of area under the surface component to that of the bulk component and bulk binding energy vs. annealing temperature for the clean surface. Solid graphs are for photon energy 390eV while dashed graphs are for 450eV. The points at 742K are probably due to experimental errors, and can be neglected.

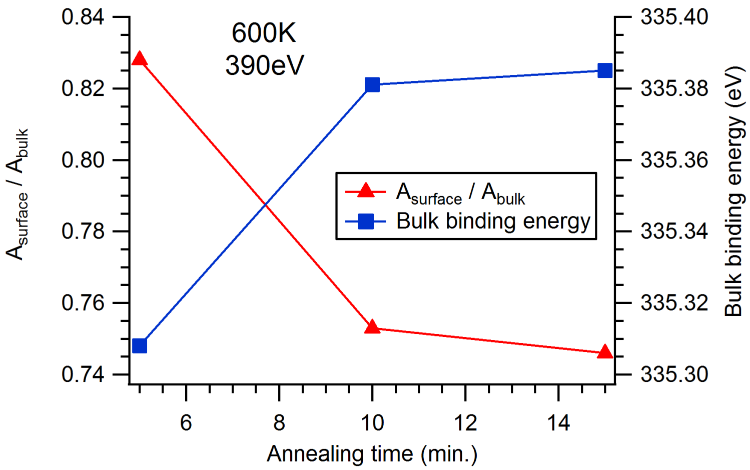

Figure 7.3: Plot of the ratio of area under the Pd 3d$_{\frac{5}{2}}$ surface component to that of the bulk component and bulk binding energy vs. annealing time for the clean surface. The graphs show that the system is close to equilibrium after 15 minutes, and that the difference is small between 5 and 10 minutes.

7.1.2 Clean surface annealed to 300^{o}C for 10 minutes

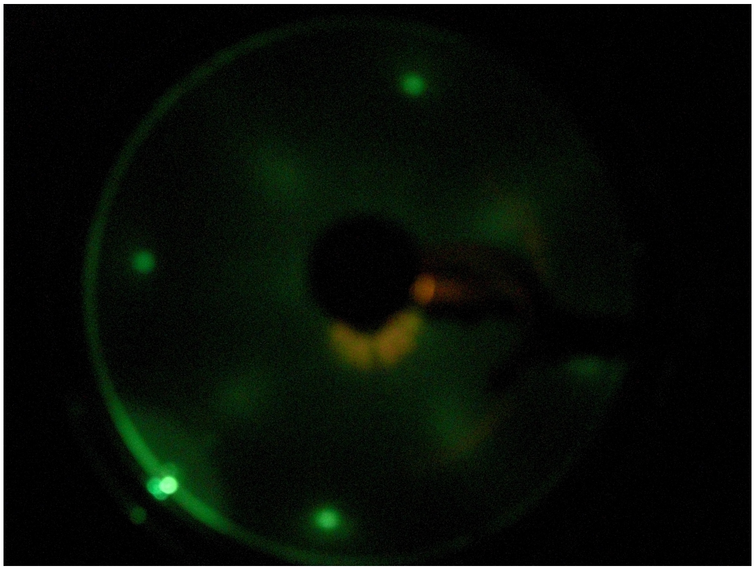

Figure 7.4: Image of the LEED pattern of the clean surface after annealing to 300^{o}C for 10 minutes, showing a diffuse c(2 × 2 pattern. Electron energy was 67.9eV.

A LEED image of the PdCu(100) surface annealed to 300^{o}C for 10 minutes is seen in Figure (7.4). The bright spots correspond to the (1 × 1) structure of the bulk, and were always seen very clearly on this surface. They constitute a square structure, as expected from an fcc(100) crystal. Quite interesting are the four weaker and more diffuse spots, which were also a part of all LEED images of the clean surface annealed to 300^{o}C. It was speculated that they could arise from oxide structures which had not disappeared after sputtering, but they appeared similarly regardless of the number of sputterings, and were there even after more than 5 cycles of sputtering and annealing. After the PdCu(100) sample was first introduced into the vacuum chamber, it was sputtered and annealed more than 15 times without being oxidized, but the diffuse spots did not disappear and they also never changed. The conclusion is therefore that they are a feature of the clean surface itself. Their positions are halfway between the (1 × 1) spots, and they constitute a square rotated 45^o relative to the square of the (1 × 1) spots. Hence a diffuse c(2 × 2) LEED pattern is seen. A plausible explanation of this is that the clean surface reconstructs, but it is difficult to explain why the half order spots are weak and diffuse based on qualitative LEED alone. Possible explanations are that the clean surface consists of both unreconstructed (1 × 1) and reconstructed c(2 × 2) domains, or that the c(2 × 2) structure is disordered or perhaps strained so that the positions of atoms differ slightly from an ideal c(2 × 2) structure. Similar LEED patterns were seen by Pope et al. for deposition of Pd on Cu(100), for which the (1 × 1) is replaced by a clear c(2 × 2) pattern up to 0.5ML coverage, but at higher Pd coverages, a weaker and diffuse c(2 × 2) LEED pattern was seen [79]. Using qualitative LEED spot analysis, Pope et al. concluded that the half order spots were diffuse due to a reconstruction with p4g symmetry, a so-called clock reconstruction as illustrated in Figure (3.6). Pd and Cu atoms are present at a ratio of 1:1 in this reconstruction [79, 84]. Such a

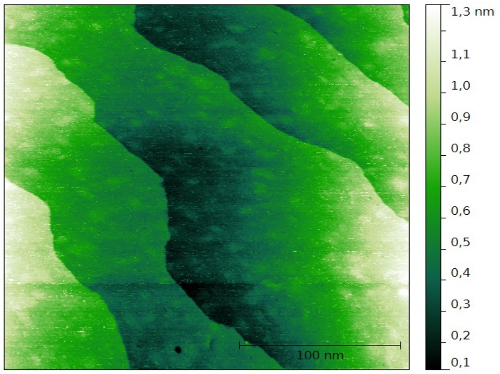

Figure 7.5: STM image of the clean surface annealed to 300^{o}C for 10 minutes (250x250nm^2, 1.42V, 1.14nA). Flat terraces are separated by step edges oriented in more or less the same direction.

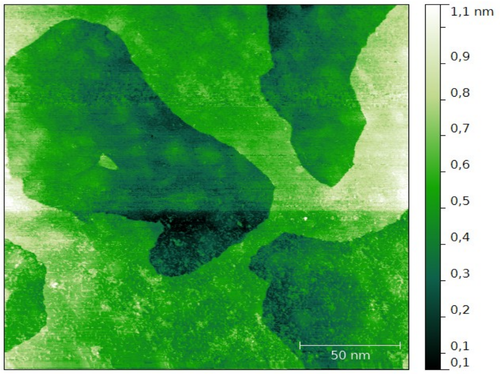

Figure 7.6: STM image of the clean surface annealed to 300^{o}C for 10 minutes (200x200nm^2, 1.67V, 2.10nA). Steps are oriented in any direction, and a large hole is seen in the image.
.

reconstruction could explain the diffuse LEED spots for the clean PdCu(100) surface annealed to 300^{o}C.

STM images of large areas of the clean surface display two different types of areas. Some areas consisted of flat terraces separated by step edges oriented in roughly the same direction, as in Figure (7.5), while in other areas step edges could be oriented in any direction and form large holes as in Figure (7.6). Both types of areas were present simultaneously, and sample preparation history did not appear to affect the amount of one area type versus the other. All step edges are 2-2.5Å high, meaning they are monoatomic steps. In addition to step edges, island- like formations roughly 10-15Å wide are seen which are less than 1Å high. Murray et al. observed Cu islands on the surface after deposition of Pd on Cu(100), but those island were much clearer than the formations seen here [80]. Thus these formations cannot be islands, but their occurrence on the surface is significant. In some lab sessions, a large number of screw dislocations are seen. Interestingly, there seems to be a correlation between the amounts of screw dislocations and island- like formations. Where there are many screw dislocations, there are less formations, or the formations appear differently. This may suggest that the formations are defects which sometimes appear as islands and sometimes as screw dislocations. The density of these defects is quite large for all sample preparations. The hole seen in the lower part of Figure (7.5) is $\sim$ 3.5Å deep. It is difficult to determine whether or not it is actually that deep or just imaged as being that deep.

At the atomic scale, two different atomic structures were seen for the clean surface annealed to 300^{o}C for 10 minutes. Figure (7.7) shows an area consisting of rows of atoms separated by a darker background. This result is in agreement with the study of surface alloy formation for Pd deposited on Cu(100) by Murray et al. [80]. The height difference between the bright atoms and the background is $\sim$ 0.2Å, whereas both the two large formations and the many dark holes are $\sim$ 1Å high and deep, respectively. This suggests that the image shows chemical contrast between Pd and Cu atoms, in which Pd atoms are imaged as being 0.2Å higher than Cu atoms, an apparent height difference

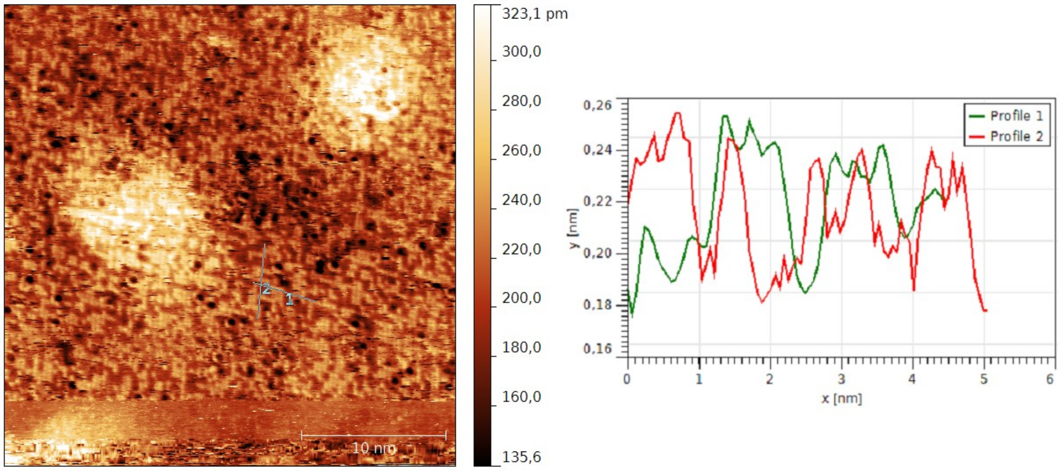

Figure 7.7: STM image of the clean surface annealed to 300^{o}C for 10 minutes ($31x31nm^2$, -1.37V, 5.25nA). Measured interatomic distances are 3.1-3.25Å, meaning that a c(2×2) structure is seen. The two bright areas are the island- like formations. Bright rows of atoms correspond to Pd, while the dark background is Cu atoms.

typical between atoms of different alloy components on a surface [108]. Even though individual Cu atoms are not seen in the image, line profile 1 shows two peaks at a lower height than the bright atoms, which probably represent Cu atoms. Interatomic distances are measured as being 3-3.25Å, and the structure is rotated 45^{o} with respect to the bulk (1×1) structure, hencea ac(2×2) structure is seen where rows of Pd atoms meet, in agreement with LEED results. Pd and Cu atoms appear to be present at a more or less 1:1 ratio in this surface. That explains why the surface component of the Pd $3d_{\frac{5}{2}}$ spectra is significant after annealing to 600K, yet a lot smaller than the surface component of pure Pd(100). The deep black holes in the image must be vacancies, and the large formations could consist of atoms ejected from these vacancy positions in the top layer which have diffused and nucleated at the formations. On the other hand, there are no sharp edges associated with the formations, but rather a gradual increase in height. They are also roughly half the height of monoatomic step edges. Hence the origin of the formations must be of complex character. The fact that rows of atoms are seen also in the formations serves as evidence that both Pd and Cu atoms are present there as well, so they cannot be pure Cu or Pd islands.

The other structure seen for this surface is shown in Figure (7.8). The surface is covered by a c(2×2) structure that appears slighly disordered. No chemical contrast is seen here, meaning that the rows of Pd atoms are most likely replaced by a more checkerboard- like alloy layer. The ratio of Pd and Cu atoms may be the same, only that this area has undergone an order- disorder transition, in which the previous separation of Pd and Cu atoms into small domains has disappeared, leaving a surface of higher entropy. This result agrees with previous studies of PdCu alloys [10, 51, 53]. The difference here is that this transition is seen at 600K, while it was previously seen at around 700K [51, 53]. Looking at the atomic structure in Figure (7.8), the c(2×2) is not oriented in two specific directions, but rather appears slightly rotated in different places. This image is not good enough to

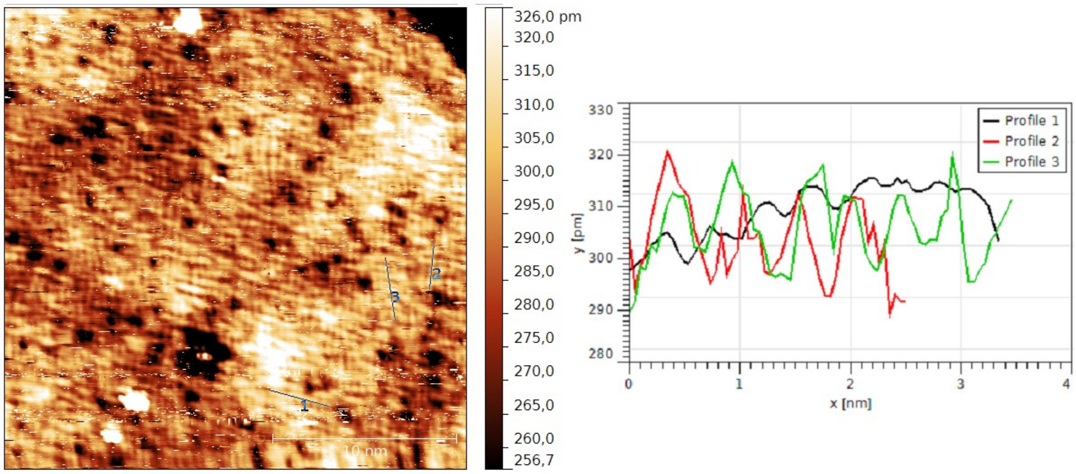

Figure 7.8: STM image of the clean surface annealed to 300^{o}C for 10 minutes (25x25nm^2, -0.41V, 2.85nA). A c(2 × 2) alloy layer with p4g symmetry is seen instead of domains of Pd and Cu atoms.

conclude that the p4g symmetry known to exist in PdCu surface alloys [79, 80, 84] is actually seen here, but it would certainly explain why there is a clear deviance from an ideal c(2 × 2) structure in STM images, and also why the half order LEED spots are diffuse. The surface is thus most likely clock- reconstructed and possesses a c(2 × 2) structure with p4g symmetry. Holes seen in Figure (7.8) are of the same depth as those seen in Figure (7.7), and are probably atom vacancies. The ordered surfaces with individual Pd and Cu rows or domains, and the more disordered surface with p4g symmetry were each seen in different lab sessions. The ordered surface was seen after 2 sputterings since the last oxidation, and the disordered was seen 3 sputterings after the ordered one. It is not known whether the number of sputterings has anything to do with which surface structure is seen, but the two different structures may depend on the preparation history of the sample.

7.1.3 Clean surface annealed to 300^{o}C for 30 minutes

In experiments with the clean surface, the highest resolution was obtained for a surface annealed to 300^{o}C for 30 minutes. Tiny areas of (1 × 1) structure were seen (Fig. (7.9), which were surrounded by large areas of c(2 × 2). Measured interatomic distances of the (1 × 1) depended on imaging conditions, and varied between 2.2-2.8Å, while they were 3.4-3.7Å for the c(2 × 2). Based on the XPS results presented, one expects small differences between this surface compared to a surface annealed for 10 minutes. LEED patterns appeared exactly the same as for 10 min. annealing, and are therefore not presented. This surface consisted of few step edges and large flat terraces, as well as areas of c(2 × 2)- p4g structure (See Figures (C)-(C)), and STM images did not differ much from those of the surface annealed for 10 minutes with that structure. This may indicate that the c(2 × 2)- p4g structure is preferred on surfaces annealed to 300^{o}C. For shorter annealing time, which we know from XPS does not allow the surface to reach equilibrium, areas of ordered Pd and Cu domains may still be present, while they become disordered upon longer annealing time. However, this only remains an assumption because atomic resolution on the clean surface was obtained quite

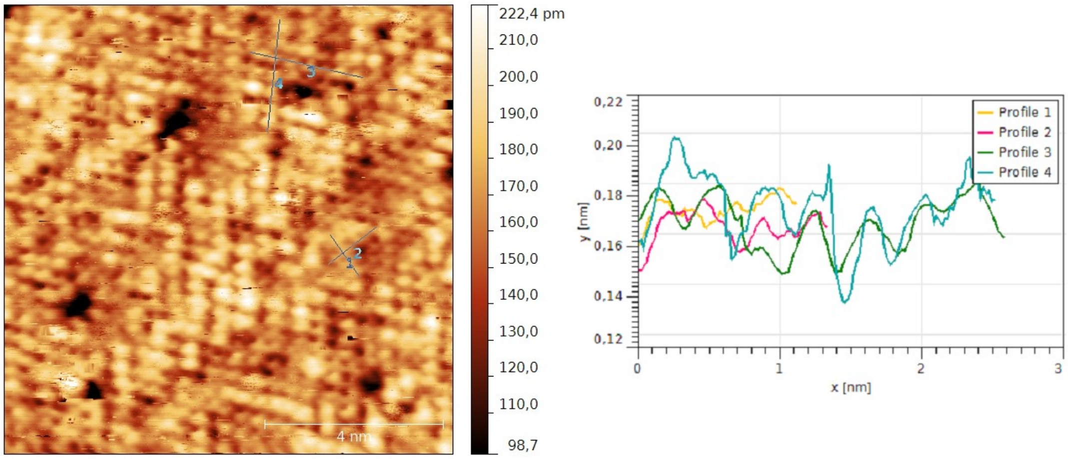

Figure 7.9: STM image of the clean surface annealed to 300^{o}C for 30 minutes (10x10nm^2, 0.02V, 8.54nA). The image shows a (1 × 1) structure partly covered by a c(2 × 2) reconstruction.

rarely so that only a few areas could be scanned with good enough resolution.

7.1.4 Clean surface annealed to 600^{o}C for 10 minutes

After annealing to 600^{o}C, the LEED pattern changes to a c(2 × 2) pattern in which the half order spots are just as bright and clear as those of the (1 × 1) bulk. This is seen in Figure (7.10). There also appears to be additional spots in between the half order spots, but those are very weak. This suggests a c(2 × 2) surface partly covered by a p(2 × 2) structure. Figure (7.11) shows an STM image of a large area of the surface. Flat terraces are separated by smooth step edges, and no screw dislocations or island- like formations are seen in any STM images. Higher annealing temperature clearly results in a more smooth surface with less defects. XPS revealed that Cu segregates to the surface at this temperature, while the surface component in Pd 3d$_{\frac{5}{2}}$ spectra is small compared to the bulk component. The absence of defects must therefore be a result of segregation and lateral diffusion processes at this temperature. An STM image with atomic resolution is shown in Figure (7.12). Measured interatomic distances are 4.5-5.25Å, and atoms are oriented in the same directions as the (1 × 1) of the bulk, hence this is definately a p(2 × 2) structure. The height of these atoms relative to the background is $\sim$ 1Å, thus the image shows an overlayer and not chemical contrast. A statistical approach was made to determine ratio of the area of p(2 × 2) atoms vs. that of the background. It turns out that the p(2 × 2) structure covers 11-17% of the surface, which is less than the saturation coverage of 25% for a p(2 × 2) overlayer. A p(2 × 2) alloy layer has previously been seen for deposition of Pd on Cu(100) [80]. The chemical composition of the overlayer seen here is difficult to determine. Cu is known to segregate to the surface, while Pd 3d$_{\frac{5}{2}}$ spectra still have a surface component. This overlayer is therefore probably an alloy layer, but further examinations are necessary in order to confirm that.

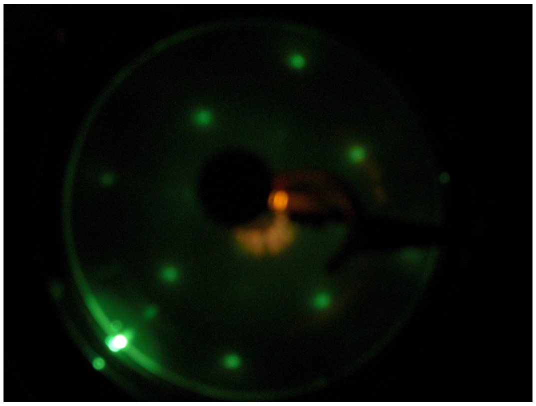

Figure 7.10: Image of the LEED pattern of the clean surface after annealing to 600^{o}C for 10 minutes, showing a weak p(2 × 2 pattern. Electron energy was 67.7eV.

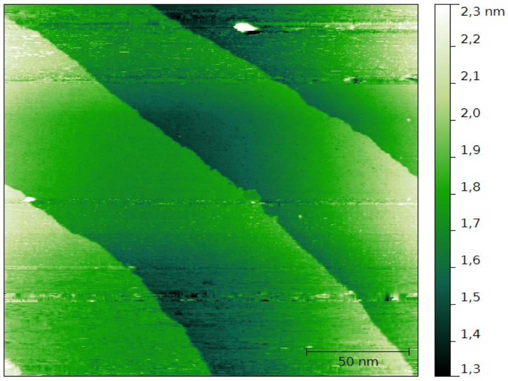

Figure 7.11: STM image of the clean surface annealed to 600^{o}C for 10 minutes (200x200nm^2, -0.34V, 2.38nA). Flat terraces are separated by step edges oriented in roughly the same direction.

7.2 Oxidized surface

7.2.1 XPS spectra

XPS spectra were recorded for different oxidations of $Pd_{57}Cu_{43}$(100). Figure (7.13) shows normalized Pd 3d$_{\frac{5}{2}}$ specra for the oxidized surface. The surface component present for the clean surface disappears upon oxidation. This means that the top layer consists of adsorbed oxygen or copper oxide instead of palladium atoms. Spectra recorded after oxidation with dosages of 500-45100L at 375-600K appear to be very similar both in width and intensity, the only exception being the one oxidized at 375K, which is wider than the others. This definately implies that no significant amount of PdO is formed, as the bulk Pd component remains unchanged upon oxidation. As for the clean surface, the shift of Pd 3d$_{\frac{5}{2}}$ towards higher binding energy after annealing the sample to higher temperatures prior to oxidation is seen also after oxidation. The shift between annealing at 600K and 900K is 0.25eV for the oxidized surface, which is the same as for the clean surface. In Figure (7.13), a spectrum recorded for the clean surface after annealing to 600K is shown for comparison. The bulk component of that spectrum is located at 335.31eV, whereas it is $\sim$ 335.15eV for the oxidized surface annealed to the same temperature. This shift of $\sim$ -0.16eV may reveal that the chemical environment for Pd atoms in the top layers change upon oxidation, possibly because of Cu segregation as a result of oxidation. Oxidation at temperatures around 600K also means that the sample is kept at that temperature for a longer time, which is found to increase the binding energy (Figure(7.2)). That would explain why the 45100L spectrum is at highest binding energy of the 5 spectra recorded for surfaces annealed to 600K, since that oxidation took longer. The 500L oxidation was performed on a clean surface annealed for 15 minutes at 600K vs. 5 minutes at 600K for the 45100L oxidation, which explains why those two are at almost exactly the same binding energy while the 3 others for a clean surface annealed to 600K are at lower binding energy. Oxidation of Pd(100) has shown 3 peaks with 4 components for Pd 3d$_{\frac{5}{2}}$ after formation of the $(\sqrt{5} \times \sqrt{5})$R27^o structure [58]. Since only one peak is seen here, the $(\sqrt{5} \times \sqrt{5})$R27^o structure is not expected to be present

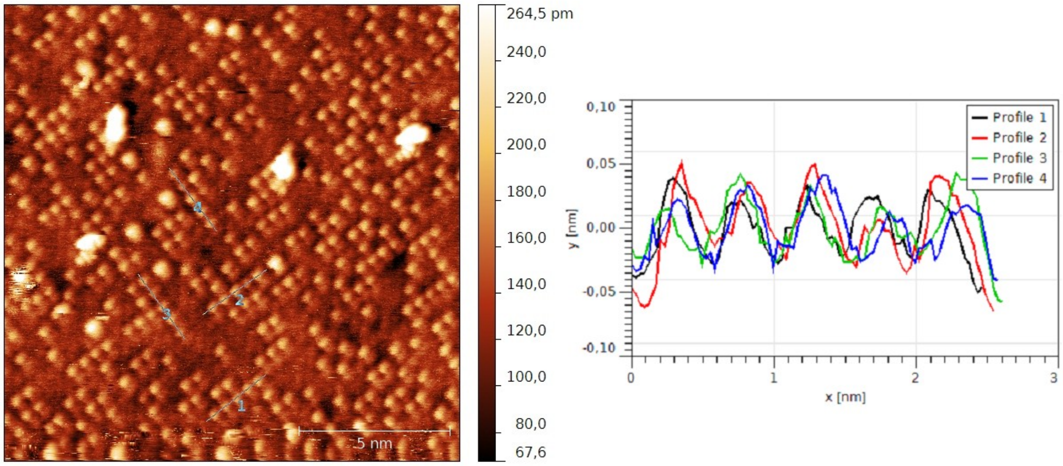

Figure 7.12: STM image of the clean surface annealed to 600^{o}C for 10 minutes (15x15nm^2, -0.24V, 3.09nA). Measured interatomic distances are 4.5-5.25Å in the same directions as that of the bulk (1 × 1). Hence a p(2 × 2) structure is seen in the image. The very bright cluster- like shapes could be small clusters of atoms or simply the restult of tip effects.

on the oxidized PdCu(100) surface.

Pd 3d$_{\frac{5}{2}}$ spectra for 45100L at 600K and 500L at 575K on clean surface annealed to 600K were fitted (Figure (7.13)). The 500L spectrum could be fitted with just one component, but the 45100L needed two. The second component in the 45100L spectrum is located at 334.77eV binding energy, which is 0.40eV lower than the bulk component. The origin of the second component is unknown, but it may have arised from the fitting procedure itself. Further studies are necessary in order to determine whether or not a second component is present in that spectrum.

Figure (7.14) shows Cu 2p spectra recorded after the different oxidations. The only visible change relative to the clean surface is that the peaks are wider. No clear evidence is seen for formation of Cu oxide at these temperatures. Cu 2p intensity is higher for surfaces annealed to higher temperatures prior to oxidation, which is a result of Cu segregation to the surface. Because no apparent chemical or surface core level shifts are seen in the Cu 2p spectra, it is very difficult to draw any conclusions from them, especially since they cannot be calibrated.

Perhaps most interesting for the oxidized surface are the O 1s spectra. These are shown for various sample preparations in Figure (7.14). Spectra recorded for 45100L oxidations have been separated from the others to make comparison easier. The large peaks represent O 1s while the smaller peaks are represented by Pd 3p levels. Fermi edges were not available for the top 3 spectra, so those are not calibrated, and therefore only shown for comparison of shapes and intensities. As for Pd 3d and Cu 2p spectra, the O 1s spectra are very similar for all oxidations. They show almost no dependence on oxygen dosage, a result which most likely means that at around 600K the surface is saturated with oxygen even at 500L. O 1s spectra also seem to consist of only one peak. These results then

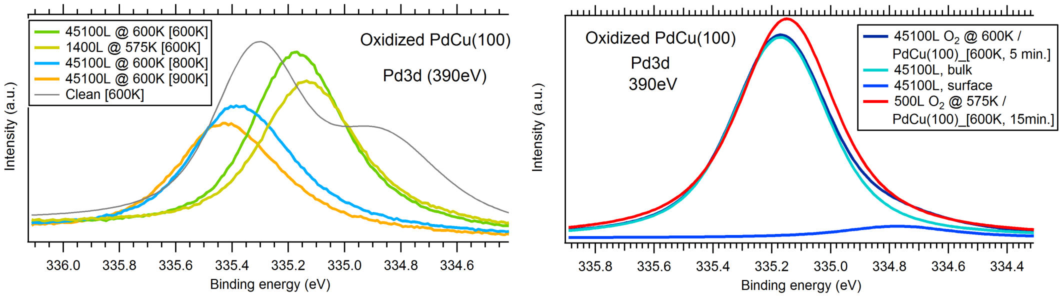

Figure 7.13: Left: Pd 3d$_{\frac{5}{2}}$ XPS spectra after different oxidations. The corresponding spectrum for the clean surface annealed to 600K is shown for comparison. Right: Fittings for two of the spectra. The one for 500L O_2 (red) could be fitted with one peak, while the one for 45100L O_2 needed two (blue).

suggest that no bulk oxide is formed in any of these cases. The layer of adsorbed oxygen is therefore non-reactive towards further oxidation at 600K even for oxygen pressures up to $5 \cdot 10^{-5}$mbar, which was the highest O_2 pressure used in the XPS experiments. O 1s spectra recorded for oxidized Pd(100) also consist of only one peak for $p(2 \times 2)$, $c(2 \times 2)$ and (5×5) oxide phases present at low coverages, and an additional peak is only seen upon formation of the $(\sqrt{5} \times \sqrt{5})R27^o$ phase [58]. The position of the O 1s peak is $\sim$ 530eV, which is in agreement both with oxygen on Pd(100) [58] and on Cu(100) [107]. Hence these oxygen spectra are quite similar to those reported in the literature for low- coverage oxide phases on Pd(100) and Cu(100), further indicating that no bulk oxide is formed, but rather just a layer of adsorbed oxygen. The only spectrum that differs from the other ones here is the one recorded after oxidation at 375K as opposed to 575K and 600K for the other spectra. Its maximum point is shifted $\sim$ 0.30eV from the others, and this is clearly caused by the lower oxidation temperature.

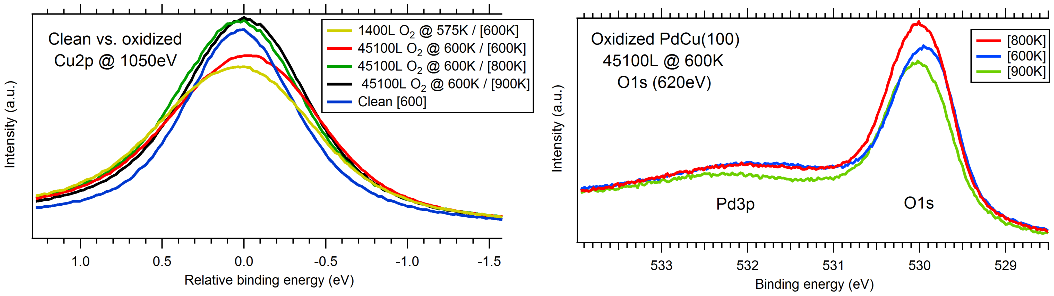

Figure 7.14: Left: Cu 2p spectra after different oxidations, compared with the spectrum of the clean surface annealed to 600K, which is more narrow than the oxidized ones. Right: O 1s spectra for 45100L O_2 at 600K on clean surfaces annealed to different temperatures. The small peak corresponds to Pd 3p levels, while O 1s levels contribute with a large peak.

7.2.2 Oxidation at 300^{o}C on surface annealed to 300^{o}C

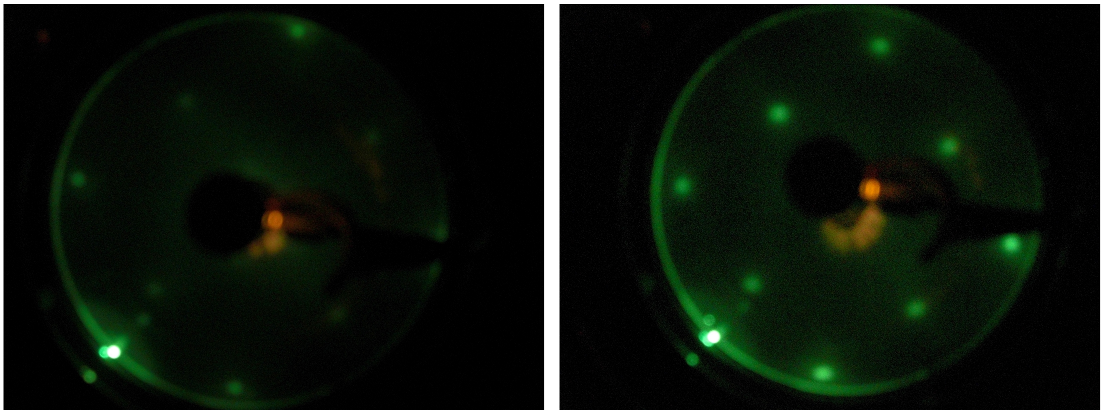

Figure 7.15: LEED images of the surface after oxidation at 300^{o}C of the clean sample annealed to 300^{o}C. Left: 1L O_2 with 49.9eV electron energy, showing a weak c(2 × 2) pattern. Right: 68L O_2 with 60.0eV electron energy, showing a clear c(2 × 2) pattern.

Figure (7.15) shows two LEED images of the surface oxidized at 300^{o}C with different dosages. The left image is the result after 1L O_2 and the right is taken after 68L O_2. Already after exposure to 1L oxygen, the LEED pattern changes from the diffuse c(2 × 2) of the clean surface to a more clear c(2 × 2) for the oxidized surface. At this low dosage, the half order spots are weak, but not diffuse. With increasing dosage, these spots become brighter, and at 68L they are just as bright as those of the substrate. LEED images for 338L, 1350L, 3400L and 33800L O_2 look exactly like the image for 68L in Figure (7.15), hence LEED results show that there is very little variation in surface structure with different dosages at these temperatures, and that the c(2 × 2) structure is found for all dosages.

Exposure to 1L oxygen results in a surface with rough terraces that appear to be partly covered by an overlayer (Figure (C.2). Island- like formations known to be present on the clean surface after annealing to 300^{o}C are still visible at 1L oxygen. The surface is rough due to patches of what seems to be an ordered structure covering the terraces. Atomic resolution images show that c(2 × 2) and p(2 × 2) phases coexist, while the overlayer was difficult to image due to the roughness (Figure (C.3). A large scale STM image of the oxidized surface with 10L oxygen dosage is shown in Figure (7.16). An incomplete overlayer is seen, which appears to have formed small clusters. A larger cluster is seen in the top right part of the image. This cluster is nearly 2Å high, the same height as step edges, suggesting it might be the beginning of an oxide island. Island- like formations on the clean surface were only around 1Å at their highest, and a sharp edge was not seen in any of them. On this cluster, however, there is a well- defined edge. In the middle of the cluster, there is an area that is 1Å lower than the rest of the cluster, but still 1Å higher than the surrounding background. This may be an oxide island that started to form from a formation that was there when the surface was clean, or it may have formed in a previously flat area as a result of the oxidation alone. A large number of smaller clusters are seen, and some places they have formed lines that almost cross a whole terrace. Notice that a slight ordering of step edges has taken place during oxidation. On the

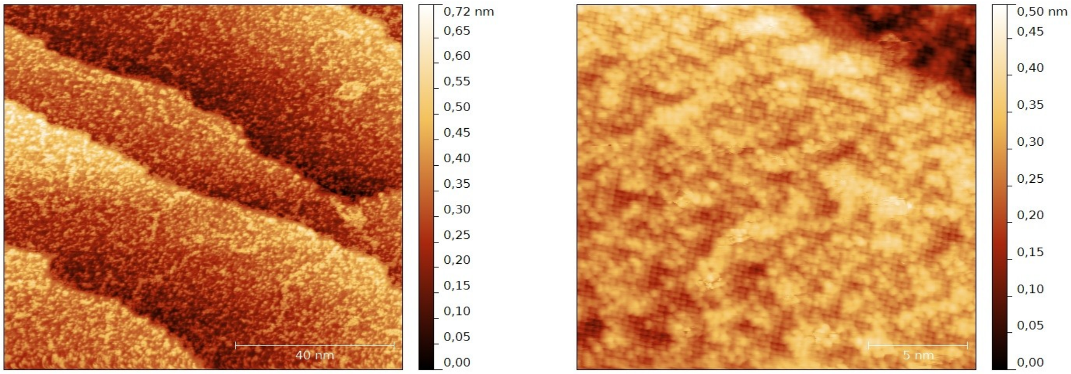

Figure 7.16: Left: STM image of 10L O_2 at 300^{o}C on the clean surface annealed to 300^{o}C (100x100nm^2, -0.857V, 1.40nA). The surface is partly covered by an overlayer, and appears rough. Ordering of step edges along [010] and [001] directions has taken place. The image shows what might be initial stage of an oxide island being formed. Right: Atomic resolution STM image of 10L O_2 at 300^{o}C on the clean surface annealed to 300^{o}C (20x20nm^2, 0.32V, 2.11nA). A p(2×2) is seen on top of a c(2×2) structure

clean surface, step edges can be oriented in any direction and appear smooth, but in Figure (7.16) one can see the initial stages of step edges being oriented in specific directions. An atomic resolution image of the surface exposed to 10L oxygen is also shown in Figure (7.2.2). A p(2×2) structure is seen on top of a c(2×2), and it is the p(2×2) that appears as clusters in the large- scale STM image. What is seen could be chemisorbed oxygen on top of a reconstructed c(2×2) PdCu alloy layer. However, the clusters are found to cover 35-40% of the surface, which is above the saturation coverage of a p(2×2), and the clusters look somewhat disordered. Therefore, this is probably the initial stage of a transition from p(2×2) to c(2×2), similar to what is known to occur for oxygen adsorption on Pd(100) [56, 57].

Increasing the oxygen dosage to 68L causes all steps to be oriented along the [010] and [001] directions of the bulk crystal, as shown in Figure (7.17a). Thus it takes a very low dosage to make steps fully ordered. The same phenomenon is observed for oxidation of Pd(100) [62] and Cu(100) [63]. Incorporation of oxygen in sub- surface sites eject Pd [57] and Cu [63, 68] atoms onto the terraces, which nucleate either at step edges or form islands on the terraces. Because of the similarities of Cu(100) and Pd(100) surfaces with the PdCu(100) surface, a similar mechanism must be the cause of island formation and step ordering also on this surface. The surface structure after 68L exposure is c(2×2), and a large number of what appears to be atom vacancies are seen (Figure (C.4)). Figure (7.17b) shows on oxidized surface after 1350L oxygen exposure. All steps are oriented in the preferential directions and several islands have formed. Islands are 2.0-2.5Å high, thus the same height as step edges both on the clean and oxidized surface. Screw dislocations similar to those of the clean surface are seen also after high oxygen exposures, and they also follow the [010] and [001] directions. Notice that the island at the bottom of this image is located right next to a screw dislocation. The bright lines seen on otherwise flat terraces are phase boundaries separating two domains of the c(2×2) structure. The apparent height of boundary lines is ~ 0.6Å, and they were

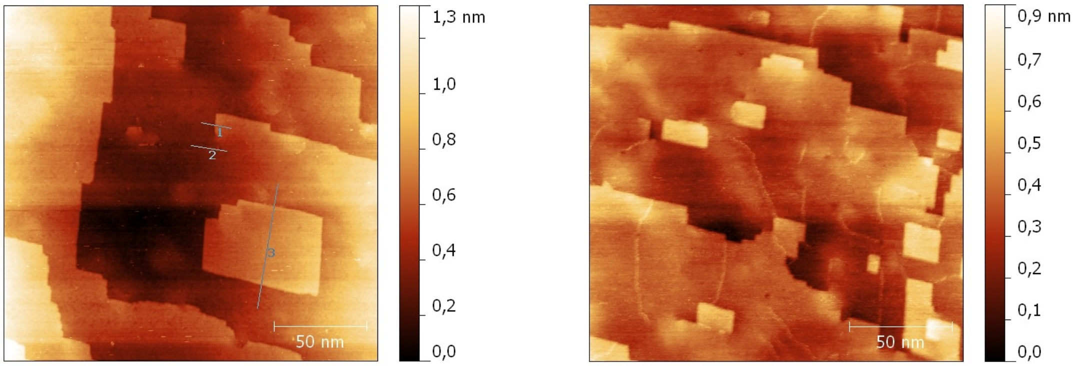

a) b)

Figure 7.17: a) STM image of 68L O_2 at 300^oC on the clean surface annealed to 300^oC (200x200nm^2, 1.24V, 1.40nA). Step edges and islands are oriented in the preferred directions. The image shows that screw dislocations are present also on the oxidized surface. b) STM image of 1350L O_2 at 300^oC on the clean surface annealed to 300^oC (180x180nm^2, 0.14V, 1.52nA). Several islands have formed with this oxygen dosage.

usually imaged as being higher than the background for both negative and positive bias voltages, although they occasionally appeared lower. In Figure (7.17b) as well as in several other STM images of this surface (E.g. Figure (C.5), there is evidence for boundary lines originating preferentially at corners of islands and holes, and at step edge kinks. Hence there is a connection between boundary lines and the formation of ordered steps. Boundary lines can cross islands, which indicates that the atomic structure of islands is also c(2 × 2).

Oxidation with 3400L O_2 was performed in two different lab sessions, with different results. In both cases, the surface was covered by the c(2 × 2) structure, but islands were only seen in one of the experiments even though the sample preparation after sputtering was the same (See Figure (C.6)). The only possible explanation for this is that the preparation history of the sample plays an important role. Islands were seen when the sample had previously only been annealed to 300^oC, while no islands were seen when the sample had been annealed to 600^oC in the previous lab session. Thus the segregation of Cu to the surface and the shift of Pd $3d_{\frac{5}{2}}$ towards higher binding energy observed by XPS upon annealing to 900K must influence the surface and near- surface region to such a degree that more than 2-3 sputterings are required to restore the original nature of this region of the sample. This may be a result of the order-disorder transitions observed for PdCu alloys, which is temperature- dependent [10, 51, 53] and may also be the cause of the Pd $3d_{\frac{5}{2}}$ CLS. An atomic resolution image of the surface after oxidation with 33800L is shown in Figure (7.18). Even with this high dosage and an oxygen pressure of $5{\cdot}10^{-5}$mbar, only the c(2 × 2) structure is seen. Obviously, this oxide structure is very inert towards further growth or reconstruction at 300^oC and typical oxygen pressures of experiments in UHV. The boundary line furthest to the left in Figure (7.18) originates at the corner of an edge and ends at the corner of another edge. It seems to consist of a complex atomic structure next to a bright row of atoms forming a zig-zag pattern, similar to the illustration in Figure (2.4). The inertness of the c(2 × 2) structure is consistent with XPS spectra showing no significant differences for different oxygen dosages at 600K. The only exception is the small second component needed to fit the XPS spectrum recorded for 45100L at 600K, but that component may be a result of the fitting procedure itself, as it is very difficult to explain its origin based on a relative temperature difference of only 27 degrees.

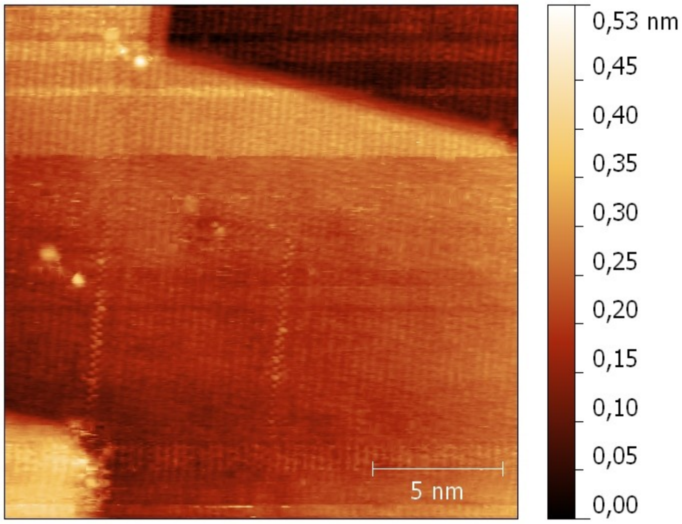

Figure 7.18: STM image of 33800L O_2 at 300^{o}C on the clean surface annealed to 300^{o}C (20x20nm^2, -0.15V, 2.63nA). The image shows the atomic structure of the boundary lines. Note that the line originates at the corner of one step edge and ends at the corner of another step edge. The surface is entirely covered by a c(2 × 2) structure.

7.2.3 Oxidation at 300^{o}C on surface annealed to 600^{o}C

An image of the LEED pattern for 10L O_2 at 300^{o}C on the clean surface annealed to 600^{o}C is seen in Figure (7.19a). A clear p(2 × 2) diffraction pattern was observed, i.e. the same as for the clean surface annealed to 600^{o}C. Figure (7.19b) shows an STM image of the surface after 1L O_2 exposure. In the bottom part of the image one can see that the c(2 × 2) structure forms an incomplete layer, and that the surface is rough and therefore difficult to image. A few small areas of a larger structure were found next to step edges. Although this area seemed to be disordered and at the same time difficult to image (Figure (C.7)), patches of ordered atomic structures were seen. In parts of this area, the structure looked hexagonal, while it looked more square in other parts. The only structure previously seen on Pd(100) and Cu(100) that could explain the one seen in Figures (7.19b and C.7) is the $(\sqrt{5} \times \sqrt{5})$R27^o structure seen on Pd(100) [57, 6, 58]. However, since one knows from XPS that this surface was Cu rich before oxidation, and given the very low oxygen dose, it would be very surprising if this is actually the $(\sqrt{5} \times \sqrt{5})$R27^o palladium oxide phase. It might be a structure only

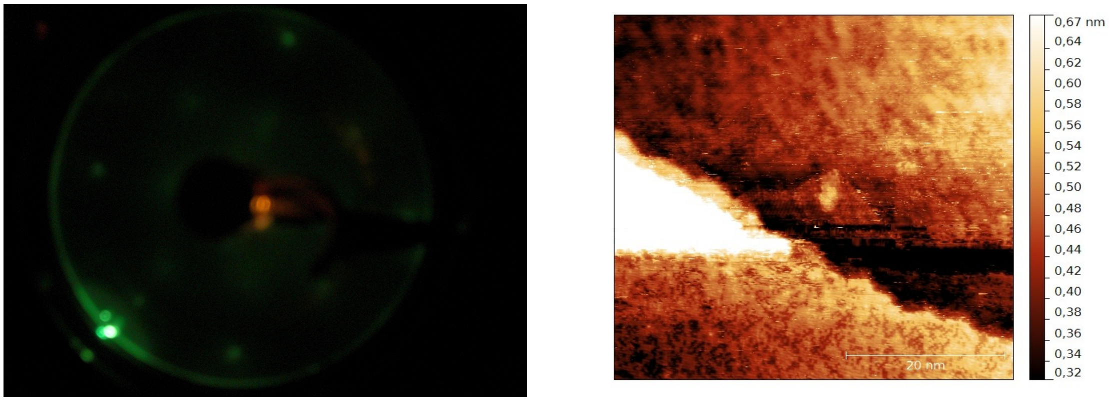

a) b)

Figure 7.19: a) LEED image of 10L O_2 at 300^{o}C on the clean surface annealed to 600^{o}C with 63.3eV electron energy, showing a p(2 × 2) pattern. b) STM image of 1L O_2 at 300^{o}C on the clean surface annealed to 600^{o}C (50x50nm^2, 2.80V, 3.02nA). The surface consists of an incomplete layer of c(2 × 2) structure. An area of a larger structure is seen in the middle of the image.

seen on the alloy surface, and not on Pd(100) or Cu(100). The area is surrounded by a step edge on one side and edges of very clear p(2 × 2) structure on the other side, while the rest of the terraces are covered by the c(2 × 2). For 10L O_2 exposure, the surface clearly consists of a p(2 × 2) on top of a c(2 × 2) (Figure (C.8)), explaining the p(2 × 2) LEED pattern in Figure (7.19a). There are no obvious tendencies towards preferential orientation of step edges after 10L O_2 exposure.

After exposure to 3400L O_2 at 300^{o}C on the clean surface annealed to 600^{o}C, the LEED pattern is a bright and clear c(2 × 2), with no signs of additional diffraction spots (Figure (B.1)). STM images of this surface are seen in Figures (7.2.3a and 7.2.3b). On a large scale, flat terraces are separated by step edges mostly oriented in the [010] and [001] directions. A small number of islands have formed, which follow the same directions. Based on this and the LEED pattern, most of the surface must be covered by a c(2 × 2) structures. But areas of a larger structure can also be found (see Figure 7.2.3b). This structure has two domains that are orthogonal to eachother, and follow the [011] and $[01\bar{1}]$ directions of the bulk crystal. It looks very much like the $(2\sqrt{2} \times \sqrt{2})R45^o$ oxide structure seen on Cu(100) [63], which is consistent with this surface being Cu rich prior to oxidation. Figure (7.21) shows the atomic structure in more detail. From this image it is not obvious that the structure is a $(2\sqrt{2} \times \sqrt{2})R45^o$ missing row type. The dark row parallel to line profile 3 appears to be a row of missing Cu atoms, in agreement with the interatomic distances along line profile 3 being ∼ 4.35Å, i.e. in between the measures distances of the c(2 × 2) (∼ 3.5Å) and p(2 × 2) (∼ 5.0Å). Measured interatomic distances along profiles 1 and 2 are 5.25Å and 6.94Å, respectively. However, in profile 1 there appears to be atoms that are imaged as being lower than the other ones, whereas this is not the case in line profile 2. This suggests that missing rows are also seen in between the bright atoms, and that one of the domains is imaged differently from the other. There is a convincing similarity between the image in Figure (7.21) and the model for the $(2\sqrt{2} \times \sqrt{2})R45^o$ structure in Figure (3.4). Hence the surface is covered mostly by a c(2 × 2) structure, but also shows areas of the missing row

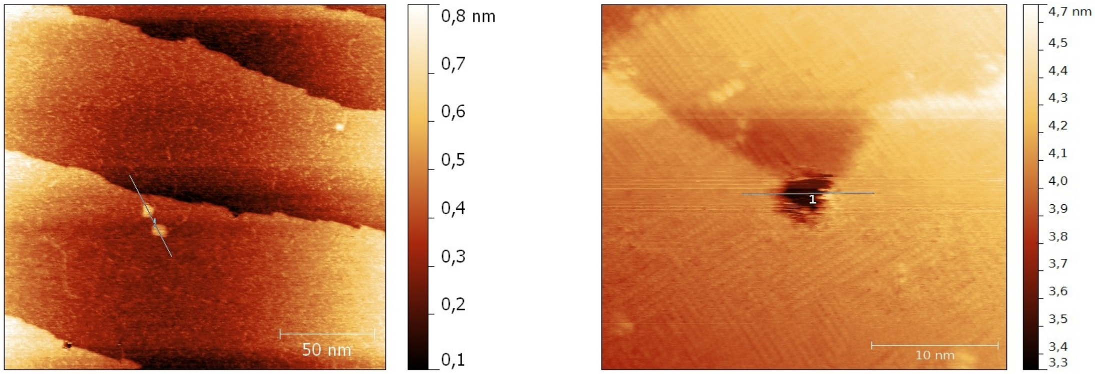

a) b)

Figure 7.20: a) STM image of 3400L O_2 at 300^oC on the clean surface annealed to 600^oC (200x200nm^2, -0.22V, 2.74nA). Large flat terraces are separated by step edges which are partly ordered in the [010] and [001] directions. Three small oxide islands are present. b) STM image of 3400L O_2 at 300^oC on the clean surface annealed to 600^oC (32x32nm^2, -0.36V, 2.33nA). A large structure with two domains which are orthogonal to eachother covers the whole surface in this image. The hole in the middle is $\sim$ 5Å deep.

reconstruction.

7.2.4 Oxidation at 600^{o}C on surface annealed to 600^{o}C

When the sample is oxidized with 3400L O_2 at 600^oC after annealing to 600^oC, LEED shows a very weak (4×4) pattern as in Figure (7.22a). Spots corresponding to $c(2 \times 2)$ is brighter than those of a $p(2 \times 2)$, which in turn are brighter than those of a (4×4). The 200x200nm^2 STM image in Figure (7.22b) shows that the surface appears disordered, although a small ordered area is visible in the bottom left part of the image. Several different structures are seen on this surface. In Figure (7.23)a), there are areas with a maze- like structure similar to what is seen for oxidation of Cu(100) [63]. The bright lines in those areas are less than 1Å high, and are therefore most likely boundary lines between the two domains of the $(2\sqrt{2} \times \sqrt{2})R45^o$ structure, although they could also be ordered islands of the same structure. Unfortunately, no high resolution images were obtained of this structure, but based on the results of Lahtonen et al., it must be a copper oxide phase [63]. Figure (7.23)b) shows an area of (4×4)- like structure where each row of atoms is separated by 11.5-12.5Å. This should be the structure that gives rise to the (4×4) LEED pattern. On the other hand, it has 2 domains which are rotated $\sim$ 30 degrees with respect to eachother (Figure (C.9), and which are both rotated $\sim$ 15 degrees with respect to the bulk (1×1). Because this structure was difficult to image, possibly due to mobility of atoms, the true nature of the (4×4)- like structure has not been revealed here. However, a $c(4 \times 4)$ structure with two rotational domains has been observed for deposition of Pb on Cu(100) [109], suggesting that this structure is due to copper oxide and not palladium oxide, in agreement with the surface being Cu rich as found by XPS. It is most likely not the (5×5) seen on oxidized Pd(100) because that structure only forms

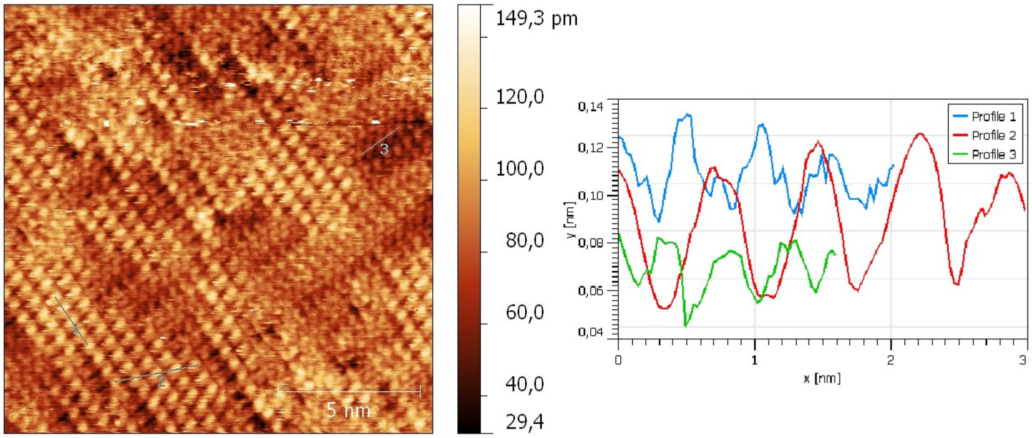

Figure 7.21: STM image of 3400L O_2 at 300^{o}C on the clean surface annealed to 600^{o}C (15x15nm^2, -0.30V, 2.74nA). Measured interatomic distances are 5.25Å in profile 1, 6.94Å in profile 2 and 4.35Å in profile 3. The structure is consistent with a $(2\sqrt{2} \times \sqrt{2})R45^o$ missing row reconstruction.

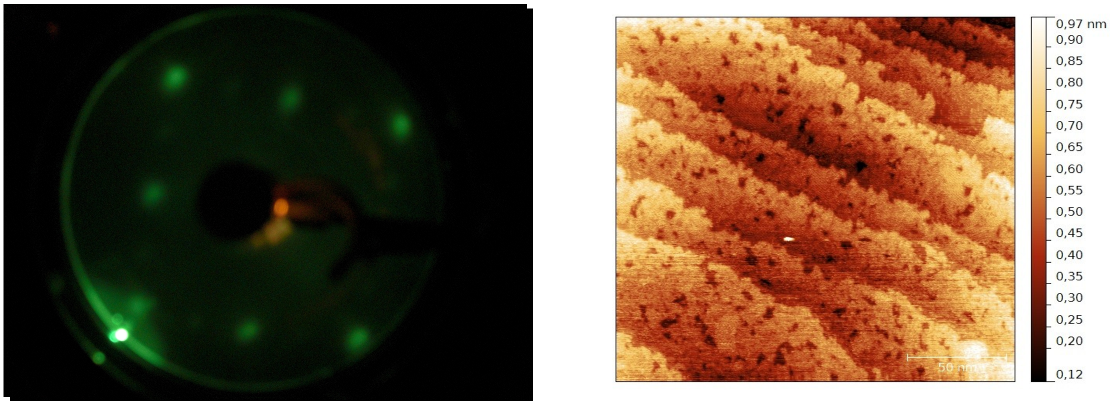

a) b)

Figure 7.22: a) LEED image of 3400L O_2 at 600^{o}C on the clean surface annealed to 600^{o}C with electron energy 30.9eV. The LEED pattern corresponds to a (4×4) structure. b) STM image of 3400L O_2 at 600^{o}C on the clean surface annealed to 600^{o}C (200x200nm^2, -0.37V, 2.24nA). The surface appears disordered on this scale, but a small ordered area can be seen in the bottom left part of the image.

below 400K [57]. Figure (7.23)b) further reveals that the roughness of this surface is due to a p(2

× 2) structure on top of a c(2 × 2). One more structure is seen in Figure (C.10), with measured interatomic distances of 8.3-9.0Å. It appears to have two domains, and each is rotated ∼ 30 degrees with respect to the (1 × 1) of the bulk. It is thus larger than the p(2 × 2), but smaller than the (4 × 4)- like structure. The interatomic distances and domain directions actually match those of the $(\sqrt{5} \times \sqrt{5})$R27^o structure seen on Pd(100) [57, 6, 58] quite well, but it does not look like that structure when the STM image in Figure (C.10) is compared to images of the $(\sqrt{5} \times \sqrt{5})$R27^o in the literature. Compared to the $(2\sqrt{2} \times \sqrt{2})$R45^o structure, the interatomic distances match, but the missing row reconstruction disagrees with this structure having two domains rotated ∼ 30 degrees instead of 45 degrees. Because good enough resolution was not obtained for this structure, it will have to be left for further studies to characterize it in more detail. No islands are seen on this surface, but step edges are oriented along the preferred [010] and [001] directions where the top layer is a c(2 × 2).

The fact that 3 new structures are seen for oxidation at 600^{o}C compared to oxidation at 300^{o}C might be a result of increased Cu segregation during oxidation as well as incorporation of oxygen beneath the surface layer. Both the $(\sqrt{5}\times\sqrt{5})$R27^o structure on Pd(100) [57] and the $(2\sqrt{2}\times\sqrt{2})$R45^o structure on Cu(100) [63] are known to form from the c(2 × 2) only after oxygen atoms have entered subsurface sites, at which point reconstruction can take place. In the work with this thesis, such reconstructions were only seen for oxidation of the clean sample after annealing to 600^{o}C, i.e. on the copper rich surface. This explains why the $(2\sqrt{2} \times \sqrt{2})$R45^o was seen while the $(\sqrt{5} \times \sqrt{5})$R27^o was absent except after the 1L oxidation at 300^{o}C on the copper rich surface annealed to 600^{o}C, where very small areas may have had that structure. On the Pd rich alloy surface annealed to 300^{o}C, only c(2 × 2) was seen even at very high oxygen pressures, thus the copper oxide $(2\sqrt{2} \times \sqrt{2})$R45^o clearly forms more easily than the palladium oxide $(\sqrt{5} \times \sqrt{5})$R27^o on this surface. This is taken as evidence that formation of copper oxide is preferred when the sample has been annealed to 600^{o}C, for oxidation at both 300^{o}C and 600^{o}C. No signs are seen for formation of bulk oxide in any of these experiments.

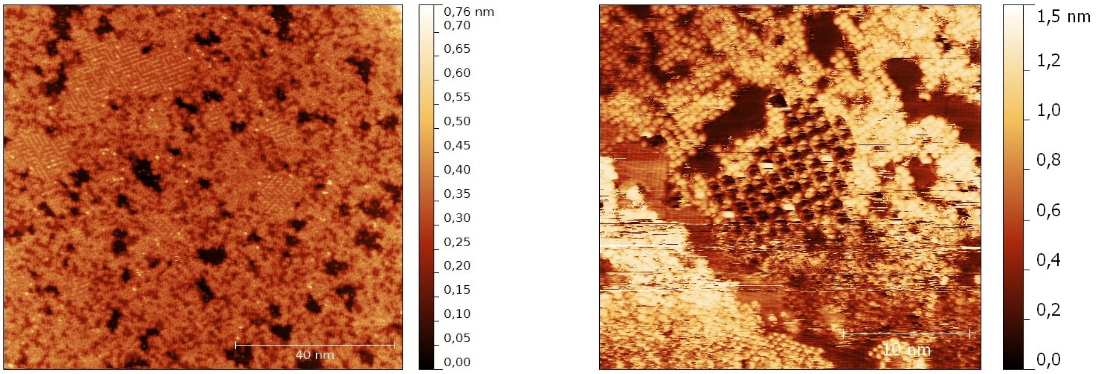

a) b)

Figure 7.23: a) STM image of 3400L O_2 at 600^{o}C on the clean surface annealed to 600^{o}C (100x100nm^2, -1.71V, 0.92nA). Areas of a maze- like structure are found between the otherwise rough and large areas. b) STM image of 3400L O_2 at 600^{o}C on the clean surface annealed to 600^{o}C (30x30nm^2, -0.44V, 2.10nA). Rows of the (4×4)- like structure are separated by 11.5-12.5Å. The image shows that the roughness of the surface at larger scale is due to a $p(2 \times 2)$ on top of a $c(2 \times 2)$ structure. The step edge in this image is oriented along the [010] and [001] directions where the $p(2 \times 2)$ is not covering it.

8. Suggestions for further work

Future experiments with this material in UHV should include further inspections of the hexagonal and (4 × 4)- like structures as well as the unknown structure seen for 3400L O_2 at 600^{o}C on the clean surface annealed to 600^{o}C. It would be very interesting to study the oxidation in-situ at the oxygen pressures applied here. An attempt was made to oxidize the PdCu(100) in-situ at up to $9{\cdot}10^{-9}$mbar, which is the highest pressure the ion pump can tolerate, but no specific results were obtained at this low pressure. If the Pdcu(100) sample was studied in a system allowing for high- pressure in-situ STM, a better understanding of formation of islands and boundary lines could be obtained. Oxygen pressures higher than $5{\cdot}10^{-5}$mbar could be applied in order to find out at which point a bulk oxide is formed. Density functional theory could be performed in order to explain the core level shifts seen for the clean surface at different annealing temperatures. In order to accuretely determine the chemical composition of the surface for different preparations, Low Energy Ion Scattering (LEIS) experiments should be considered. Also adsorption of CO and H_2 on this surface should be studied by STM, as those are the most relevant gas components in hydrogen separation membranes.

9. Conclusions

Clean and oxidized $Pd_{57}Cu_{43}(100)$ single crystal surfaces have been studied by LEED, STM and XPS in UHV conditions. A detailed understanding of this material and its oxidation at the atomic scale is obtained. It was found by XPS that Pd $3d_{\frac{5}{2}}$ spectra for the clean surface consist of a surface component and a bulk component. The surface component decreases with increasing annealing temperature, while the intensity of Cu 2p spectra increases, hence higher annealing temperature causes Cu to segregate to the surface. Pd $3d_{\frac{5}{2}}$ spectra are shifted towards higher binding energy with higher annealing temperature, probably as a result of the segregation processes, for which an equilibrium is nearly obtained after 15 minutes annealing. The clean sample annealed to 300^0C shows different structures for different preparations, depending on the preparation history of the sample. In one case, an ordered alloy structure with separate domains of Pd and Cu atoms was seen by STM. The surface then posessed a c(2 × 2) structure. In another case, the surface had undergone an order-disorder transition in which the separate Pd and Cu domains were replaced by an alloy layer of clock reconstructed c(2 × 2)-p4g structure. Small areas with (1 × 1) structure were found, thus the surface only partly reconstructs at 300^0C. On the Cu rich surface annealed to 600^0C, a p(2 × 2) structure was seen. At 300^0C the clean surface consists of several screw dislocations and island- like formations, and is therefore rich in defects. Annealing to 600^0C results in a more defect- free surface.

XPS spectra recorded for clean surfaces annealed to 300^0C and oxidized at 300^0C revealed that the surface component in Pd $3d_{\frac{5}{2}}$ spectra disappeared. No additional peaks were seen in Pd $3d_{\frac{5}{2}}$ or Cu 2p spectra, indicating that no bulk oxide had formed for any oxygen dosages of 500L-45100L. O 1s spectra consisted of just one peak, while Cu spectra became wider. STM images of 1L-33800L O_2 at 300^0C on the clean surface annealed to 300^0C showed coexisting p(2 × 2) and c(2 × 2) structures up to 10L, whereas only c(2 × 2) was seen at 68L or above. Thus the surface is clearly inert towards oxidation at these oxidation and annealing temperatures. Depending on the preparation history of the surface, oxide islands were present in some experiments, while they were absent in following experiments with the same preparation. These islands were found alongside phase boundary lines and screw dislocations, which means defects play an important role in the formation of islands. Because the surface contained fewer defects after annealing to 600^0C, and because an order- disorder transition is found to occur, the absence of islands must be due to the sample previously having been annealed to 600^0C. Step edges were ordered in two preferential directions after oxidation of the surface annealed to 300^0C for all dosages of 68L and above.

Oxidation of the clean sample annealed to 600^0C indeed showed very few and very small islands. For 3400L dosages, step edges were oriented in the same two directions as on the clean surface annealed to 300^0C. Oxidations with 1L-10L O_2 at 300^0C on this surface resulted in an incomplete c(2 × 2) layer. A hexagonal structure was seen in small areas at 10L O_2. Increasing the dosage to 3400L O_2 resulted in large areas of a $(2\sqrt{2} \times \sqrt{2})R45^o$ missing row reconstruction previously seen for oxidation of Cu(100) [63]. An oxidation with 3400L performed at 600^0C resulted in a rough surface with many different structures coexisting. These were c(2×2), p(2×2), (4×4)- like, a maze structure and one that could not be characterized. Given that the surface was Cu rich prior to oxidation and that Cu may segregate during oxidation, and the fact that several structures were seen which correspond to structures reported in the literature for Cu(100), it must be a copper oxide that is formed when $Pd_{57}Cu_{43}$(100) annealed to 600^0C is oxidized. No evidence for formation of bulk oxide was found in any of these experiments.

Bibliography

[1] J. R. H. Ross, Elsevier (2012), *Heterogeneous catalysis: Fundamentals and applications*

[2] E. Lundgren, A. Mikkelsen, J. N. Andersen et al., Journal of Physics: Condensed Matter, Vol. 18, Iss 30 (2006) 481-499 , *Surface oxides on close-packed surfaces of late transition metals*

[3] E. Lundgren, J. Gustafson, A. Mikkelsen et al., Physical Review Letters, Vol. 92, Iss. 4 (2004) , *Kinetic hindrance during the initial oxidation of Pd(100) at ambient pressures*

[4] "The Nobel Prize in Chemistry 2007". Nobelprize.org. 10 Feb 2012 *http://www.nobelprize.org/nobel_prizes/chemistry/laureates/2007/*

[5] U. Diebold S.-C. Li, M Schmid, Ann. Rev. of Physican Chemistry, Vol 61 (2010), 129-148 , *Oxide Surface Science*

[6] P. Kostelnik, N. Seriani, G. Kresse et al., Surface Science, Vol. 601, Iss. 6 (2007), 1574-1581 , *The Pd (100)-(root 5 x root 5)R27 degrees-O surface oxide: A LEED, DFT and STM study*

[7] D. A. Bell, B. F. Towler, F. Maohong, Elsevier 2011, 35-100, 137-156 , *Coal Gasification and Its Applications*

[8] C Higman, M. van der Burgt, Elsevier 2008, 1-9, 91-367 , *Gasification*

[9] C. P. O'Brien, B. H. Howard, J. B. Miller et al., Journal of Membrane Science, Vol. 349, Iss. 1-2 (2010), 380-384 , *Inhibition of hydrogen transport through Pd and Pd(47)Cu(53) membranes by H(2)S at 350 degrees C*

[10] J. B. Miller, C. Matranga, A. J. Gellman, Surface Science, Vol. 602, Iss. 1 (2008), 375-382 , *Surface segregation in a polycrystalline Pd70Cu30 alloy hydrogen purification membrane*

[11] I. P. Jain, International Journal of Hydrogen Energy, Vol. 34, Iss. 17 (2009), 7368-7378 , *Hydrogen the fuel for 21st century*

[12] D. Ciuparu, M. R. Lyubovsky, E. Altman, et al., Catalysis Reviews: Science and Engineering, Vol. 44, Iss. 4, 593-649 , *Catalytic combustion of methane over palladium-based catalysts*

[13] S. Tagliaferri, R. A. Koppel, A. Baiker, Applied Catalysis B: Environmental, Vol. 15, Iss. 3-4 (1998), 159-177 , *Influence of rhodium- and ceria-promotion of automotive palladium catalyst on its catalytic behaviour under steady-state and dynamic operation*

[14] B. D. Morreale, M. V. Ciocco, R. M. Enick et al., Journal of Membrane Science Vol. 212, Iss. 1-2 (2003), 87-97 , *The permeability of hydrogen in bulk palladium at elevated temperatures and pressures*

[15] G. J. Grashoff, C. E. Pilkington, C. W. Corti, Platinum Metals Review, Vol. 27, Iss. 4 (1983), 157-169 , *The Purification of Hydrogen: A review of the technology emphasising the current status of palladium membrane diffusion*

[16] C.-H. Chen, Y. H. Ma, Journal of Membrane Science, Vol. 362, Iss. 1-2, 535-544 , *The effect of H(2)S on the performance of Pd and Pd/Au composite membrane*

[17] B. D. Morreale, B. H. Howard, O. Iyoha et al., Industrial & Engineering Chemistry Research, Vol. 46, Iss. 19,6 313-6319 , *Experimental and computational prediction of the hydrogen transport properties of Pd4S*

[18] Ø. Hatlevik, S. K. Gade, M. K. Keeling et al., Separation and Purification Technology, Vol. 73, Iss. 1 Special Issue: SI (2010), 59-64, , *Palladium and palladium alloy membranes for hydrogen separation and production: History, fabrication strategies, and current performance*

[19] L. Semidey-Flecha, C. Ling, D. S. Sholl, Journal of Membrane Science, Vol. 362, Iss. 1-2 (2010), 384-392 , *Detailed first-principles models of hydrogen permeation through PdCu-based ternary alloys*

[20] L. Shi, A. Goldbach, G. Zeng et al., International Journal of Hydrogen Energy, Vol. 35, Iss. 9, 4201-4208 , *Preparation and performance of thin-layered PdAu/ceramic composite membranes*

[21] C. G. Sonwane, J. Wilcox, Y. H. Ma, Journal of Chemical Physics, Vol. 125, Iss. 18 (2006) , *Achieving optimum hydrogen permeability in PdAg and PdAu alloys*

[22] S. K. Gade, M. K. Keeling, A. P. Davidson et al., International Journal of Hydrogen Energy, Vol. 34, Iss. 15 (2009), 6484-6491 , *Palladium-ruthenium membranes for hydrogen separation fabricated by electroless co-deposition*

[23] B. H. Howard, R. P. Killmeyer, K. S. Rothenberger et al., Journal of Membrane Science, Vol. 241, Iss. 2 (2004), 207-218 , *Hydrogen permeance of palladium-copper alloy membranes over a wide range of temperatures and pressures*

[24] A. Kulprathipanja, G. O. Alptekin, J. L. Falconer et al., Journal of Membrane Science, Vol. 254, Iss. 1-2 (2005), 49-62, *Pd and Pd-Cu membranes: inhibition of H-2 permeation by H2S*

[25] F. Roa, J. D. Way, Applied Surface Science, Vol. 240, Iss. 1-4 (2005), 85-104 , *The effect of air exposure on palladium-copper composite membranes*

[26] A. L. Mejdell et al., Journal of Membrane Science, Vol. 307, Iss. 1 (2008), 96-104 , *Hydrogen permeation of thin, free-standing Pd/Ag23% membranes before and after heat treatment in air*

[27] L. Yang, Z. X. Zhang, X. H. Gao et al., Journal of Membrane Science, Vol. 252, Iss. 1-2 (2005), 145-154 , *Changes in hydrogen permeability and surface state of Pd-Ag/ceramic composite membranes after thermal treatment*

[28] L. Yang, Z. Zhang, B. Yao et al., Aiche Journal, Vol. 52, Iss. 8 (2006), 2783-2791 , *Hydrogen permeance and surface states of Pd-Ag/ceramic composite membranes*

[29] W. M. Tucho, H. J. Venvik, J. C. Walmsley et al., Journal of Materials Science, Vol. 44, Iss. 16 (2009), 4429-4442 , *Microstructural studies of self-supported (1.5-10 mu m) Pd/23 wt% Ag hydrogen separation membranes subjected to different heat treatments*

[30] A. Ramachandran, W. M. Tucho, A. L. Mejdell et al., Applied Surface Science, Vol. 256, Iss. 20 (2010), 6121-6132 , *Surface characterization of Pd/Ag23 wt% membranes after different thermal treatments*

[31] F. Bechstedt, Springer (2003), 1-80 , *Principles of surface physics*

[32] J. B. Hudson, Butterworth-Heinemann (1992), 1-26, 170-197 , *Surface Science: An introduction*

[33] M. Prutton, Oxford University Press (1994), 1-150 , *Introduction to Surface Physics*

[34] C. T. Campbell, Surface Science Reports, Vol. 27, Iss. 1-3 (1997), 1-111 , *Ultrathin metal films and particles on oxide surfaces: Structural, electronic and chemisorptive properties*

[35] H. Lüth, Springer, 3rd edition (2001), 83-108, 128-138, 147-154, 210-218 , *Solid Surfaces, Interfaces and Thin Films*

[36] R. Franchy, Surface Science Reports, Vol. 38, Iss. 6-8 (2000), 199-294 , *Growth of thin, crystalline oxide, nitride and oxynitride films on metal and metal alloy surfaces*

[37] K. W. Kolasinski, John Wiley & Sons (2002), 1-30, 249-284 , *Surface Science: Foundations of Catalysis and Nanoscience*

[38] S. Titmuss, A. Wander, D. A. King, Chemical Reviews, Vol. 96, Iss. 4 (1996), 1291-1305 , *Reconstruction of clean and adsorbate-covered metal surfaces*

[39] R. J. Needs, M. J. Godfrey, M. Mansfield, Surface Science, Vol. 242, Iss. 1-3 (1991), 215-221 , *Theory of surface stress and surface reconstruction*

[40] R. C. Cammarata, Surface Science, Vol. 273, Iss. 1-2 (1992), L399-L402 , *Thermodynamic model for surface reconstruction based on surface stress effects*

[41] R. C. Cammarata, Progress in Surface Science, Vol. 46, Iss. 1 (1994), 1-38 , *Surface and interface stress effects in thin-films*

[42] D. McLean, Oxford University Press, London (1957), *Grain Boundaries in Metals*. Referred to in [43]

[43] M. Polak, L. Rubinovich, Surface Science Reports Vol. 38, Iss. 4-5 (2000), 127-194 , *The interplay of surface segregation and atomic order in alloys*

[44] A. Atkinson, Reviews of Modern Physics, Vol. 57, Iss. 2 (1985), 437-470 , *Transport processes during the growth of oxide-films at elevated temperature*

[45] N. Cabrera, N. F. Mott, Reports on Progress in Physics, Vol. 12 (1949), 163 , *Theory of the oxidation of metals*

[46] S. P. Baranov, L. A. Abramova, A. V. Zeigarnik et al., Surface Science, Vol. 555, Iss. 1-3 (2004), 20-42 , *Monte Carlo modeling of O-2 adsorption kinetics on unreconstructed fcc(100) surfaces of metals using UBI-QEP coverage-dependent energetics*

[47] WolframAlpha^{TM} computational knowledge engine, *http://www.wolframalpha.com/*

[48] M. S. Mousa, J. Loboda-Cackovic, J. H. Block, Vacuum, Vol. 46, Iss. 2 (1995), 117-125 , *Characterization of PdCu(110) single-crystal surface compositions during CO chemisorption*

[49] M. Hansen, K. Anderko, McGraw-Hill, New York (1958), 612 , *Constitution of binary alloys* (Referred to in [51])

[50] D. Priyadarshini et al., Journal of Physical Chemistry C, Vol. 115, Iss. 20 (2011), 10155-10163 , *High-throughput characterization of surface segregation in CuxPd1-x alloys*

[51] J. Loboda-Cackovic, Vacuum, Vol. 48, Iss. 6 (1997), 571-578 , *Temperature-induced irreversible changes in the PdCu(110) surface microstructure*

[52] M. S. Mousa, J. Loboda-Cackovic, J. H. Block, J.H, Vacuum, Vol. 46, Iss. 2 (1995), 89-96 , *Surface analysis of the PdCu(110) single crystal alloy at different segregation rates*

[53] J. Loboda-Cackovic, J. H. Block, Vacuum, Vol. 46, Iss. 12 (1995), 1449-1453 , *Properties of PdCu(110) single crystal alloy surfaces: reversible changes of domain sizes*

[54] J. Loboda-Cackovic, Vacuum, Vol. 47, Iss. 12 (1996), 1405-1411 , *Properties of PdCu(110) single crystal alloy surfaces: Temperature-induced processes in the surface microstructure*

[55] A. Hammoudeh, M. S. Mousa, J. Loboda-Cackovic, Vacuum, Vol. 54 Iss. 1-4 (1999), 239-243 , *Interaction of CO with clean and oxygen covered PdCu(110) single crystal alloy*

[56] G. Zheng, E. I. Altman, Journal of Physical Chemistry B, Vol. 106, Iss. 5 (2002), 1048-1057 , *The reactivity of surface oxygen phases on Pd(100) toward reduction by CO*

[57] G. Zheng, E. I. Altman, Surface Science, Vol. 504, Iss. 1-3 (2002), 253-270 , *The oxidation mechanism of Pd(100)*

[58] M. Todorova, E. Lundgren, V. Blum et al., Surface Science, Vol. 541, Iss. 1-3 (2003), 101-112 , *The Pd(100)-(root 5 x root 5)R27 degrees-O surface oxide revisited*

[59] N. Seriani, J. Harl, F. Mittendorfer et al., Journal of Chemical Physics, Vol. 131, Iss. 5 (2009), Art. number 054701 , *A first-principles study of bulk oxide formation on Pd(100)*

[60] E. Lundgren, J. Gustafson, A. Mikkelsen et al., Physical Review Letters, Vol. 92, Iss. 4 (2004), Art. number: 046101 , *Kinetic hindrance during the initial oxidation of Pd(100) at ambient pressures*

[61] J. Han, D. Zemlyanov, F. H. Ribeiro, Surface Science, Vol. 600, Iss. 13 (2006), 2730-2744 , *Interaction of O2 with Pd single crystals in the range 1-150 Tor: Surface morphology transformations*

[62] B. L. M. Hendriksen, S. C. Bobaru, J. W. M. Frenken, Surface Science, Vol. 552, Iss. 1-3 (2004), 229-242 , *Oscillatory CO oxidation on Pd(100) studied with in situ scanning tunneling microscopy*

[63] K. Lahtonen K, M. Hirsimäki, M. Lampimäki et al., Journal of Chemical Physics, Vol. 129, Iss. 12 (2008), Art. number: 124703 , *Oxygen adsorption-induced nanostructures and island formation on Cu(100): Bridging the gap between the formation of surface confined oxygen chemisorption layer and oxide formation*

[64] S. Jaatinen, M. Rusanen, P. Salo, Surface Science, Vol. 601, Iss. 8 (2007), 1813-1821 , *A multi-scale Monte Carlo study of oxide structures on the Cu(100) surface*

[65] F. Zaera, Chemical Record, Vol. 5, Iss. 3 (2005), 133-144 , *The surface chemistry of heterogeneous catalysis: Mechanisms, selectivity, and active sites*

[66] A. O. Musa, T. Akomolafe, M. J. Carter, Solar Energy Materials and Solar Cells, Vol. 51, Iss. 3-4 (1998), 305-316 , *Production of cuprous oxide, a solar cell material, by thermal oxidation and a study of its physical and electrical properties*

[67] S. T. Shishiyanu, T. S. Shishiyanu, O. I., Sensors and Actuators B - Chemical, Vol. 113, Iss. 1 (2006), 468-476 , *Novel NO2 gas sensor based on cuprous oxide thin films*

[68] J. H. Onuferko, D. P. Woodruff, Surface Science, Vol. 95, Iss. 2-3 (1980), 555-570 , *LEED Structural study of the adsorption of oxygen on Cu(100) surfaces*

[69] A. Puisto, H. Pitkanen, M. Alatalo et al., Catalysis Today, Vol. 100, Issue: 3-4 (2005), 403-406 , *Adsorption of atomic and molecular oxygen on Cu(100)*

[70] G. W. Zhou, J. C. Yang, Materials Science Forum, Vol. 461-464 (2004), 183-190 , *Nano-oxidation of Cu(100) investigated by in situ UHV-TEM*

[71] G. W. Zhou, J. C. Yang, Physical Review Letters, Vol. 93, Iss. 22 (2004), Art. number: 226101 , *Reduction of Cu2O islands grown on a Cu(100) surface through vacuum annealing*

[72] L. Luo, Y. Kang, Z. Liu et al., Physical Review B, Vol. 83, Iss. 15 (2011), Art. number: 155418 , *Dependence of degree of orientation of copper oxide nuclei on oxygen pressure during initial stages of copper oxidation*

[73] T. Kangas, K. Laasonen, A. Puisto et al., Surface Science, Vol. 584, Iss. 1 (2005), 62-69 , *On-surface and sub-surface oxygen on ideal and reconstructed Cu(100)*

[74] T. Kangas, K. Laasonen, Surface Science, Vol. 602, Iss. 21 (2008), 3239-3245 , *DFT study of reconstructed Cu(100) surface with high oxygen coverages*

[75] M. Lee, A. J. H. McGaughey, Surface Science, Vol. 604, Iss. 17-18 (2010), 1425-1431 , *Role of sub-surface oxygen in Cu(100) oxidation*

[76] M Lee, A. J. H. McGaughey, Surface Science, Vol. 603, Iss. 24 (2009), 3404-3409 , *Energetics of oxygen embedment into unreconstructed and reconstructed Cu(100) surfaces: Density functional theory calculations*

[77] M. Lee, A. J. H. McGaughey, Physical Review B, Vol. 83, Iss. 16 (2011), Art. number: 165447 , *Energetics and kinetics of the c(2 x 2) to (2 root 2 x root 2)R45 degrees transition during the early stages of Cu(100) oxidation*

[78] X. Duan, O. Warschkow, A. Soon et al., Physical Review B, Vol. 81, Iss. 7 (2010), Art. number: 075430 , *Density functional study of oxygen on Cu(100) and Cu(110) surfaces*

[79] T. D. Pope, K. Griffiths, P. R. Norton, Surface Science, Vol. 306, Iss. 3 (1994), 294-312 , *Surface and interfacial alloys of Pd with Cu(100) - Structure, photoemission and CO Chemisorption*

[80] P. W. Murray, I. Stensgaard, E. Lægsgaard et al., Surface Science, Vol. 365, Iss. 3 (1996), 591-601 , *Growth and structure of Pd alloys on Cu(100)*

[81] K. Pussi, M. Lindroos, E. AlShamaileh et al., Surface Science, Vol. 513, Iss. 3 (2002), 555-568, Art. number: PII S0039-6028(02)01875-7 , *A SATLEED study of the geometric structure of Cu100-Pd monolayer surface alloys*

[82] T. D. Pope, M. Vos, H. T. Tang et al., Surface Science, Vol. 337, Iss. 1-2 (1995), 79-91 , *A structural study of Pd/Cu(100) surface alloys*

[83] Y. G. Shen, A. Bilic A, D. J. O'Connor et al., Surface Science, Vol. 394, Iss. 1-3 (1997), L131-L137 , *Reinvestigation of the surface reconstruction of Cu(001)-(2x2)p4g-Pd*

[84] D. Spisak, J. Hafner, Physical Review B, Vol. 67, Iss. 23 (2003), Art. number: 235403 , *Theoretical analysis of clock-reconstructed PdCu surface alloy* , Figure taken from: *http://www.univie.ac.at/qccd/hpsc/2003/Kresse/spisak_bericht/PdCu_alloys.html*

[85] J. C. Vickerman and contributors, Wiley & Sons (1997), 43-92, 324-331, 393-423 , *Surface analysis, the principal techniques*

[86] B. Viswanathan, S. Kannan, R. C. Deka, Alpha Science International LTD. (2010), p. 7.1-7.60, 10.4 , *Catalysts and surfaces, characterization techniques*

[87] "The Nobel Prize in Physics 1986". Nobelprize.org. 9 Jan 2012 http://www.nobelprize.org/nobel_prizes/physics/laureates/1986/

[88] R. H. Fowler, L. W. Nordheim, Proc. Roy. Soc. A 119, 173 (1928)

[89] J. Tersoff, D. R. Hamann, Physical Review B, Vol. 31, Iss. 2 (1985), 805-813 , *Theory of the Scanning Tunneling Microscope*

[90] G. Binnig, H. Rohrer, Reviews of Modern Physics, Vol. 59, Iss. 3 (1987), 615-625, Part 1 , *Scanning Tunneling Microscopy - From Birth To Adolescence*

[91] R. J. Behm, N. Garcia, H. Rohrer, Kluwer Academic Publishers (1990), 217 , *Scanning Tunneling Microscopy and Related Methods*

[92] G. Yongli, Materials Science & Engineering R-Reports, Vol. 68, Iss. 3 (2010), 39-87 , *Surface analytical studies of interfaces in organic semiconductor devices*

[93] F. Reinert, S. Hufner, New Journal of Physics, Vol. 7 (2005), Art. Num. 97 , *Photoemission spectroscopy - from early days to recent applications*

[94] M.P. Seah, W.A. Dench, Surf. Interf. Anal. 1 (1979) 2

[95] Homepage of HASYLAB and DESY: *http://hasylab.desy.de*

[96] S. Hüfner, Springer (2003), 1-57 , *Photoelectron spectroscopy, principles and applications*

[97] D. Attwood, Cambridge Univerisity Press (1999), 123-186 , *Soft X- rays and Extreme Ultraviolet Radiation, Principles and applications*

[98] Wikipedia: *http://en.wikipedia.org/wiki/Angle-resolved_photoemission_spectroscopy*

[99] Omicron Vakuumphysik GMBH user manual , *Getting Started with Omicron UHV STM*, version 1.0 (1990)

[100] MAX-lab homepage: *http://www.maxlab.lu.se/*

[101] © David Necas and Petr Klapetek, Gwyddion user guide, *http://gwyddion.net/download/user-guide/gwyddion-user-guide-en-2009-11-11.pdf*

[102] © WaveMetrics, Inc., Igor Pro manual, *http://www.wavemetrics.com/products/igorpro/manual.htm*

[103] XPS Fitting Program by David Adams, University of Aarhus, *http://www.sljus.lu.se/download.html*

[104] S. Doniach, M. Šunjić, Journal of Physics C, Vol. 3, Iss. 2 (1970), 285 , *Many-electron singularity in x-ray photoemission and x-ray line spectra from metals*

[105] W. Olovsson, I. A. Abrikosov, B. Johansson B, Journal of Electron Spectroscopy and Related Phenomena, Vol. 127, Iss. 1-2 (2002), 65-69 , *Core level shift in random CuPd and AgPd alloys by the complete screening picture*

[106] N. Mårtensson, R. Nyholm, H. Calen et al., Physical Review B, Vol. 24, Iss. 4 (1981), 1725-1738 , *Electron-spectroscopic studies of the* Cu_xPd_{1-x} *alloy system - Chemical-shift effects and valence-electron spectra*

[107] H. Tillborg, A. Nilsson, T. Wiell, et al., Physical Review B, Vol. 47, Iss. 24 (1993), 16464-16470 , *Electronic structure of atomic oxygen adsorbed on Ni(100) and Cu(100) studied by soft x-ray emission and photoelectron spectroscopies*

[108] P. Varga, M. Schmid, Applied Surface Science, Vol. 141, Iss. 3-4, 287-293 (1999) , *Chemical discrimination on atomic level by STM*

[109] C. Nagl et al., Surface Science, Vol. 331, Part a (1995), 831-837 , *Surface alloying and superstructures of Pb on Cu(100)*

A. XPS spectra

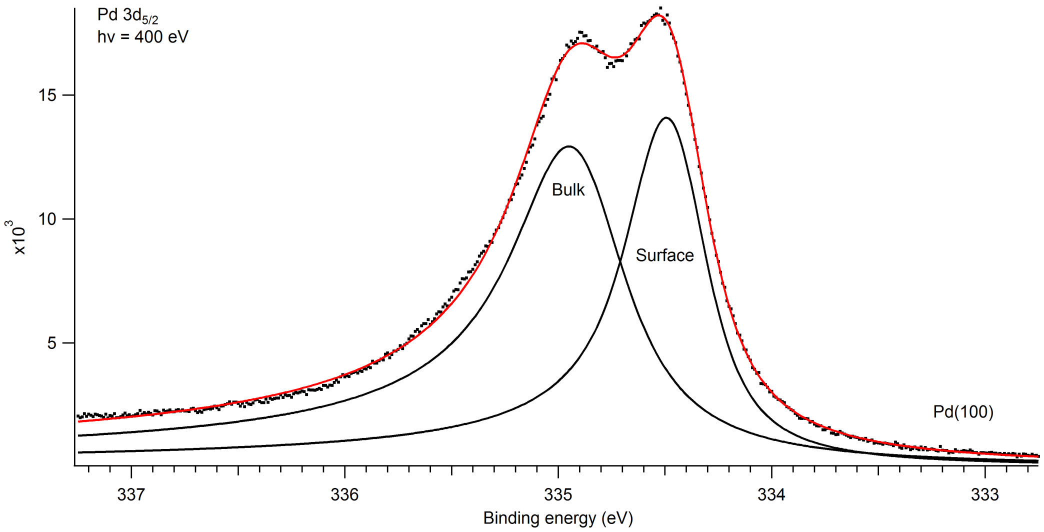

Figure A.1: Pd $3d_{\frac{5}{2}}$ spectrum for clean Pd(100) recorded previously by the group that performed XPS experiments on PdCu(100). Note that the surface component is as high as the bulk component. The position of the bulk component is $\sim$ 335eV.

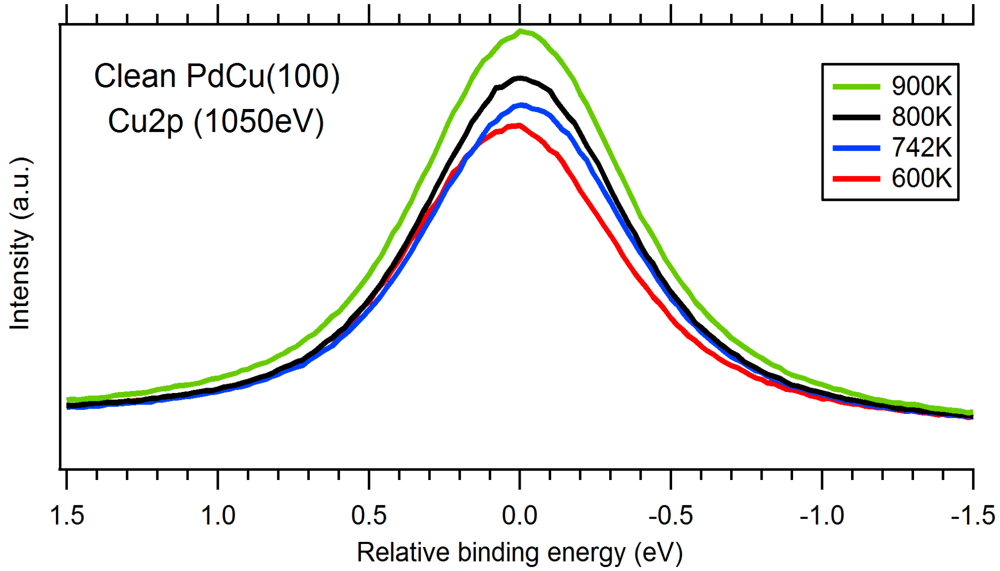

Figure A.2: Cu 2p spectra for the clean PdCu(100) surface after different annealings. There is more copper in the XPS accessible region with higher annealing temperature.

B. LEED images

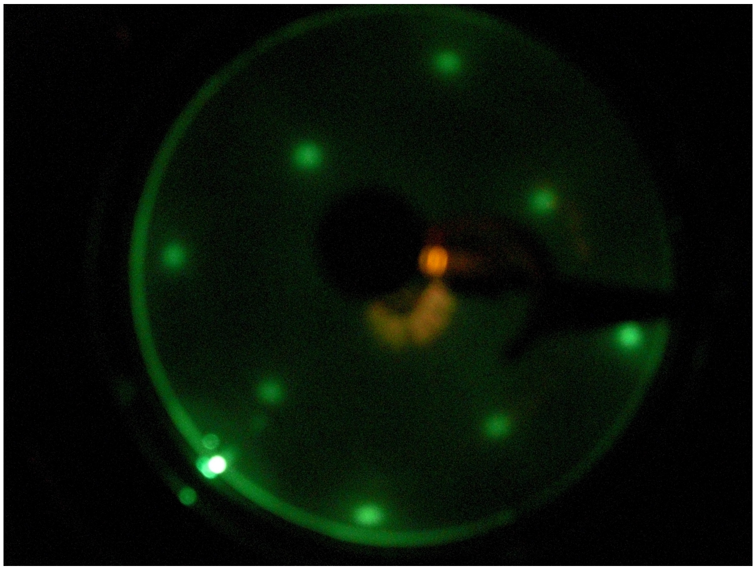

Figure B.1: LEED image of 3400L O_2 @ 300^{o}C / PdCu(100)_[600^{o}C] with an electron energy of 60.0eV.

C. STM images

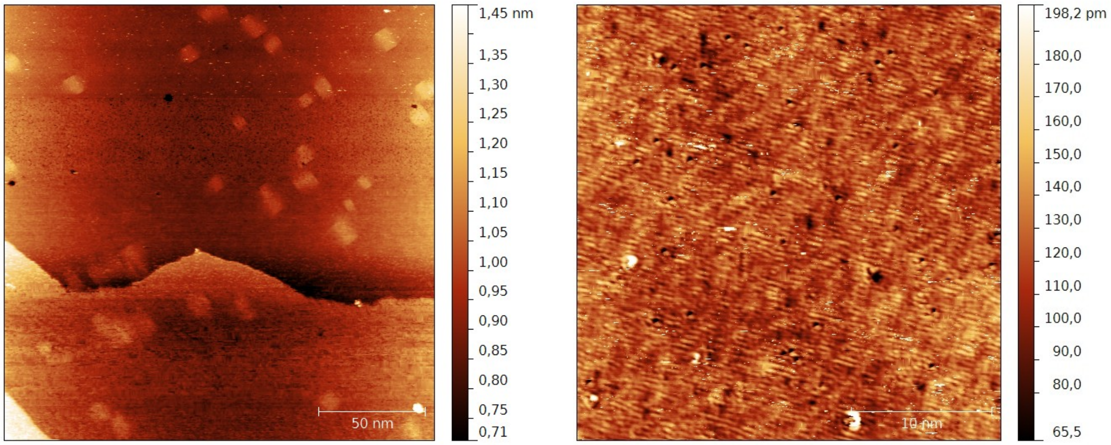

Figure C.1: Left: STM image of the clean surface annealed to 300^{o}C for 30 minutes (200x200nm^2, 0.50V, 1.68nA), showing a smooth surface with large flat terraces. Right: STM image of the clean surface annealed to 300^{o}C for 30 minutes (30x30nm^2, 0.29V, 2.70nA). The surface appears to be covered by a c(2 × 2)- p4g structure.

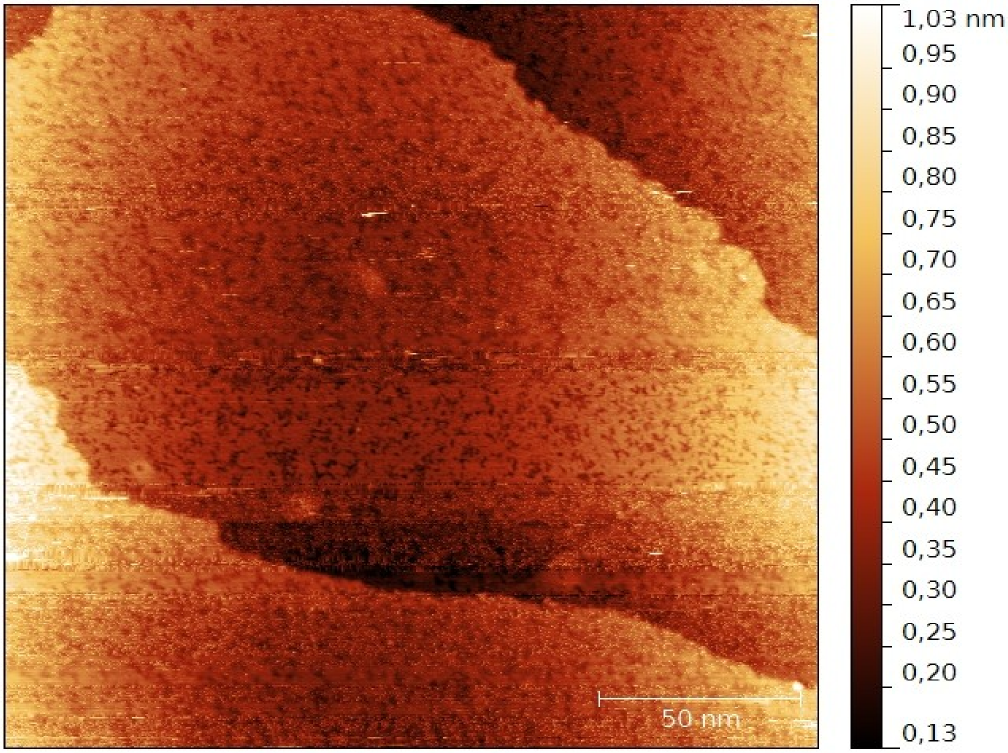

Figure C.2: STM image of 1L O_2 @ 300^{o}C / PdCu(100)$_-$[300^{o}C] (200x200nm^2, -0.26V, 2.58nA). The surface is rough, and the island- like formations seen on the clean surface annealed to the same temperature are visible also after this oxidation.

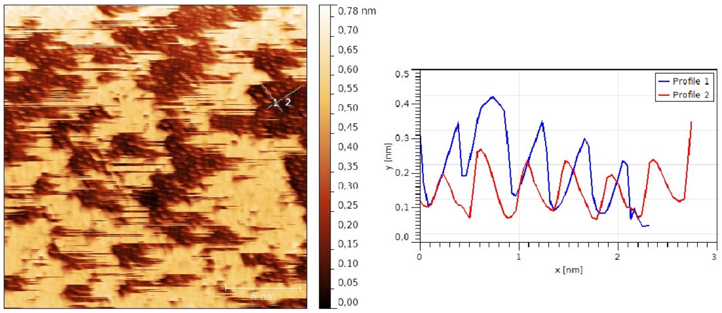

Figure C.3: STM image of 1L O_2 @ 300^{o}C / PdCu(100)_[300^{o}C] (20x20nm^2, 0.34V, 2.68nA). Interatomic distances measured along the line profiles are $\sim$ 4.2Å in the directions of the bulk (1×1) structure. It must therefore be a p(2×2), although a c(2×2) is also visible in parts of the image.

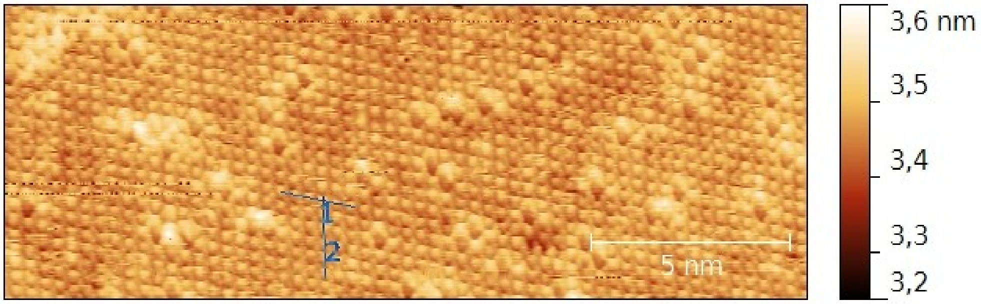

Figure C.4: STM image of 68L O_2 @ 300^{o}C / PdCu(100)_[300^{o}C] (20x20nm^2, -0.29V, 2.46nA) showing the c(2×2) structure with point defects which are probably vacancies.

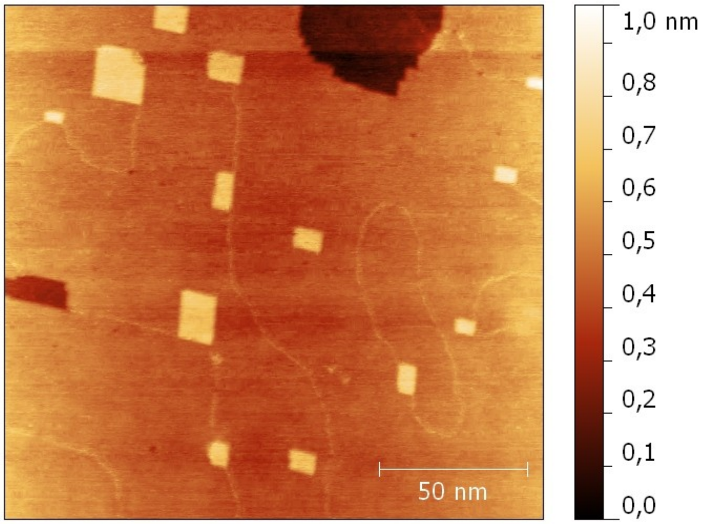

Figure C.5: STM image of 1350L O_2 @ 300^{o}C / PdCu(100)$_-$[300^{o}C] (250x250nm^2, 0.47V, 1.94nA) showing a flat area with islands and phase boundary lines.

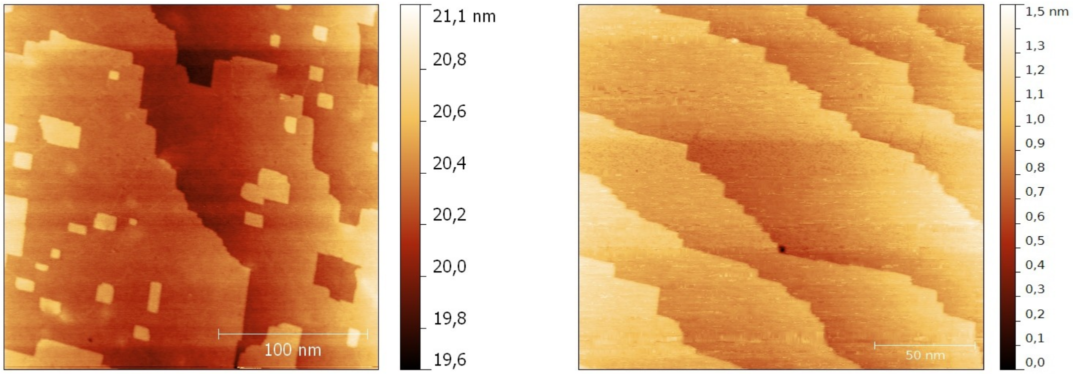

Figure C.6: Left: STM image of 3400L O_2 @ 300^{o}C / PdCu(100)$_-$[300^{o}C] (250x250nm^2, 0.99V, 1.68nA) showing several islands. Right: STM image of 3400L O_2 @ 300^{o}C / PdCu(100)$_-$[300^{o}C] (200x200nm^2, 0.95V, 1.32nA) where no islands are present.

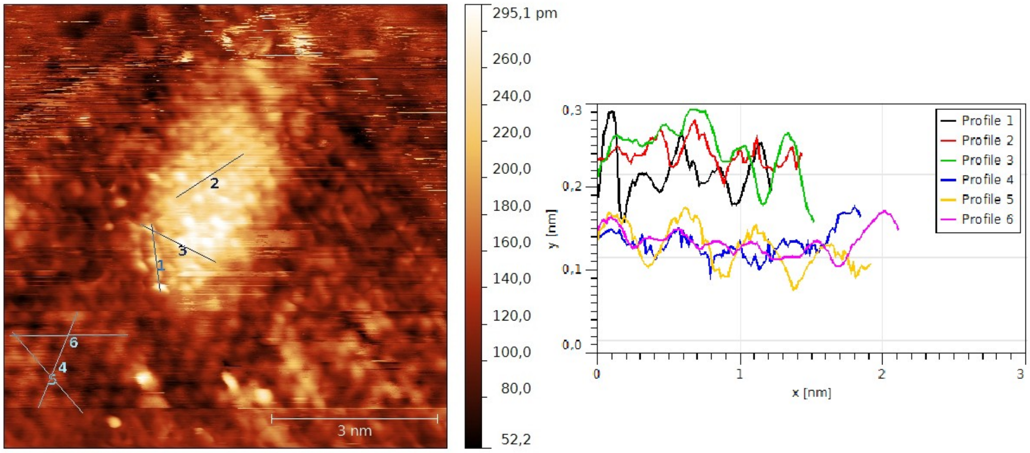

Figure C.7: STM image of 1L O_2 @ 300^{o}C / PdCu(100)_[600^{o}C] (8x8nm^2, -0.26V, 3.57nA) of an area with a structure larger than the c(2 × 2). Interatomic distances along profiles 1,2 and 3 are 2.6-3.0Å, while those along profiles 4,5 and 6 are 4.1-5.0Å.

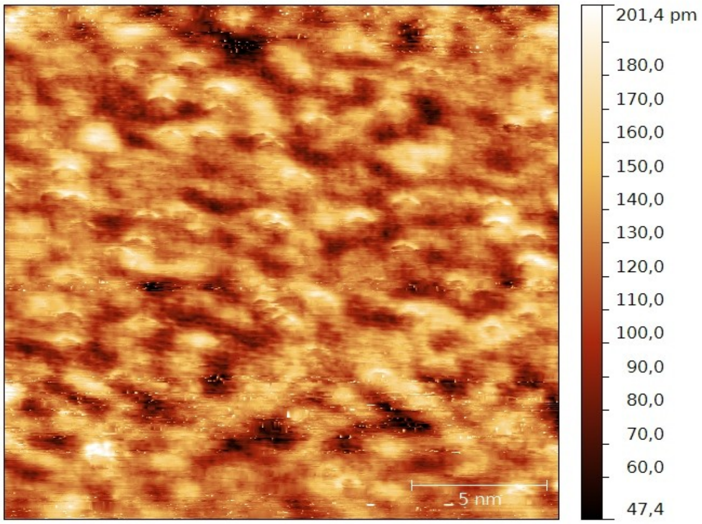

Figure C.8: STM image of 10L O_2 @ 300^{o}C / PdCu(100)_[600^{o}C] (20x20nm^2, 0.34V, 2.48nA). For this preparation, a p(2 × 2) structure is seen on top of a c(2 × 2).

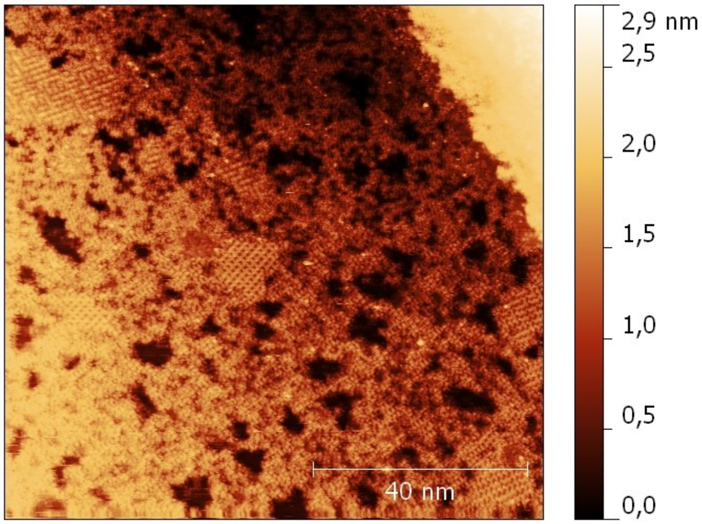

Figure C.9: STM image of 3400L O_2 @ 600^oC / PdCu(100)_[600^oC] (100x100nm^2, -1.70V, 0.91nA). In the upper left corner, a maze- like structure is seen which is made up of CuO_2 islands on top of a $(2\sqrt{2} \times \sqrt{2})R45^o$ reconstructed area. Two domains of the large (4×4) structure are seen.

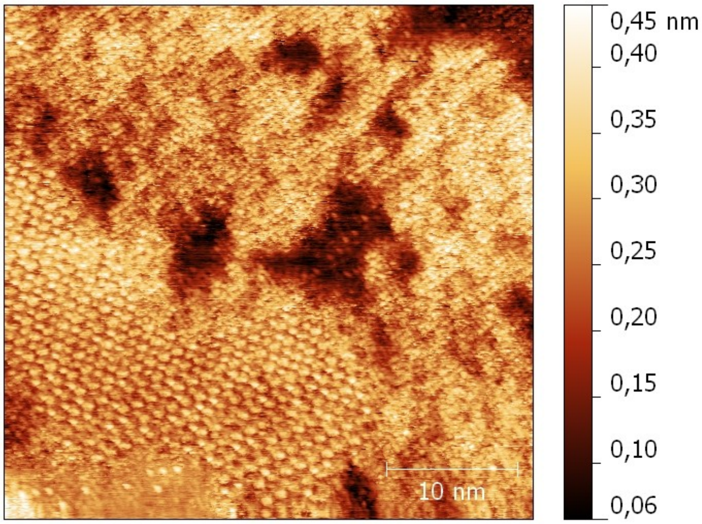

Figure C.10: STM image of 3400L O_2 @ 600^oC / PdCu(100)_[600^oC] (40x40nm^2, 0.40V, 2.10nA). Measured interatomic distances are 8.3-9.0Å and it is rotated ∼ 30 degrees with resect to the (1×1) bulk structure. The surrounding bright areas consist of the $p(2 \times 2)$.